NORTHWESTERN UNIVERSITY

Synchrotron X-ray Studies of Novel Electronic Materials

A DISSERTATION

SUBMITTED TO THE GRADUATE SCHOOL
IN PARTIAL FULFILLMENT OF THE REQUIREMENTS

for the degree

DOCTOR OF PHILOSOPHY

Field of Applied Physics

By

Li Zeng

EVANSTON, ILLINOIS

December 2017

Abstract

Synchrotron X-ray Studies of Novel Electronic Materials

Li Zeng

The promise of next-generation electronics, which combines features such as mechanical flexibility, optical transparency, and relatively low-cost, has stimulated tremendous research efforts during the past few years. As perhaps the most fundamental component of an electronic circuit, the design and optimization of the thin film transistor (TFT) is of great importance, especially the choice of the channel layer and dielectric layer materials. Transparent amorphous metal oxide (AMO) semiconducting materials replacing the traditional Si as the channel layer, and the invention of organic/inorganic hybrid ultra-thin dielectrics have demonstrated the ability to enhance performance and the potentials for the future device fabrication. However, despite the encouraging device performance, many fundamental aspects regarding their structures and non-electronic properties are largely unexplored. Herein, I will present how synchrotron X-ray characterization techniques can provide an improved view of these materials. I will show how long-period X-ray standing waves can measure the Br counteranion distributions within two self-assembled nano-dielectrics (SANDs) of differing polarity. Using synchrotron X-ray techniques and complementary DFT simulation, I will quantitatively determine the spacing, composition, elemental distribution, and molecular orientation within each trilayer-SAND heterolayer structure. Moreover, I will discuss the thermal stability study of AMOs synthesized by pulsed-laser deposition (PLD). The crystallization process of amorphous In_2O_3 films deposited as a function of deposition temperature under the isothermal-anneal condition is studied via *in situ* grazing incidence wide-angle X-ray scattering (GIWAXS) and level-set simulation. GIWAXS is also used to characterize the isochronal crystallization process of AMO thin films to systematically compare and study the effects of the secondary metal ions on the crystallization kinetics.

Approved

Professor Michael J. Bedzyk
Department of Materials Science and Engineering
Department of Physics
Applied Physics Program
Northwestern University

Professor Tobin J. Marks
Department of Chemistry
Department of Materials Science and Engineering
Applied Physics Program
Northwestern University

Final Examination Committee
Prof. Michael J. Bedzyk, Chair
Prof. Tobin J. Marks, Co-Chair
Prof. Mark C. Hersam
Prof. Robert P. H. Chang

Acknowledgements

Every journey comes to an end, and the end of a journey means the beginning of another one. At this particular moment of my life, what I remember the most is not the details of experiments or the challenges and obstacles that I have gone through, but the people who share the ride and enlighten my way. I would like to use this opportunity to express my deepest gratitude to those who supported, helped, and mentored me during my Ph.D. pursuit.

First and foremost, I would like to thank my two advisors, Professor Michael J. Bedzyk and Professor Tobin J. Marks. Mike and Tobin chose me as their first co-advised student back in the Fall of 2011. At that time, I was a puzzled Chinese student who left my hometown and home country for the first time in 22 years. I had very little knowledge about the research areas of each group as well as the project that I was going to work on. Fortunately, my professors are extremely patient and open-minded, and genuinely wish their students can succeed at NU and beyond. They not only provide necessary guidance whenever I need it but also give me sufficient freedom to find my own interests. Along the way, I have learned a lot from each of them. Professor Bedzyk teaches me the importance of critical thinking, the "spirit of the craftsman", and useful X-ray skills. Professor Marks shows me the intellectual curiosity and visionary perspectives. I will certainly remember all the lectures and lessons they taught me, and carry them in the next journey.

I would also like to say thank you to Professor Hersam and Professor Chang who served as my thesis committee members. Professor Hersam is very knowledgeable, passionate and diligent. He is also easily accessible and willing to share his thoughts on my research work even though I am not his student. Professor Chang is the team leader of IRG2. And I appreciate for all the advice he gave me during the memorable bi-weekly student meetings.

I feel privileged and fortunate to work and collaborate with many Bedzyk and Marks group members. Within Bedzyk group, I am particularly grateful for the guidance and friendship of Dr. Jonathon Emery and Dr. Sumit Kewalramani, who spent a lot of time mentoring me when I was a first-year student. Many thanks to Dr. Zhenxing Feng, Dr. Martin McBriarty, Dr. Curtis Leung and Dr. I-Cheng Tung for helping and advising me in my early years as well. I also feel very lucky to have so many amazing group members: Dr. Bor-rong Chen, Dr. Stephanie Moffitt, Xiao Chen, Boris Harutyunyan, Gavin Campbell, Liane Moreau, Changrui Gao, Janak Thapa, Kurinji Krishnamoorthy, Katherine Harmon, Anusheela Das, Dr. Bo-Hong Liu, Dr. Narayanachari and Dr. Guennadi Evmenenko. Special thanks to Dr. D.B. Buchhulz for the useful guidance on thin-film materials, and providing me high-quality samples throughout my entire projects. Special thanks to Jerry Carsello for all the help in the X-ray lab. Special thanks to Dr. Denis Keane and Dr. Qing Ma for their dedication, hard-working and assistance at sector 5.

I would also like to thank many collaborators, mentors and friends in Marks group: Dr. Jon Henneck, Dr. Jeremy Smith, Dr. Charles Song, Dr. Steve Loser, Dr. Ken Everaerts, Dr. Nanjia Zhou, Dr. Xinge Yu, Dr. Wei Huang, Dr. Hsueh-Chung Liao, Dr. Binghao Wang, Dr. Gang Wang, Dr. Xinan Zhang, Matt Leonardi, Katie Stalling, Brian Eckstein, Chen Yao, Aritra Sil, Amanda Walker and Dr. Riccardo Turrisi. They taught me so much in the field of chemistry.

Finally, I would like to acknowledge the teammates, collaborators and faculty members in IRG2: Prof. Peter Voorhees, Prof. Matthew Greyson, Prof. Julia Medvedeva, Prof. Vinayak P. Dravid, Prof. Gabriela Gonzalez, Dr. Peijun Guo, Dr. Mahyar Moghadam, Dr. Muhammad Islam, Dr. Jiajun Luo, Dr. Boya Cui, Dr. Rabi Khanal and Lintao Peng. It has been my privilege working with each of you, and I will always remember the time we spent together.

For My Parents

TABLE OF CONTENTS

LIST OF FIGURES

Chapter 1 : Introduction

1.1 Motivation

Portable electronic devices, such as laptops, tablets, smart watches, are considered to be one of the most influential technology innovations over the past 50 years. The next-generation electronics are anticipated to have more features, such as mechanical flexibility, optical transparency, and large-scale printability.[1-5] To meet the desired features, the development of the next-generation electronics relies on the invention of novel materials, exploration of new properties, and as well as the understanding of the fundamental structure-property relationship.

The tools for my research contain a variety of powerful synchrotron X-ray techniques. Compared to in-house X-ray sources, a synchrotron source possesses the advantages of higher brightness, tunable energy, and linear polarization. These advantages make it much easier to customize an experimental setup and perform *in situ* experiments, which allows for the observation and monitoring the chemical reactions or structure evolvement under controllable conditions. In this dissertation, I will employ synchrotron X-ray to characterize the novel electronic materials. To be more specific, I will: 1) explore the dipolar effects of the high-*k* molecules within self-assembled nano-dielectric (SAND)[6]; 2) structurally understand and differentiate the amorphous metal oxide semiconductors.[7]

Self-assembled nano-dielectric, known as SAND, has been invented and optimized at Northwestern University for the past decade.[6, 8, 9] SAND is usually made of 4 high-*k* organic /inorganic bi-layers on the top of a thicker prime oxide layer. It possesses high capacitance, low leakage current, ultra-thin thickness, and compatibility with many other semiconducting materials. SAND can be synthesized through solution-processing method at ambient environment, which makes SAND an ideal candidate for the large-scale and printable fabrication. However, despite the unique properties exhibited by SAND, some fundamental aspects of its dielectric behavior remain unexplored, namely the built-in polarity effects of the organic molecule and details of important geometrical parameters. Therefore, through this dissertation, I will elaborate the design and synthesis of a new organic molecule with an inverted dipole, discuss the effects from the incorporation of the new molecule into devices, and finally present a comprehensive X-ray structural analysis of tri-layer SANDs based on these two molecules.

The other focus will be the structure-property relationship of amorphous metal oxides (AMOs).[7, 10, 11] AMOs are important conducting/semiconducting materials widely used in modern electronics due to their excellent optical transparency, mobility, and mechanical flexibility. However, in this dissertation, I will focus on the thermal stability of AMOs. I will first compare and understand the thermal stability of In_2O_3 thin films grown at different deposition temperatures (T_d), and the crystallites orientation distributions of the after-annealed crystalline films. Along with the level-set simulation methods, important crystallization kinetic parameters are determined. I will later explore the effects brought by a variety of dopants: the increased thermal stability induced by doping Ga, Zn, and Sn; the local structure distortion resulted from cation sizes (Sc, Y and La), or polymer species (PVP, and PEI).

At the end, I provide some recommendations for possible future directions and include usefully instructions, such as operational manual, and Matlab codes, in the Appendices for the future reference.

1.2 Outlines

This dissertation will start with the introduction of TFTs (Chapter 2), including the basic structure and working principle of TFTs, the dielectric layer and semiconducting layer materials, and the common growth methods. The X-ray techniques are introduced in Chapter 3, which covers the basic theory behind each X-ray technique, and both qualitative and quantitative interpretation of the X-ray data. The X-ray standing wave measurement of the dipole inversion in self-assembled nano-dielectric (SAND) molecular layer is shown in Chapter 4. The Br counteranion position and distributions within two different molecules are determined through a suit of X-ray characterization tools. The deposition temperature effects on the pulsed laser deposition (PLD) In_2O_3 film crystallization process is shown in Chapter 5. The thin-film isothermal crystallization process is revealed via both X-ray measurements and level-set simulation. Furthermore, the thermal stability study of the doped In_2O_3 films is presented in Chapter 6. This chapter focuses on comparing the crystallization kinetics for each doping element at various atomic doping concentrations and the after-annealed crystalline film orientations. The microstructural alternations and overall density changes induced by doping metal ions or organic species are shown in Chapter 7. The recommendations for future work is shown in Chapter 8. And finally, some useful manuals are included in the Appendices.

Chapter 2 : Thin Film Transistor (TFT)

2.1: Introduction to Thin Film Transistors

The invention of transistors is one of the most influential technology breakthroughs within the past 100 years.[12, 13] Transistors exist in almost every aspect of our lives since they are the key components in the modern electronic devices, such as computers, smartphones, tablets, monitors, and laptops.[14] One common type of transistors is known as the thin-film field effect transistors (TFTs).[15, 16] The role of an TFT is mainly an on/off switch to allow electric current flowing to different parts of an electronic circuit, and enable various functionality.[17] For example, the most widely known application of TFTs is its implementation in the organic light-emission diode (OLED) or liquid crystal display (LCD) as the back-panel to drive the current for millions of pixels.[18, 19]

A TFT typically consists of a dielectric layer, a semiconductor layer, and three conductive electrodes with four common geometries.[16] As shown in Figure 2.1, this is a top-contact-bottom-gate TFT. The gate and dielectric materials can be a conductive Si wafer with the thermally grown 300 nm SiO_2 layer on the top. The channel layer materials can be metal oxides or organic semiconducting materials. The top source and drain contacts are normally thermal-evaporated Al or Au. A shadow mask with the pre-defined geometry can be used to control the dimension of contacts during the metal thermal evaporation process.

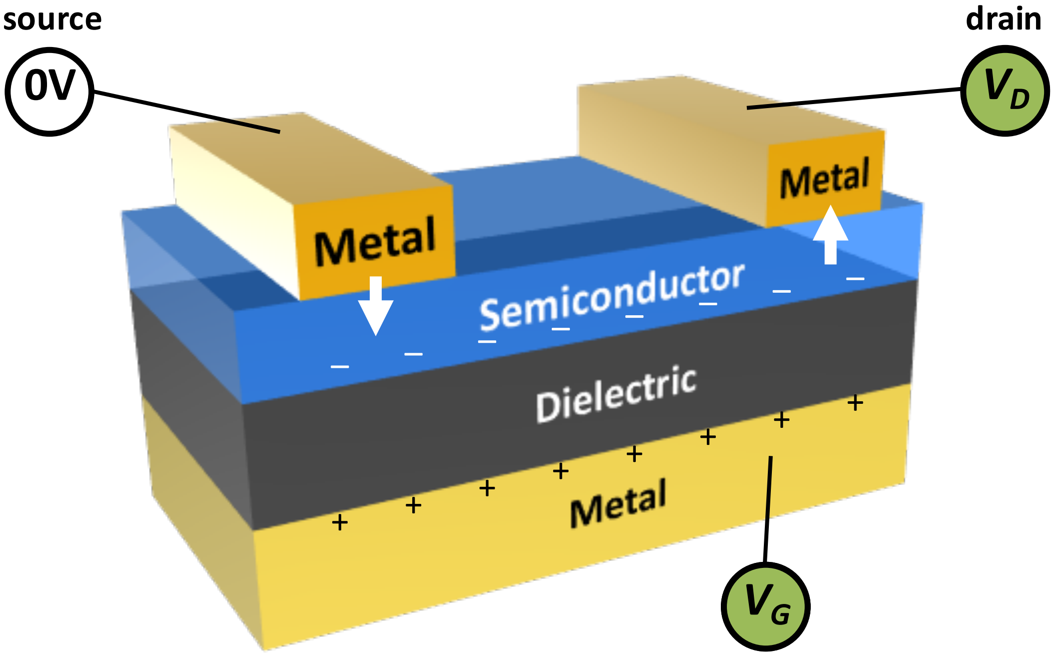

Figure 2.1: The schematic of the operation of thin-film transistors with a n-type semiconductor layer.

Here is how a typical TFT (Figure 2.1) operates. When a gate voltage (V_G) (between the gate and the grounded source electrode) is applied, negative charges will build up at the interface between the semiconductor layer and the dielectric layer. At the same time, if applying a voltage at the drain contact (V_D), the gate field-induced charges will flow and form the current I_{DS}. Note that Figure 2.1 uses an n-type semiconductor as the channel layer material. As stated above, a TFT is an on/off switch. Therefore, the operation of TFT typically requires a low off-state current I_{off}, and large on-state current I_{on}, compatibility with low working voltage, such as the battery (< 3V), and moderate operation mobility (μ).

2.2: The Characteristics of TFTs

A representative TFT transfer plot (red) is shown in Figure 2.2.[15] The relationship between the source and drain current I_{DS} and the gate voltage V_G can be expressed by Eq.2.1 and Eq.2.2, corresponding to the linear region and the saturated region respectively:

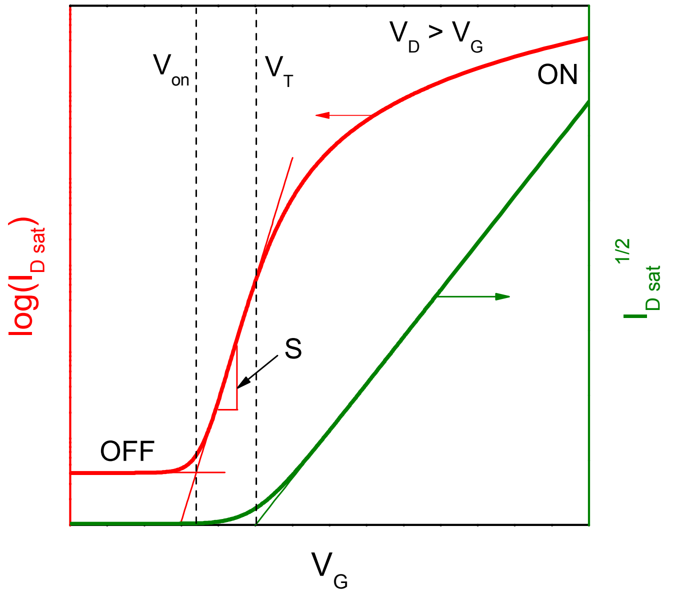

Figure 2.2: A representative TFT transfer curve. Courtesy of Dr. Jeremy Smith.

$$I_{DS} = \left(\frac{W}{L}\right) C_i \mu \left[(V_G - V_T) V_D - \frac{{V_D}^2}{2} \right], \tag{2.1}$$

$$I_{DS} = \left(\frac{W}{2L}\right) C_i \mu_{SAT} (V_G - V_T)^2 , \tag{2.2}$$

where the W and L are the channel width and length, C_i is the areal capacitance of the dielectric layer, V_T is the threshold voltage, and μ is the device mobility. The threshold voltage indicates the on-state voltage of a TFT device. From Eq.2.2, V_T equals to the value of V_G when $\sqrt{I_{DS}}$ is 0. The green line in Figure 2.2 presents the $\sqrt{I_{DS}}$ curve as a function of gate voltage (V_G). By extrapolating the linear region of $\sqrt{I_{DS}}$, the tangent dash green line intersects with axis where $\sqrt{I_{DS}}$

= 0, and the intersected voltage is V_T. The value of threshold voltage should be ideally zero. However, due to the existence of trap states at the semiconductor/dielectric interface, additional voltage is needed to induce charges to fill the trap states before turning on the device. The V_T could be either positive or negative depending on the carrier type (n or p) of the semiconducting layer.[16]

The turn-on voltage (V_{on}) is where I_{DS} starts to increase sharply depending on V_{GS}. It can be seen in the log(I_{DS}) plot (red). The subthreshold swing (S), defined in Eq2.3, is another useful parameter to assess how fast the device can be turned on in the subthreshold region.

$$S = \left(\frac{d\log\left(I_{DS}\right)}{dV_G}\right)^{-1}. \qquad \textbf{(2.3)}$$

Typically, a smaller S is preferable, resulting in lower power consumption and higher refreshing speed.

Another important characteristic is the on-off ratio (I_{on}/I_{off}). Ideally, this value should be infinity as no current should exist before the device is turned on. However, due to the intrinsic property of semiconductor material, I_{off} will not be zero. A small off-state current is necessary because this is related to the wasted power consumption, while a large on-current is also required so the device can operate under low-voltage (<10 V) and provide enough current for a circuit. The design of the on-off ratio should aim at > 10^4.

The areal capacitance is defined in Eq. 2.4, where the *k* is the dielectric constant, and *d* is the layer thickness. For some of the low mobility semiconductor material, a large capacitance is needed for low-voltage operation. This can be achieved by either replacing with the high-*k* material, or reducing the thickness or both. A series of dielectric materials named self-assembled nano-dielectrics (SANDs) will be introduced in the next section. As indicated above, normally 300 nm thermally grown SiO_2 is used as the reference dielectric layer material for the demonstration and comparison when the novel semiconducting material is the only focus of the research.

$$C_i = \frac{k\varepsilon_0}{d}. \tag{2.4}$$

At last, the mobility (μ) measures how fast the carriers (electrons or holes) can move under the applied electric field. The higher the value indicates fast current response under the same E-field intensity. It is certainly related to the fundamental structure of semiconductor material. For the past several decades, Si-based semiconducting materials, such as amorphous Si (a-Si:H), has dominated the display market. However, due to its low mobility, many researchers are seeking for the replacement, one of which is the amorphous metal oxide (AMO). And I will elaborate more in the future section.

In summary, the TFT transfer characteristics are important to evaluate the device quality. To achieve a desirable device performance, a deeper understanding of the materials is necessary. In the next few sections, I will proceed to some examples of dielectric materials and channel-layer materials.

2.3: Dielectric Layer Material

The dielectric layer in the TFT is of great importance as it directly affects the operation voltage of TFT device performance. As stated above, SiO_2 has been the most common gate dielectric material used in the modern electronic technologies. However, it fails to meet many requirements for the next-generation electronics: 1) SiO_2 has a relatively low dielectric constant (k = 3.9) which limits the optimal device performance; 2) SiO_2 is typically grown through the sputtering, CVD or thermal growth methods, which are high-cost and time-consuming. Moreover, the impressive advances in semiconductor materials such as carbon-based material (graphene,[20] carbon nanotubes[21]), high-mobility polymers[22], and transparent metal oxides (MO)[11] also require improvement of compatible gate dielectric materials. Therefore, many research has focused on developing and inventing new dielectric materials to replace SiO_2.[23] The replacing dielectrics should possess: 1) large dielectric constant and capacitance; 2) low trap density and leakage current; 3) compatibility with low-temperature growth and large-scale fabrication, such as solution processing or printing method. In the next section, I will elaborate on the self-assembled nano-dielectrics (SANDs).

2.3.1: Introduction to SAND

A self-assembled nano-dielectric (SAND) is a hybrid ultra-thin film, typically made of periodic high-k oxide layers and phosphoric acid-based π-electron (PAE) molecular layers.[6] SAND has shown to have high areal capacitance (750 nF/cm^2 ~1.1 μF/cm^2), low leakage current (~10^{-7} A/cm^2 at 2 MV/cm), low processing temperature ($\leq$ 150°C), high uniformity and low roughness, and the compatibility with large-scale fabrication under the ambient environment. The excellent performance of SAND is due to its hybrid nature which combines the advantages of both high-*k* oxide and organic material. High-*k* MOs, such as HfO_2, or ZrO_2 have been proven to be competitive candidates for the gate dielectric materials due to their exceptionally high dielectric constant and insulating properties.[23, 24] Recently, the increasing demands of flexible electronics favors the amorphous phase of MO since it is compatible with the low-temperature fabrication and resilient to the mechanical bending or cracking. However, this often results in a relatively large leakage current, and instability of device performance. The incorporation with high-*k* organic layer, such as PAE molecule in our case, compensates for the deficiencies of low-temperature synthesize MO dielectric, and enhancing the thermal and mechanical stabilities. Hence, the multilayers with alternating self-assembled monolayer and MO layer realizes a new class of robust dielectric materials for the next-generation electrical applications. The hybrid nature of these materials exploits the distinct properties of both the organic and inorganic components and have been incorporated into low-operating voltage flexible semiconductor-based OTFT/MOTFTs with enhanced performance.[6]

2.3.2: Fabrication of SAND-based Device

The SAND is synthesized via solution processing methods, and typically consisted of four oxide/PAE bilayers and a thicker bottom oxide prime layer. SANDs are prepared by multi-layer coating/self-assembly.[8, 9] Use a Zr-SAND precursor as an example. For the oxide layer, 100 mM ethanol solution of $ZrCl_2$ are prepared with the mixture of nitric acid, and DI water (molar ratio, metal chloride: HNO_3: H_2O=1:10:10) is then added under ambient conditions. The mixed precursor solutions are stirred overnight (> 12 h) to reach full hydrolysis. Prior to film deposition, 20 mM ZrO_x precursor solutions are prepared individually through dilution with ethanol. The first ZrO_x prime layer is synthesized by spin-coating the 20 mM $ZrCl_2$ ethanol solution on the substrate (typically Si substrate with native oxide) for 30 sec with 5000 rpm, and annealing in ambient environment for 30 min at 150 °C for film oxides film formation and densification. Then the ZrO_x-primed substrate is immersed in a preheated 3.0 mM phosphonic-acid based π-electron (PAE) methanol solutions for 1 h at 60 °C. After rinsing the coated substrate with methanol and blow-drying, the 10 mM ZrO_x precursor solution is spin-coated (30 sec, 5000 rpm) on, followed by 30 min annealing at 150 °C to form the ZrO_x layer. After repeating the self-assembly and ZrO_x layer synthesis for another three times, a Zr-SAND with desired thickness is produced. The Hf-SAND fabrication procedure is very similar but using a 70 mM $HfCl_4$ ethanol solution. For more information regarding to the synthesis of the PAE molecule, please refer to the previous publication.[6]

The procedure of the SAND-based TFT includes additional step of depositing semiconductor layer and thermally evaporated Au electrode. An example of SAND-based device and its electrical performance is shown Figure 2.3. Instead of presenting I_{DS} as a function of V_G (Figure 2.2), the drain/source current is plotted as a function of drain/source voltage for different fixed V_G (Figure 2.3(b)). Also, a p-type semiconductor is used for the channel-layer material so the transistor curve shown at the opposite side.

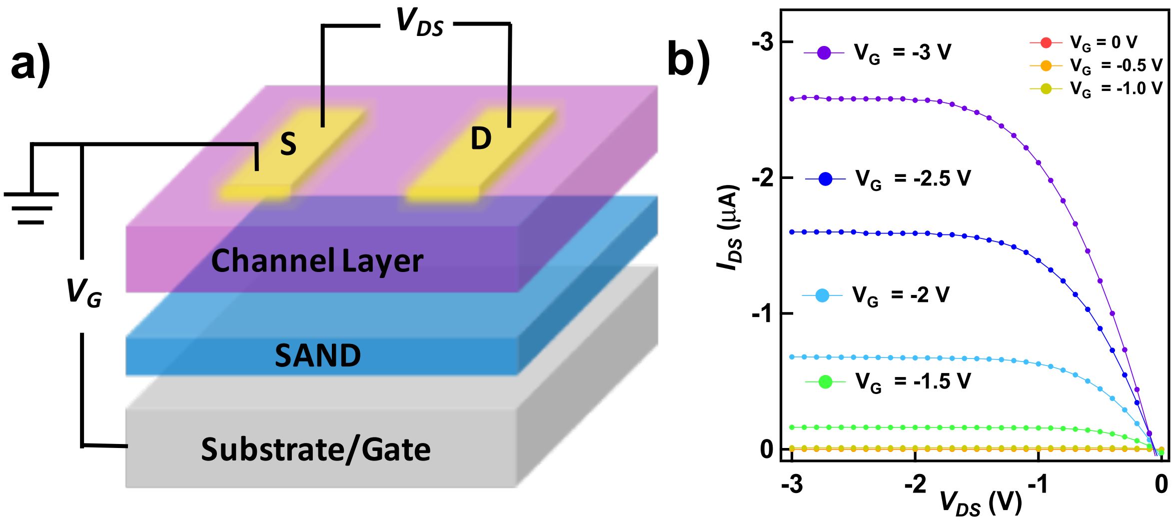

Figure 2.3: a) Structure of a typical bottom gate staggered TFT with Zr-SAND as the dielectric. b) A representative transistor curve of drain/source current I_{DS} as a function of drain/source voltage V_{DS} at multiple gate voltages V_G. (The TFT used pentacene as the semiconducting channel layer, and Zr-SAND as the dielectric.)

2.4: Channel-layer Materials

2.4.1: The Development of Channel-layer Materials

The development of electronics is also closely related to the innovation of the channel-layer materials. As shown in Figure 2.4, over the past 80 years, since the first invention of field-effect transistor (FET), every major advance comes along with the invention of new materials, such as the Si-based TFT in 1980s[25], the indium-gallium-zinc oxide (IGZO) based TFT in early 21 centuries[26], or more recently, the TFTs with the incorporation of novel low-dimensional materials (Graphene[20], MoS_2[27] and black phosphorus[28]). Some of these major technological innovations have already been widely used in our modern electronic devices and completely reshape our life.[29]

A retrospect of these highlighted materials can shed lights on how these breakthroughs are accomplished:

1) the effect of doping. Each element in the periodic table possesses its unique atomic structure and properties, and the combination of two or more atoms will facilitate the discovery of new properties. For example, the introduction of dopants (As or B) to a known system (intrinsic Si) leads to the formation of either n-type or p-type semiconducting Si. Another example would be the doping of Zn or Ga can tune the electronic properties of In_2O_3 from highly conductive to semi-conductive.

2) the exploration of surface or interface properties. When reducing the size of materials to nanometer scale, additional properties related to the surface or interface will start to dominate due to the dramatically increased surface to volume ratio. A good example would be 1-dimentional carbon nanotube (CNT) and 2-dimentional graphene exhibit drastic optoelectronic properties compared to 3-dimentional graphite or diamond.

3) the interplay of organic and inorganic materials. Inorganic materials tend to be more robust over time and less sensitive to the exposure of oxygen or moisture, and they typically have a more well-organized structure. However, organic materials also present a great potential

in replacing inorganic materials in many aspects, such as conductive polymers, organic light emission diodes (OLED). Therefore, instead of excluding one from the other, it would be more beneficial if the advantages of both organic and inorganic species can be selectively combined. Perovskite solar cell is an excellent example of combining methyl ammonium and lead halide groups to form a high efficient hybrid organic-inorganic light harvesting layer material.

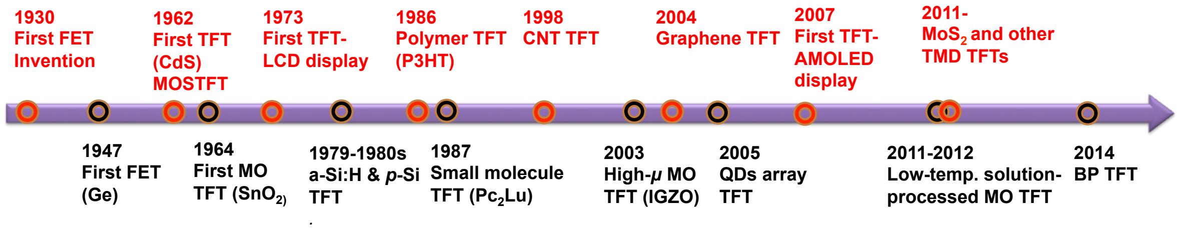

Figure 2.4: The channel-layer material evolution over the past 80 years. (Courtesy of Dr. Binghao Wang)

2.4.2: Amorphous Metal Oxide

As briefly mentioned above, over the decades, Si has dominated the transistor market. However, it does not meet some of the key requirements of the next-generation electronics, such as Si is opaque, the crystalline Si is rather brittle and not compatible with flexible substrates, and the cost is high. Amorphous metal oxides (AMOs)[10, 11, 26, 30, 31] as an alternative, have garnered much attentions over the past ~15 years due to their optical transparency, mechanical flexibility, and high mobility. And the advantageous features are summarized as follows:

- Optical transparency. AMOs typically are wide-bandgap (>3 eV) materials with transparency >80% over the visible-light range.

- Low processing temperature. AMOs can be fabricated at room temperature or low annealing temperature (< 300°C) to be compatible with flexible substrates such as plastic.[32-35]
- High uniformity and surface flatness. AMOs exhibit excellent uniformity and surface roughness (≤1 nm) owing to their amorphous structure. Unlike polycrystalline Si-based TFTs, they have limited applications due to the difficulty in large-scale fabrication raised by the inhomogeneity from the presence of grain boundaries.[5, 11]
- High electron mobility (n-type). Even though p-type AMOs are also promising, I limit the scope of my dissertation to only n-type semiconductors. AMOs can achieve a large and controllable Hall or TFT mobility (> 1 cm^2/Vs), which can be up to 50 cm^2/Vs depending on the growth methods and conditions. The high electron mobility is originated from the unique electronic structure of the metal oxides. The conduction band minimums (CBMs) are mainly consisted of large ns orbitals from the heavy metal cations (In, Zn and Ga, etc.), which have a large and spherical spatial spread with a broad CBM band dispersion. This results in a small electron effective mass m_e, and a larger mobility. More importantly, the above electronic structure also explains why high mobility can be maintained at the amorphous phase. The spherically distributed ns orbitals of metal cations overlap with the neighboring s orbitals and create a conduction path which is insensitive to the structural distortion presented in the amorphous phase.[26]
- Mechanical flexibility. Due to the lack of grain boundaries and overall amorphous nature, AMOs are more resilient to bending or compression in contrast to their crystalline counterparts. When the films under small strains (< 2%), the carrier mobility can be approximated as $\frac{\mu(R)}{\mu_0} = 1 + m\varepsilon$, where μ_0 and $\mu(R)$ are the mobility in flat

and bent condition with bending radius R, ε is the film strain, and m is an empirical constant. Previous studies reported that the value of m for IGZO-based TFTs is 0.5~2.7, which indicates that the mobility change within AMOs is relative insensitive to the mechanical strain. Whereas in either polycrystalline or amorphous Si-based TFTs, the absolution value of $|m|$ is much larger (> 15).[36]

- Compatibility with low operation-voltage and a variety of gate dielectric materials. Less defect states are formed within the AMOs compared to the conventional semiconductors such as Si, which allows for small S value (0.1 V/decade) and low operation voltage (< 5 V). Also, less defects states formed at the semiconductor/dielectric interface allow for more choices of gate dielectric materials. Many (HfO_2, SiO_2, Al_2O_3 and organics) have already been explored and demonstrated when incorporated them into the AMO-based TFTs.[37]

2.4.3: Growth Method

The metal oxides can be grown through either physical vapor deposition, such as puled laser deposition (PLD), atomic layer deposition (ALD) and sputtering, or via solution processing methods, such as spin-coating, spray-coating, inkjet printing and brush shearing. The growth conditions and methods directly determine the structure of the materials and their properties. In general, films synthesized through the physics vapor deposition are denser and have less defects and more stable device performance. However, the drawbacks of these methods are typically high-cost (expensive growth chamber and vacuum equipment, targets, and regular maintenance fee), time-consuming to reach the desired thickness and not compatible with large-scale fabrication. Whereas, the solution-processing methods allow for much faster deposition at low cost.

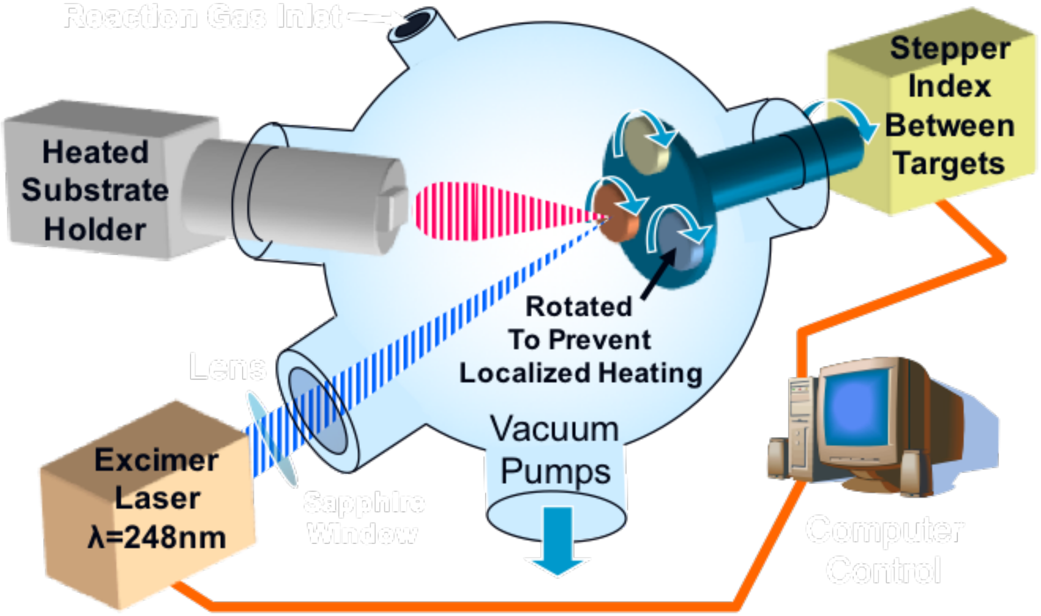

Figure 2.5: The multi-target pulsed-layer deposition (PLD) system. (Courtesy of Dr. D.B. Buchholz)

Both methods can grow films with a variety of crystallinity by controlling the deposition temperature or post-annealing temperature. Using the PLD deposited In_2O_3 film on quartz substrate as an example, the quartz substrate can be fixed at various depositions temperatures (T_d) during the deposition process.[33] If T_d is set above the room temperature (RT), crystalline films can be synthesized. More interestingly, when T_d is fixed below the RT (-100°C to 0°C), amorphous In_2O_3 can be grown. The as-deposited amorphous films can be transformed into crystalline phase if they are treated with post-annealing process (T_A). As for the solution-processing method, higher temperature (T_A >150°C) is typically needed for the evaporation of the solvents, overcoming the energy barrier for chemical reactions, and the calcination of the organic chemical residues. The time scale for the first two steps are a few seconds, but the last step could take up to a few hours until a high-quality film is achieved.

2.4.4: The Structure of MOs

Metal oxides (MOs) widely exist in the Earth's crust, and have been studied for decades since they are the key parts to many of the electrical, optical, and magnetic materials in our modern life. For example, the SiO_2, Al_2O_3 and HfO_2 for the dielectric materials;[23, 24] indium-tin oxide (ITO) is a common conductive electrode;[5] vanadium oxide and tungsten oxide are common catalysts; and $BaTiO_3$ is the well-known perovskite structure which exhibits unique piezoelectric property. In this dissertation, the In_2O_3-based *n*-type (semi)conducting materials and their structural and electrical investigation will be the main topic. This subchapter will focus on studying the crystal structure of the most representative binary, ternary and quaternary oxides system.

1) **Binary metal oxides (MOs)**

Since indium oxide is one of the most common AMOs, the understanding of its structure is of great importance. The most stable phase of indium oxide has a cubic structure (bixbyite, $Ia\overline{3}$, space group 206) with lattice constant a = 10.14 Å. Please see the following figures (Figure 2.6 - Figure 2.8) for the unit cell and polyhedral information. The unit cell has 32 indium and 58 oxygen atoms. The In atoms have two possible sites: b-sites (8 atoms, 25%) and d-sites (24 atoms, 75%). Each In atom is surrounded by 6 oxygen atoms and two interstitials, which form an octahedral structure with an average 2.18 Å In-O bond length. At the *b*-site, 6 oxygen atoms are located at the equivalent distance 2.18 Å. While at the *d*-site, the interstitials at the face diagonal positions lead to the local reorganization of three distances: 2.13, 2.19, 2.23 Å.

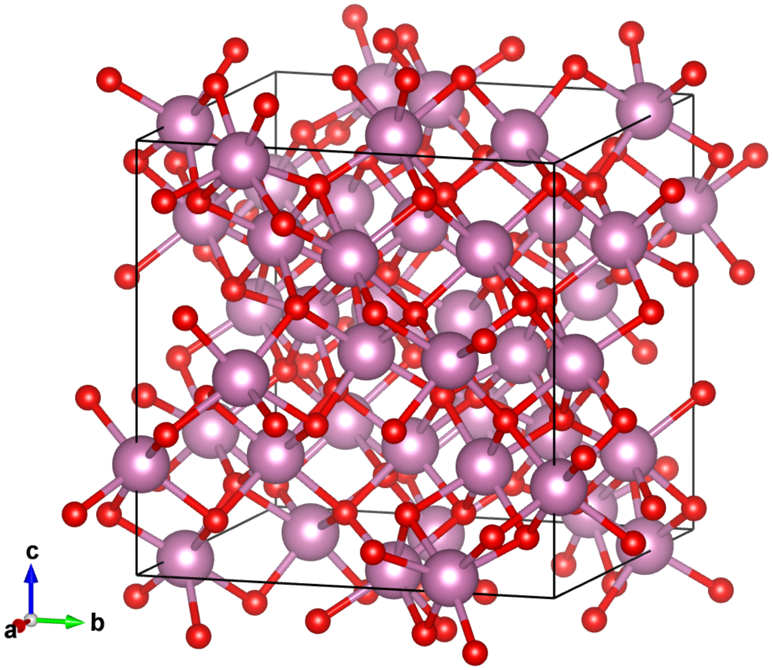

Figure 2.6: The crystal structure of cubic In_2O_3. In atom is labelled in purple and the oxygen atom is labelled in red.

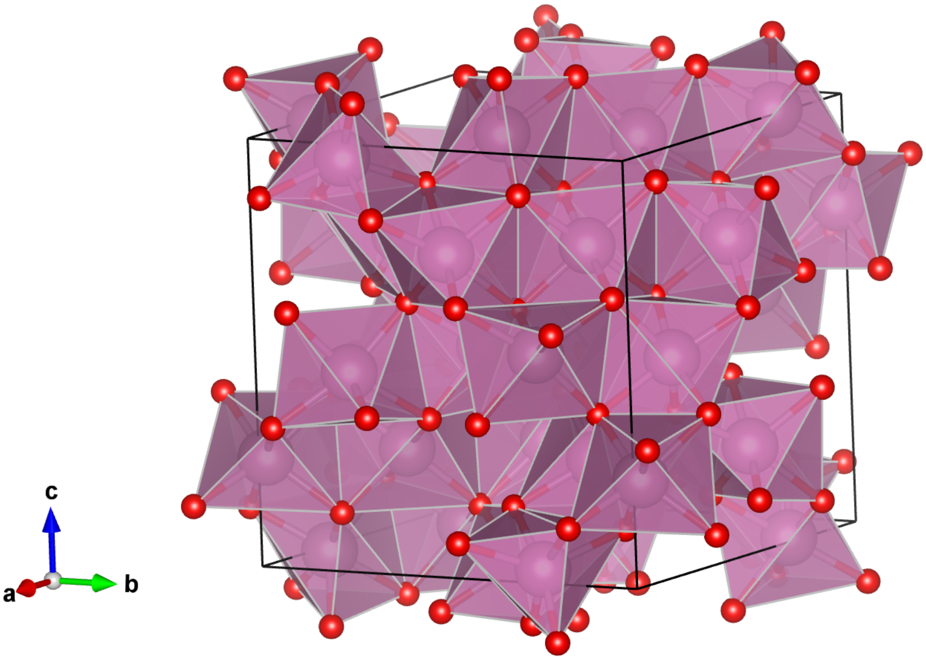

Figure 2.7: The polyhedral plot of cubic-phase In_2O_3. In atom is labelled in purple and the oxygen atom is labelled in red.

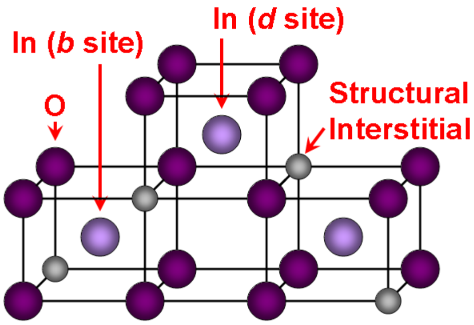

Figure 2.8: The depiction of two different In atom sites within the bixbyite structure. (From REF[38]).

The other possible phase of In_2O_3 is rhombohedral structure (space group 167, $R\bar{3}c$) with lattice parameters: a = 5.49 Å, b = 5.49 Å, c = 14.52 Å, and $\alpha = 90°$, $\beta = 90°$, $\gamma = 120°$ (Figure 2.9). The bulk In_2O_3 with rhombohedra structure is typically synthesized at high temperature and under high pressure while thin-film rhombohedral In_2O_3 can epitaxially grow on a single substrate such as sapphire.[39-41] The rhombohedral structure is rare in the products of the typical synthesis method since the temperature is not high enough to have the cubic to rhombohedra transformation. However, through the doping of secondary metal cations and/or annealing under certain environment, the rhombohedral In_2O_3 or doped In_2O_3 can be fully or partially transformed from the cubic phase.[42]

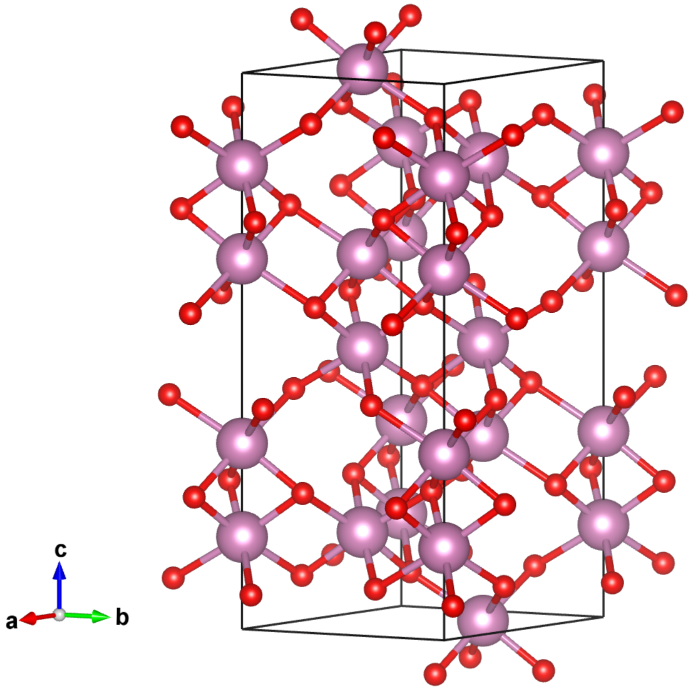

Figure 2.9: The crystal structure of rombohedral-In_2O_3. In atom is labelled in purple and the oxygen atom is labelled in red.

Tin dioxide (SnO_2) is another common transparent conducting oxide (TCO) material. The fluorine-doped SnO_2 (FTO) and indium-tin-oxide (ITO) (In:Sn=9:1) are two well-known TCO electrodes for numerous applications, such as, in solar cell fabrication. The 200 nm FTO coated on the glass is the standard transparent substrate. SnO_2 has a rutile structure (space group 136: P42/mnm) with the lattice parameters: a = b = 4.74 Å, c = 3.19 Å, and $\alpha = \beta = \gamma = 90°$ (Figure 2.10). Locally, each tin atom is coordinated with 6 oxygens forming an octahedral site with average Sn-O bond length 2.05 Å.

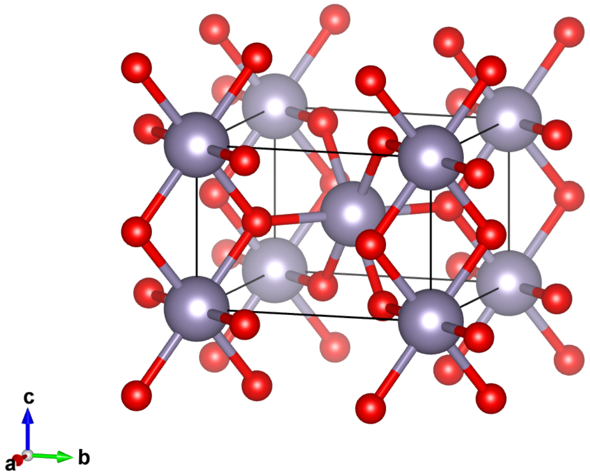

Figure 2.10: The crystal structure of SnO_2. Sn atom is labelled in grey and the oxygen atom is labelled in red.

Zinc oxide (ZnO) and its derivatives are common transparent semiconducting oxide materials. ZnO has the wurtzite structure (P63mc) and the unit cell consists of double-layers composed of zinc and oxygen atoms planes perpendicular to the c-axis (Figure 2.11). The lattice parameters of the ZnO unit cell are a = 3.25 Å and c = 5.21 Å. Each Zn atom is coordinated with

4 oxygen atoms with 1 bond of 1.96 Å (along with the c direction) and 3 bonds of 1.98 Å.

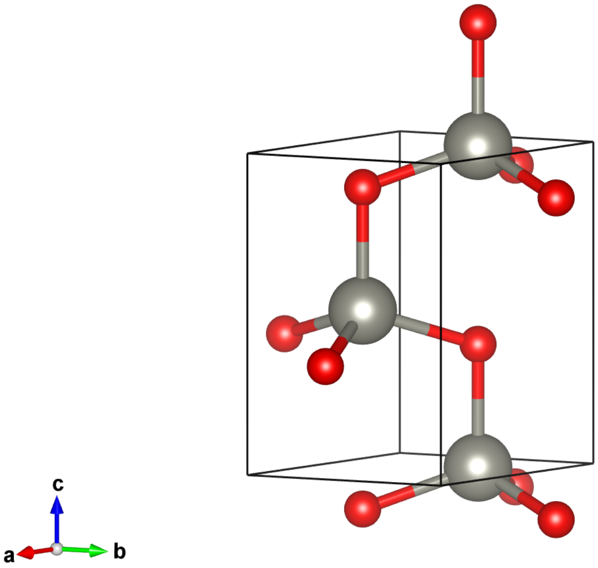

Figure 2.11: The crystal structure of ZnO. Zn atom is labelled in grey and the oxygen atom is labelled in red.

Gallium oxides (Ga_2O_3) have many polymorphs and the most stable phase is the *β*-phase. The lattice parameters of *β*-phase Ga_2O_3 are: a = 12.23 Å, b = 3,04 Å, c = 5.80 Å, and α = γ = 90°, β = 103.7°. Compared the above MOs, Ga_2O_3 is less explored since Ga cations are typically doped to the other MO systems rather than using Ga_2O_3 directly or as the host material. There are literatures showing Ga is the "oxygen getter", which facilitates the formation of oxygen vacancy in the amorphous matrix, and increase the carrier concentrations.[32]

2) Ternary metal oxides (MOs)

Even though binary MOs have many promising properties, the ternary or quaternary MOs are often used so the optimum performance can be reached.[5]

As stated above, there are two major categories of growth methods: physical vapor deposition and solution processing. For the former method, the formation of ternary or quaternary systems is typically achieved via periodically switching targets during the deposition process. Using PLD method as an example, to achieve ternary oxide films, a computerized shuttle is employed to alternate ablation between two targets, and the ratio of the pulses for each metal oxide in each cycle is adjusted to obtain the desired film composition. The film compositional uniformity is ensured since each single PLD pulse only deposits ~10^{12} metal cations/cm^2, which is < 1% of the total coverage requirement (0^{14}~10^{15} metal cations/cm^2) for a typical MO monolayer. Therefore, multiple pulses are required to deposit a single monolayer, and dopants can be uniformly dispersed down to the 1% level without additional aids on the diffusion of dopants. While for the solution processing methods, the dopants are added during the precursor solution preparation step. The composition can be tuned by controlling the concentration or volume of the metal cation precursor solutions. After the post-annealing, the metal cations will react with oxygen and form the oxides. Hence, the pre-determined the composition will be maintained in the synthesized materials.

Sn-doped In_2O_3 (ITO) is a transparent conductor with the very high optical transmissivity for visible light, and low electrical resistivity among all the doped indium oxides materials. The doping of Sn to a level of 5–10 at.% can produce 1~2x10^{21} /cm^3 carrier concentration and 1.5~2.0x10^4 Ω cm resistivity. At low Sn doping concentration (<20 at.%), the structure of ITO has been shown in many kinds of literature to have the identical crystal structure as cubic phase In_2O_3 and the Sn substitutes In in In_2O_3 matrix.[5, 43] This can be confirmed from X-ray diffraction patterns (XRD).

Zn doped In_2O_3 (IZO) is another TCO material that has been widely explored.[5, 44] Due to the high thermal stability of IZO (up to 500 °C), amorphous phase of IZO is typically used for industrial applications. With comparable properties to ITO as a TCO material, amorphous IZO has the advantages of being amorphous along with room temperature deposition, easy patterning and improved homogeneity relative to ITO, which have more potentials for fabricating the flexible device. The crystalline structure also varies depending on the doping percentage of Zn to the In_2O_3. At low doping concentration (<20 at.%), Zn is also considered to be the substitute of In within the cubic crystalline phase. Whereas at high doping concentration (> 20 at.%), rhombohedral IZO sometimes can be observed. At even higher concentration, the ZnO diffraction will dominate the overall crystalline structure.[45]

3) Quaternary metal oxides (MOs)

This section will cover two of most important quaternary metal oxides[44]: conductive zinc-indium-tin oxides (ZITO)[46, 47] and semiconducting indium-gallium-zinc oxides (IGZO)[26]. Both materials are transparent, and their amorphous phases are used in many areas.

One important motivation to search for the alternatives of historical ITO is that the increasing cost of indium metal because of its natural scarcity. Hence, zinc-indium-tin oxide (ZITO) has been invented as one of the alternative. $Zn_xSn_xIn_{2-2x}O_3$ ($x \leq 0.4$) is one of most commonly used quandary oxide as In_2O_3 doped with equal amounts of Sn and Zn. The indium amount is reduced through this co-doping strategy. Through both X-ray diffraction and electron microscopy measurement,[48, 49] ZITO has the common bixbyite structure as the In2O3 and ITO. However, under high temperature and at high post-annealing temperature, ZITO with rhombohedral phase can also be synthesized for a broad compositional range $0.2 \leq x \leq 0.7$.[46]

This is very similar to the discussion of the possible crystalline structures of In_2O_3 (section 2.4.4). The structure of an example of rhombohedral ZITO is shown in Figure 2.12, with lattice constant a = 5.36 Å, b = 5.36 Å, c = 14.322 Å, and $\alpha = 90°$, $\beta = 90°$, $\gamma = 120°$ and space group space group 167, $R\bar{3}c$. The lattice parameter is very similar to the rhombohedral In_2O_3 phase but has a smaller unit cell volume due to the smaller cation sizes of Zn and Sn compared to In. ZITO is also very thermally stable, and its amorphous phase can maintain high conductivity with the additional advantages brought by the reduced of grain boundaries mentioned above. There are reports to use ZITO as conductive electrodes for solar cell devices.[34]

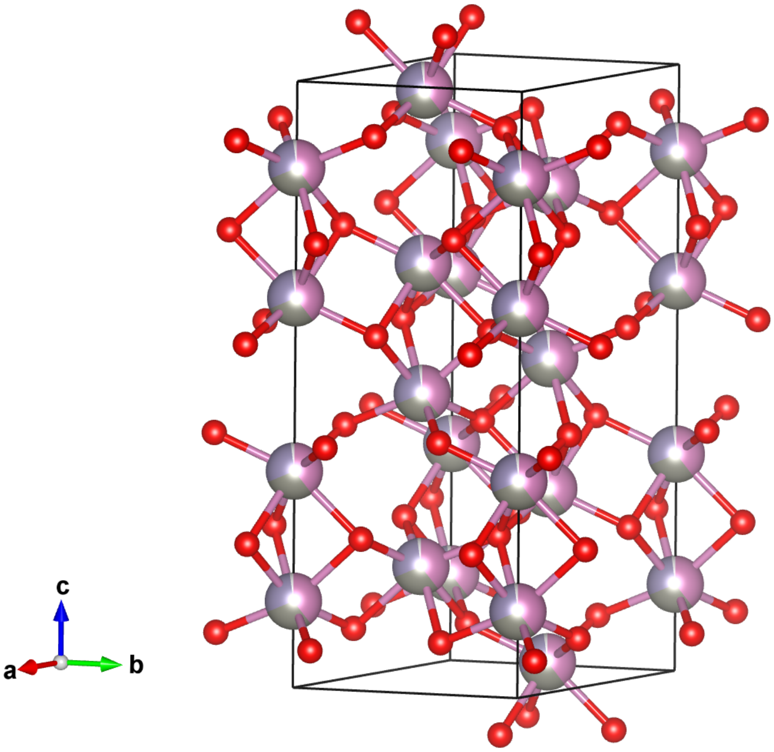

Figure 2.12: The crystal structure of $Zn_{0.6}In_{0.8}Sn_{0.6}O_3$. The oxygen atom is shown with small red sphere. The atomic site represented by the large sphere is shared between Zn, In and Sn based on the doping amount of each element.

IGZO chemical formula can be expressed as $InGaO_3(ZnO)_k$, where k=integer. It can have two possible structures based on the value of k. The structure can be either hexagonal for k = even, or rhombohedral structure for k = odd. An example structure from each case is shown in Figure 2.13a and b.

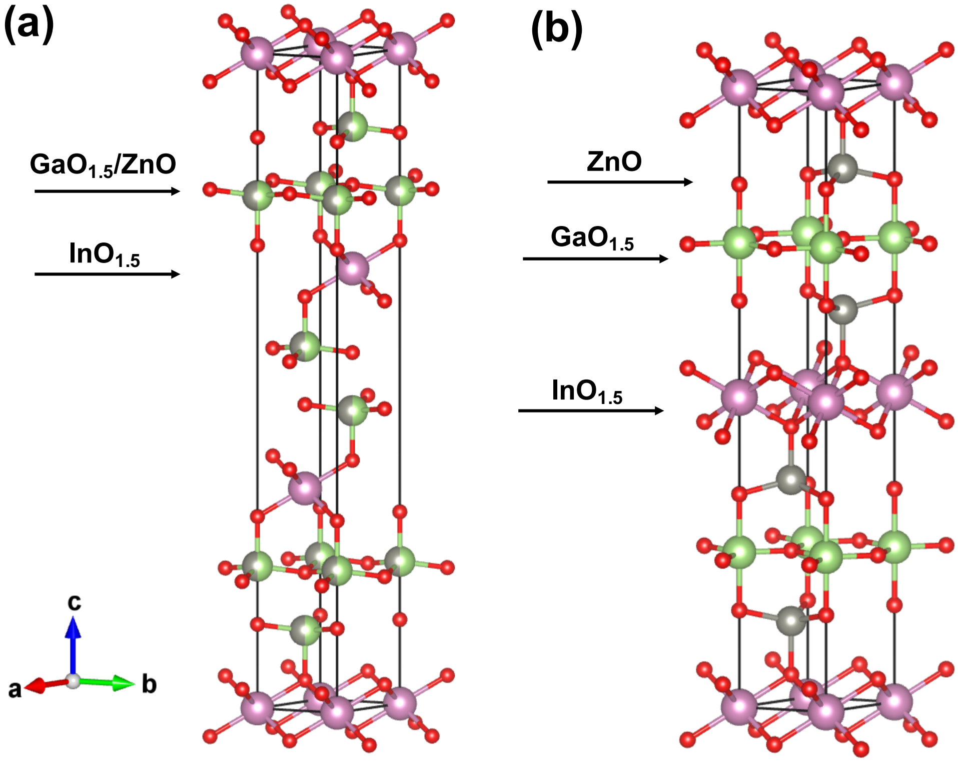

Figure 2.13: The crystal structure of $IGZO_4$ (a) and IGZ_2O_5.

The unit cell parameters of $IGZO_4$ (Figure 2.13a) are: a = 3.30 Å, b = 3.30 Å, c = 26.10 Å, and $\alpha = 90°$, $\beta = 90°$, $\gamma = 120°$ and space group 148, $R\overline{\mathbf{3}}$. Whereas, for IGZ_2O_5, the unit cell parameters are a = 3.29 Å, b = 3.29 Å, c = 22.53 Å, and $\alpha = 90°$, $\beta = 90°$, $\gamma = 120°$, and the space group 194, P 63/mmc. For both possible structures, alternating $InO_{1.5}$ layers and ($GaO_{1.5}$+$(ZnO)_k$) layers stack on each other with Ga and Zn sitting at the tetragonal site, and In sitting at the octahedral site.

The familiarization of crystalline structure is necessary for the understanding of amorphous materials. Typical structural characterization tools, such as XRD and electron diffraction, become less effective since the amorphous materials are lack of the long-range orderings. Hence, the structurally differentiation of two amorphous materials require alternative approaches. The following chapters, especially Chapter 7, will provide helpful discussions regarding the understanding of amorphous phase, especially from the local structure of metal cations.

2.4.5: The Electrical Properties of MOs

Part of the electrical properties of MOs, such as field effect mobility (μ_{FE}), has been described in the chapter 2.2 since MOs can be used as the channel layer material in TFTs. However, many intrinsic characteristics related to the thin film can be determined from Hall measurement: carrier type, sheet resistance (Rs: Ω/□), carrier concentration (n: $1/cm^2$), and carrier mobility (μ: $cm^2/V\cdot s$). These characteristics can be measured through the Hall measurement in the Van der Pauw configuration.[50] This measurement is generally more accurate for films thicker than 50 nm. For the standard field effect transistor (FET) application, the thickness of the MO layer is ~10 nm, and the field effect mobility is generally the electrical characteristic.

At last, I would like to briefly introduce the conductive mechanism in MO system. The oxygen vacancy is the one of key factors that tunes the electrical properties of AMOs. Using the Kröger-Vink notations, for n-type MOs, the generation of the doubly-ionized oxygen vacancy

($V_O^{\cdot\cdot}$) will produce two free electrons as carriers and oxygen gas[51]

$$O_O^{\times} \rightleftharpoons V_O^{\cdot\cdot} + 2e^{'} + \frac{1}{2}O_2(g)\,. \qquad \textbf{(2.5)}$$

Therefore, from the above equilibrium reaction (Eq. (2.5)), the carrier concentration can be increased under oxygen-deficient environment, such as low vacuum condition. In the PLD growth condition, this can be well controlled by different O_2 partial pressure inside the growth chamber. However, for films made by solution-processing methods, since most of experiments are made in ambient environment instead of in the oxygen-deficient one, the variation of device properties can be more profound. The humidity in the air, or the vacuum condition during the metal electrodes deposition can easily alter the device performance. Hence, it is necessary to monitor and keep every step under the same controllable condition from batch to batch to reduce the samples variation.

Chapter 3 : X-ray Characterization Techniques

3.1: Introduction

X-ray techniques are powerful characterization tools and extensively used in material science fields for structural and chemical analysis. X-rays are electromagnetic waves with energy (E_γ) from ~1 keV to 100 keV and wavelength (λ) ranging from ~0.1 Å to 10 Å, which is ideal to probe nm-scale materials. A typical lab source has X-ray wavelength corresponding to the characteristic wavelength of target materials, e.g. Cu Kα is 1.54 Å. A synchrotron is an alternative X-ray source that has much higher brightness, flux, and with tunable X-ray energy/wavelength. A brief introduction to the X-ray characterization techniques used in this dissertation will be given in this chapter.

3.2: X-ray Scattering Methods

3.2.1: X-ray Diffraction

When X-ray interacts with atoms of the materials, it is mainly scattered by the electrons and the scattering from the nucleus will be negligible (Born Approximation). Based on whether the energy of the X-rays is conserved or not, the scattering process will undergo either elastic or inelastic scattering. This section will concentrate on the elastic scattering, which covers the basic X-ray diffraction (XRD) and X-ray reflectivity (XRR). A brief introduction to X-ray diffraction mainly adopted from textbook by Als-Nielsen and McMarrow.[52]. Other helpful resources of the X-ray scattering can be also found in textbooks written by Cullity[53], or Warren[54].

The quantity that was used to describe the scattering process and determine the scattered intensity is the differential cross-section $d\sigma/d\Omega$, which calculates the number of X-ray photons

I_{sc} scattered by N particles per second per solid angle $d\Omega$:

$$\left(\frac{d\sigma}{d\Omega}\right) = \frac{\text{Number of X-rays scattered per second into } d\Omega}{(\text{Incident flux})\, N d\Omega} \ . \qquad \textbf{(3.1)}$$

For the scattering from one electron, the differential cross-section follows the classical Thomson scattering:

$$\left(\frac{d\sigma}{d\Omega}\right) = r_0^2 P \ , \qquad \textbf{(3.2)}$$

where r_0= 2.818 x10^{-5} Å is the classical radius of electron, and P is the polarization factor (the synchrotron source produces a polarized X-ray in the horizontal plane, and if the experiments are performed at the vertical scattering plane, then the polarization factor would be $P = 1$).

The next step calculates the cases for a group of electrons. Materials are consisted of atoms, and each electron of an atom forms an electron cloud around the nucleus with a density distribution $\rho(\vec{r})$. For an atom with Z electrons, the differential cross-section is not the simple sum of Z individual electrons but the supposition of contributions from different volume of electron clouds. *Atomic scattering* factor is defined to calculate the scattering from an atom:

$$f(\vec{Q}) = \int \rho(\vec{r}) e^{i\vec{Q}\cdot\vec{r}}\, d\vec{r}, \qquad \textbf{(3.3)}$$

where the $\vec{Q}$ is the momentum transfer or scattering vector. When the atoms form a molecule, the total scattering contribution from the whole molecule can be denoted as:

$$F(\vec{Q}) = \sum_j f_j(\vec{Q}) e^{i\vec{Q}\cdot\vec{r_j}}, \qquad \textbf{(3.4)}$$

where the $f_j(\vec{Q})$ is the atomic scattering factor of jth atom in the molecule, $\vec{r_j}$ is the relative displacement locating the jth atom and $F(\vec{Q})$ is named *structure factor*. Finally, from kinematical scattering theory, for X-rays scattered by a crystal, the structure factor is:

$$F(\vec{Q}) = \sum_{j} f_j(\vec{Q}) e^{i\vec{Q}\cdot\vec{r_j}} = \sum_{\overrightarrow{R_n},\vec{r_i}} f_i(\vec{Q}) e^{i\vec{Q}\cdot(\vec{r_i}+\overrightarrow{R_n})} = \sum_{\overrightarrow{R_n}} e^{i\vec{Q}\cdot\overrightarrow{R_n}} \sum_{\vec{r_i}} f_i(\vec{Q}) e^{i\vec{Q}\cdot\vec{r_i}}$$
$$= S_N(\vec{Q}) F^{u.c.}(\vec{Q}), \qquad \textbf{(3.5)}$$

where $\vec{r_j}$ can be represented as the sum of atom position $\vec{r_i}$ within the unit cell and the lattice vector $\overrightarrow{R_n}$, the $F^{u.c.}(\vec{Q})$ is the unit cell structure factor, *N* is the total number of unit cell and $|S_N(\vec{Q})|$ is the *3D* interference function. Then for a perfect crystal, the intensity that the detector received is:

$$I_{sc}\left(\frac{photons}{sec}\right) = \Phi_0\left(\frac{photons}{unit\ area \times sec}\right) r_0^2 P \left|F^{u.c.}(\vec{Q})\right|^2 N \frac{\lambda^3}{\nu_c} L, \qquad \textbf{(3.6)}$$

where the Φ_0 is the incident flux and ν_c is the volume of unit cell, and *L* is the Lorentz factor. Eq. (3.6) provides a mathematic approach to simulate, predict and fit the diffraction patterns.

The degree of crystallinity χ_c is a quantity from 0 to 1, which describes the factional volume of crystalline phase within a material. It can be determined by using Ruland's Method[28,29], which is the area under the crystalline peaks $I_c(Q)$ over the area under the entire diffraction pattern:

$$\chi_c = \frac{\int I_c(Q)dQ}{\int I(Q)dQ} \qquad \textbf{(3.7)}$$

3.2.2: Grazing Incidence Wide-angle X-ray Scattering

Single crystal substrates, such as silicon, $SrTiO_3$, etc., are often used in the thin film deposition. The films information would be buried under very strong substrate diffractions if we do a typical *θ /2θ* XRD measurement. One way to suppress the substrate signals and focus on the film is to employ grazing incidence wide-angle X-ray scattering (GIWAXS). X-ray refractive index n in material is defined as:

$$n = 1 - \delta - i\beta \,, \tag{3.8}$$

where δ is a quantity proportional to the density of material and the square of X-ray wavelength; while β is related to the X-ray absorption by the material. Since n has the quantity less than 1, the total external reflection will occur if incident angle α_i is less than critical angle α_c based on Snell's law. The evanescent waves will be formed below the scattering surface at this condition. X-ray penetration depth Λ can be calculated from following equation[52]:

$$\Lambda = \frac{\lambda}{4\pi}\left(Re\left\{(\alpha_c^2 - \alpha^2 + 2i\beta)^{1/2}\right\}\right)^{-1}. \tag{3.9}$$

Therefore, by tuning the incident angle α_i, X-ray penetration depth Λ can be adjusted to avoid the generation of a strong substrate diffraction peak. A typical GIWAXS setup is presented in Figure 3.1. The scattered X-rays are recorded by using a 2D detector with the advantage of collecting many diffraction patterns simultaneously. At the beamline, sample can be measured under controlled environment such as annealing or flowing reactive gas.

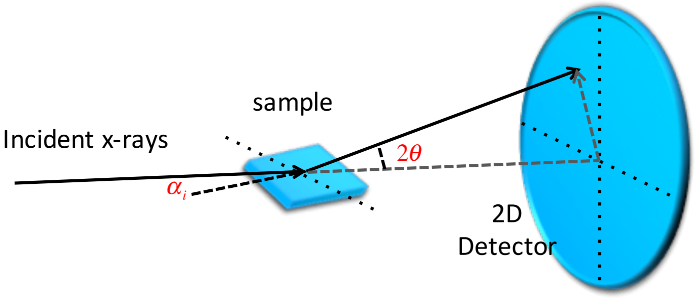

Figure 3.1: A schematic of the setup of GIWAXS experiment with an incident angle α_i.

An example of penetration depth Λ calculation is also plotted in Figure 3.2. Due to evanescent wave effect, the depth is close to 0 when the incident is below critical angle. To avoid X-rays penetrating to the substrate, the depth Λ should be less than the thickness of the film (300 nm), therefore, incident angle is set to be 1.5 times the critical angle to achieve (Λ = 250 nm).

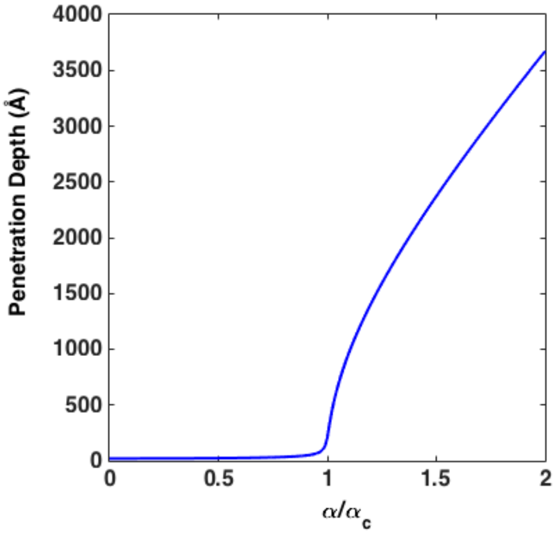

Figure 3.2: The penetration depth of 20 keV X-rays by varying incident angle α. α_c is the critical angle of In_2O_3 film.

3.2.3: X-ray Reflectivity

The studies of materials with multilayer structures are particularly important. The modern film growth techniques can tune the structures and properties of materials down to atomic or molecular level. Hence, an accurate measurement of structural information will be of great importance for the understanding, designing and fabrication of materials. For example, from eq. (2.4), the accuracy of capacitance value heavily relies on the thickness of each layer in 4-layer SAND (Figure 3.3c). XRR studies the scattering from interfaces and is sensitive to the electron density contrast between layers. Due to the large e-density contrast between metal oxides and organics of SAND, XRR will be an ideal characterization tool to measure the thicknesses of each layer based on eq. (3.10), where $\rho(z)$ is the electron density and $R_F(Q)$ is the Fresnel

$$\frac{R(Q)}{R_F(Q)} = \left| \int \frac{1}{\rho}\left(\frac{d\rho}{dz}\right) e^{iQz} dz \right|^2 . \qquad \textbf{(3.10)}$$

reflectivity. From $\rho(z)$, layer thickness, e-density of each layer, and interfacial roughness can be extracted. One example to show the utilization of XRR is to determine the spacing of IGZO on the top of 4-layer SAND structure (Figure 3.3).

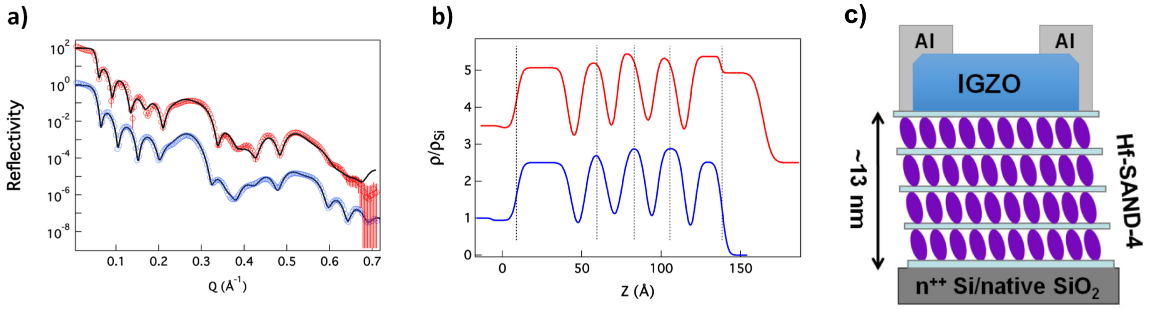

Figure 3.3: (a) XRR of a-IGZO-coated 4 layer Hf-SAND (red), and 4 layer Hf-SAND only (blue) on Si substrate substrate, respectively; (b) corresponding e-density profiles normalized to the bulk Si density; (c) device structure of IGZO on 4-layer Hf-SAND deposited on Si substrate. Adopted from REF[37].

3.3: X-ray Photoelectric Effect

The previous section has demonstrated how X-ray will be elastically scattered from a single electron, a molecule, a crystalline material, and at the graded interfaces. This section will focus on the photoelectric absorption process.

When an atom absorbs X-rays, it leads to the ionization of the atom and the emission of characteristic X-ray or Auger electrons as the excited atom (ion) goes to its ground state, and the excessive photon energy will be transferred to the photoelectron. A quantity to evaluate the ability to absorb X-ray is defined by linear absorption coefficient μ. When the incident X-ray energy is tuned from below the absorption edge energy to above the edge, linear absorption coefficient μ will have a sharp increase due to the annihilation of the incident photon. The ejected outgoing photoelectron wave will propagate and scatter back from the neighboring atoms. The backscattered waves will cause an interference effect with the outgoing waves, which lead to the presence of fine structures as a function of incident energy or wavelength at the absorption edge. Figure 3.4 shows the possible photoelectric effect and related X-ray techniques when X-ray is absorbed.

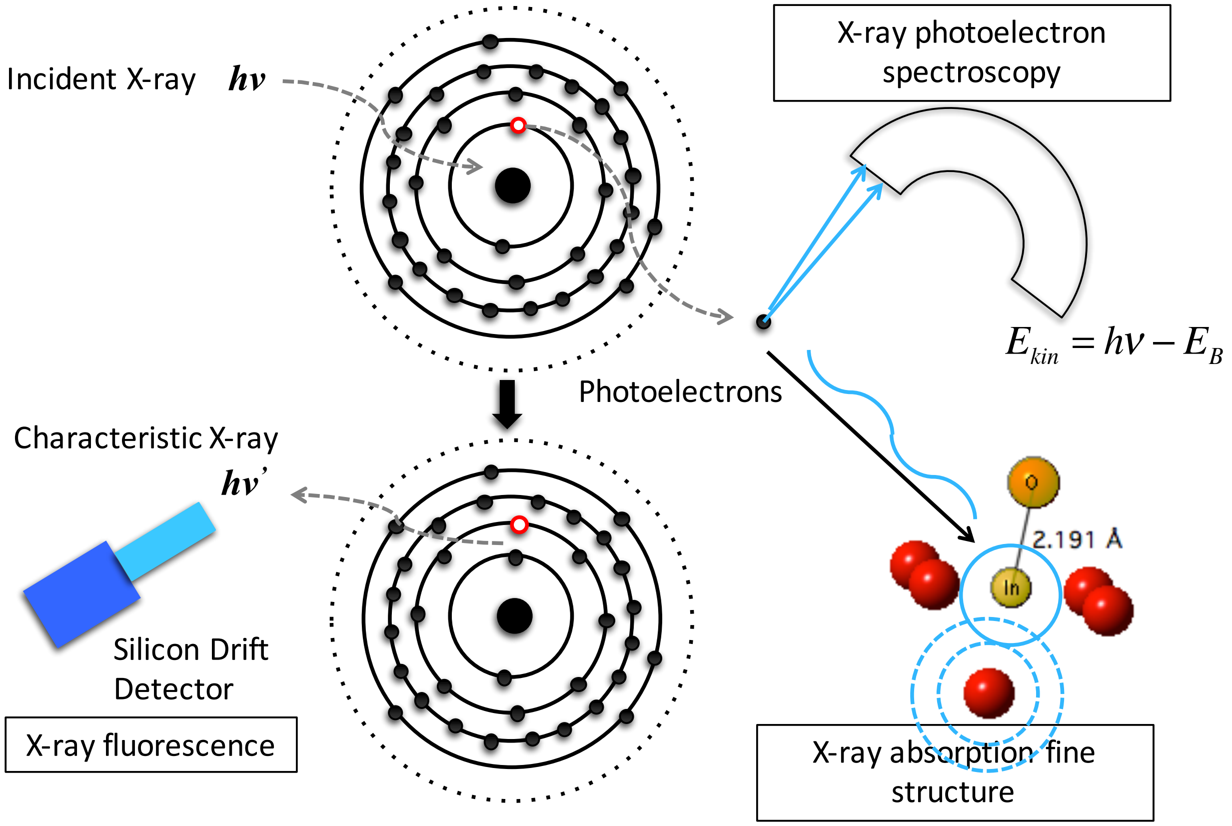

Figure 3.4: Illustration of X-ray photoelectric interaction with an indium atom.

3.3.2: X-ray Absorption Fine Structure

X-ray absorption fine structure (XAFS) is a useful technique to study the local environments around an atom of interest and has been widely used to establish structure-property relationships within transparent AMOs fields. For amorphous samples that lack of long-term orderings, XAFS is an ideal technique complementary to the pervious X-ray diffraction (XRD) measurements. Generally, XAFS spectra can be separated into two parts by the energy difference relative to the X-ray absorption edge energy: X-ray absorption near-edge structure (XANES) (-10 to 20 eV), which is sensitive to the chemical state and site symmetry; extended X-ray absorption fine structure (EXAFS), which can be analyzed quantitatively to gain the local structure information by fitting spectrum to the following equation:[55]

$$\chi(k) = \sum_i \frac{N_i(\theta)|f_i(k)|S_0^2}{kR_i^2} sin[2R_i k + \phi_i(k)] e^{\frac{-2R_j}{\lambda(k)}} e^{-2\sigma_i^2 k^2} \qquad \textbf{(3.11)}$$

where $\chi(k)$ is the normalized absorption coefficient; S_0^2 is the intrinsic loss factor; $e^{\frac{-2R_j}{\lambda(k)}}$ is the attenuation factor due to the electron mean free path $\lambda(k)$; $N_i$and R_i are the coordination number and bond distance of the ith shell of the absorbing atom; $f_i(k)$ and $\phi_i(k)$ are the backscattering amplitude and the phase shift; $e^{-2\sigma_i^2 k^2}$ is the Debye-Waller factor. The Fourier transformation of $\chi(k)$ can generate *pseudo*-radial distribution function (*p*-RDF) around the central atoms.

3.3.3: X-ray Photoelectron Spectroscopy

If a detector is placed to collect photoelectrons and analyze their kinetic energies E_{kin}, then bonding energy E_B can be deduced by Einstein relationship:

$$E_{kin} = E_{\gamma} - E_B - \phi_A, \qquad \textbf{(3.12)}$$

where E_{γ} is the incident X-ray energy, and ϕ_A is the work function of the analyzer. X-ray photoelectron spectroscopy (XPS) is widely used to study the chemical states and determine the composition of different elements of the films. The chemical states and compositions are determined by fitting XPS peaks. The peak position is corresponding to the bonding energy E_B. The peak area A_i will be used to determine the elemental composition C_i by following equation[56]:

$$C_i = \frac{A_i/S_i}{\Sigma({}^{A_i}/_{S_i})}, \qquad \textbf{(3.13)}$$

where S_i is the atomic sensitivity factor. Due to the relative low photoelectron, kinetic energy and large electron scattering cross section, XPS is more sensitive to the top surface of the films. Therefore, employing Ar ion gun to etch the surfaces oxides, and measuring the signals from deeper inside the films will give the bulk compositions.

The use of Ar ion gun will also enable “depth profiling” XPS measurement. By periodically etching the topmost surface and doing XPS on the freshly exposed surface within the selective area, we will be able to determine the compositional distribution from the original sample surface to the substrate.

An example of depth profiling result is provided in Figure 3.5. The sample is a perovskite film, which is spin-casted onto FTO coated glass substrate. The result shows that the film is completely etched since the strong Sn signals from the FTO layer are observed at the end of the profiling. This study shows that the surface is Cl rich; while I is mainly located at the lower part of film.

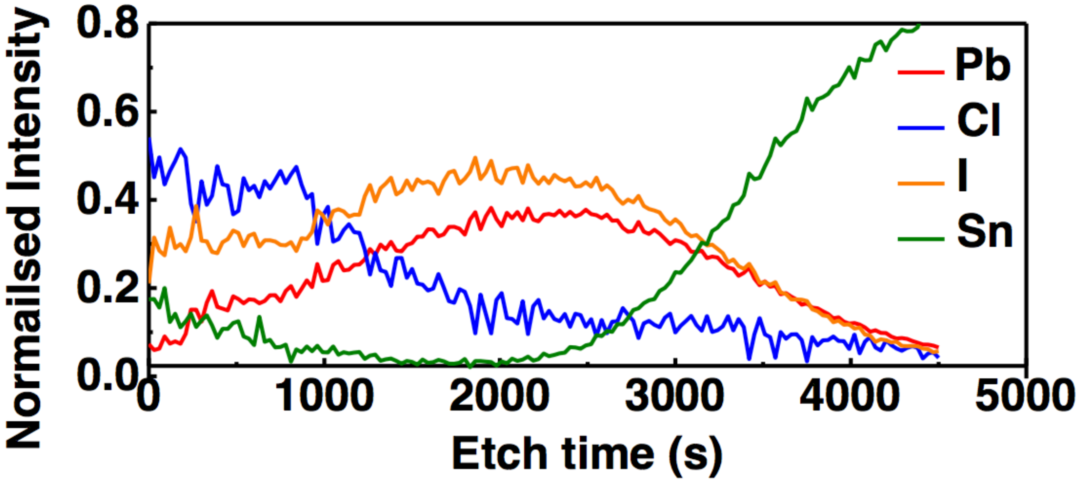

Figure 3.5: Depth profile of perovskite film coated on an FTO substrate obtained by XPS *in situ* with ion sputtering from REF[57]

3.3.4: X-ray Fluorescence

If the characteristic X-ray signals are collected and analyzed by the X-ray fluorescence (XRF) detector, it will also be possible to determine both the relative and absolute composition information from the fluorescence X-ray intensities. For the absolute coverage measurement, a standard with the known elemental coverage are measured at the same geometry with the unknown sample. By comparing the area A_s under the fluorescence peaks, the coverage of elements inside the films can be determined by using eq. 3.14:

$$C_s = \frac{A_s}{A_{std}} \frac{\sigma_{std}(E_\gamma)}{\sigma_s(E_\gamma)} \frac{T(E'_{std})}{T(E'_s)} C_{std} \, , \qquad \textbf{(3.14)}$$

where C_{std} is the coverage of standard; $\sigma_{std}(E_\gamma)$ and $\sigma_s(E_\gamma)$ are the cross-sections for element in standard and sample element at incident X-ray energy E_γ; $T(E'_{std})$ and $T(E'_s)$ are the transmission of X-ray path (usually the air absorption) and detector efficiency when measuring characteristic fluorescence X-ray from the standard E'_{std} and sample E'_s.

The relative coverage or composition of a sample can also be determined following the same method. The eq. 3.14 can be modified to:

$$\frac{C_A}{C_B} = \frac{A_A}{A_B}\frac{\sigma_B\left(E_\gamma\right)}{\sigma_A\left(E_\gamma\right)}\frac{T(E_B')}{T(E_A')}\ . \tag{3.15}$$

3.4: X-ray Standing Waves

Modern surface science has already been shrinking down the measurable scale to nm-scale. At this length scale, surface properties will dominate instead of bulk properties. Therefore, the understanding of surface structures will be of great importance for future theoretical interpretation, property optimization, and future applications of the materials. X-ray standing wave (XSW) is a surface sensitive technique, which can be used to investigate the structural information with Å-scale resolution.[58-60] The X-ray standing wave (XSW) is generated by the interference between the incident and Bragg reflected X-rays This stationary X-ray wave field, as a source of excitation, will cause X-ray photoelectric effect and related processes, such as X-ray fluorescence (XRF), to have a cross-section proportional to the XSW intensities. Since these intensities of XSW are spatially modulated, the intensities of XRF signals will depend on whether the scattering atoms are located at the maximum or minimum of the XSW. Therefore, XRF of the atoms will contain the phase information of the XSW fields, and the analysis of fluorescence yields will provide two important parameters, coherent faction *f* and coherent position *P* of a specific element.[61-63]

The method in this dissertation will be focusing on Bragg diffraction from a periodic layered synthetic microstructure (LSM) (Figure 3.6)[64-66]. Alternating amorphous or polycrystalline high-Z and low-Z materials are deposited on Si substrate by sputtering deposition method with a periodic d-spacing ranging from 15-200 Å and 10-200 layer pairs. Since LSMs are synthetic and can be customized based on the experimental needs, it provides a large visibility to probe various elements within a larger distance from the silica surface.

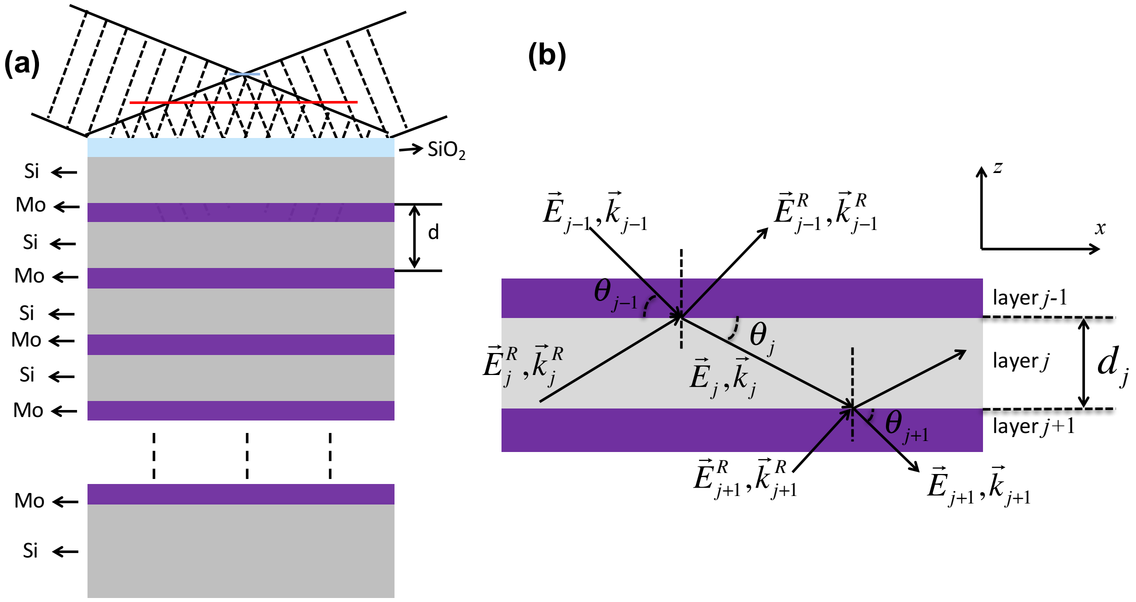

Figure 3.6: (a) A schematic picture of layer synthetic microstructures, and the generation of XSW above the silica surface; (b) The reflected and refracted E-field plane waves at two successive boundaries in a multilayer.

The XSW period is $D = 2\pi/Q$, where $Q = 4\pi \sin\theta/\lambda$ is the scattering vector, λ is the X-ray wavelength, and θ is the incident angle. In addition to the XSW period decreasing as Q (or θ) is advanced, the XSW phase, υ, also decreases by π radians as the incident angle θ is scanned across the TER and Bragg reflection regions. This causes an inward shift (along the z-axis) of the XSW *E*-field intensity, which can be approximated with the 2-beam interference function[67] as:

$$I(\mathrm{Q}, \mathrm{z}) = 1 + R + 2\sqrt{R}\cos(\upsilon - \mathrm{Q}\,\mathrm{z}). \tag{3.16}$$

While the X-ray fluorescence (XRF) yield, from each XRF-selected elemental distribution profile, $\rho(\mathrm{z})$, is

$$Y(\mathrm{Q}) = \int I(\mathrm{Q}, \mathrm{z})\,\rho(\mathrm{z}) dz\,. \tag{3.17}$$

Eqs. (3.16) and (3.17) can be calculated by a modification[60] to Parratt's recursion formulation (Figure 3.6b).[68] A more rigorous derivation, which we use for analyzing the data, takes into account refraction and absorption affects, is described elsewhere.[60]

Chapter 4 : Measuring Dipole Inversion in SAND Molecular Layer

4.1: Introduction

Thin-film transistors (TFTs) based on both organic (OTFTs) and inorganic metal oxide (MOTFTs) semiconductors are important candidates for the next-generation thin film electronics owing to their unique properties,[10, 17],[26] and make OTFT/MOTFTs ideal components for large-scale fabrication of several unconventional devices such as flexible displays [22, 69, 70], biocompatible circuits [71, 72] and chemical sensors [73]. However, despite these advantageous properties, there are some key limitations needed to be solved, such as the large operating voltage caused by the low capacitance of most common solution-processable organic dielectrics used for OTFT fabrication and high processing temperatures of those used for MOTFTs. [10, 31] (Chapter 2.3)

The basic working principle has been introduced in Chapter 2.[16] Typical TFT-based display technologies operate at < 20 V, and for portable/wearable electronic devices as well as radio-frequency systems, much lower operating voltages are required. Hence, for a given μ larger TFT currents can be achieved at low voltages if the gate dielectric capacitance (C) is sufficiently large. Since C is defined as $C = k\varepsilon_0/d$ (eq. 2.4), the capacitance can be increased by either using relatively high-k materials ($k > 10$), by reducing d, or a combination of the two. Several high capacitance materials were developed for both OTFTs and MOTFTs, such as high-k polymers[74-76], high-k metal oxide dielectrics[24, 77, 78], and ultra-thin self-assembled monolayers[16, 79, 80]. Our group has developed a unique type of robust nano-scale dielectric SANDs. Please refer to Chapter 2.3 for more information.

4.2: PAE vs IPAE

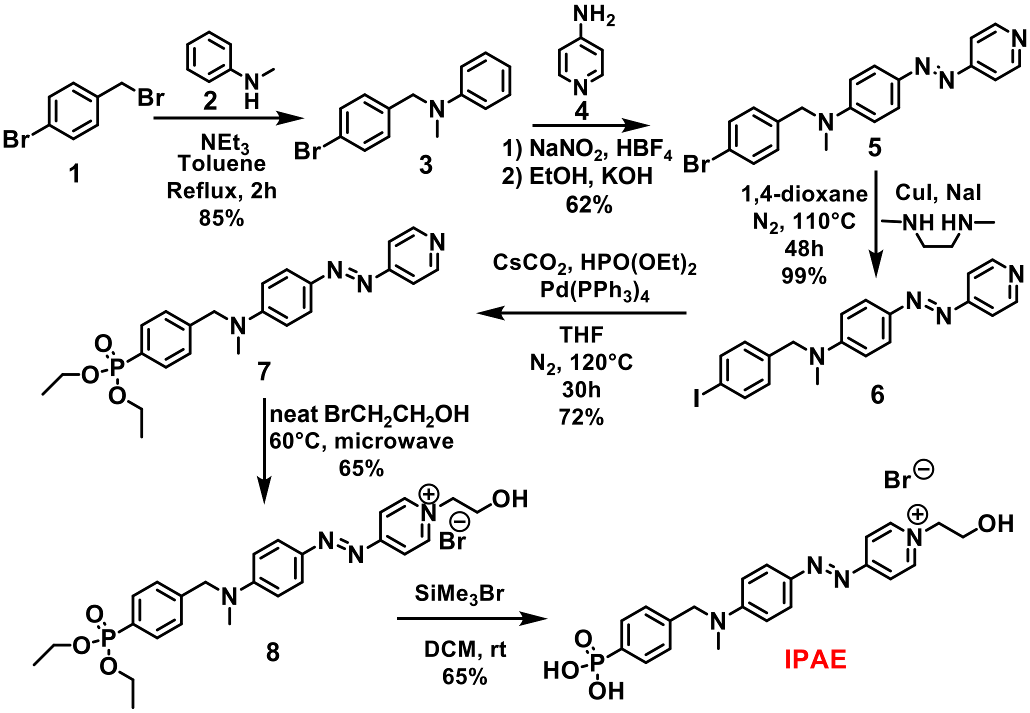

Figure 4.1:The synthesis route of IPAE molecule. This figure is from a submitted manuscript REF[81]

The electrical behavior of SANDs has been studied in context of the chemical and structural aspects of their molecular/inorganic components.[6] The focus will be on the fundamental aspects of dielectric behavior that remain unexplored, namely the built-in polarity effects of the PAE molecule and details of important geometrical parameters. Our research will also serve to clarify findings from previous reports on how the dipolar character of a self-assembled monolayer (SAM) affects the OTFT device performance. [82-86] Typically, depositing a SAM on an oxide surface is known to decrease the leakage current and reduce interfacial traps between the channel layer and dielectric layer. [87, 88] In particular, a well-ordered SAM forms a dipolar layer that can alter and modify transistor parameters, particularly the threshold voltage (V_T), and induce a gate potential shift by $\Delta V_T \sim NP_{\perp}/\varepsilon_0 k$, where N is the surface packing density, k is the dielectric constant of the SAM, and $P_{\perp}$ is the molecular dipole along the molecular long axis.[83, 89] Therefore, controlling the magnitude and direction of $P_{\perp}$ in a fabricated device is an important design criteria for next-generation electronics.[89-91]

To this end, we recently designed and synthesized a new molecule, IPAE, which is similar to PAE in structure but possesses an "inverted" bond connectivity (Figure 4.1).[81] Note, PAE and IPAE molecules both consist of a positively charged π-conjugated stilbazolium unit associated with a bromide (Br^-) counteranion for neutrality. Replacing PAE with IPAE during the self-assembly step of dielectric fabrication yields an inverted SAND (I-SAND) multilayer structure with an inverted dipole moment caused by flipping the molecular building block's regiochemistry. We recently found that the 4-layer ISAND exhibits a 40% higher k value for the organic layer ($k_{\text{IPAE}} \sim 13$, whereas $k_{\text{PAE}} \sim 9$) and a 10% increased areal capacitance ($C_{\text{I-SAND}} \sim 503$, whereas $C_{\text{SAND}} \sim 465$ nF cm^{-2}) in comparison to the typical 4-layer Zr-SAND. [81, 92] OTFTs fabricated based on inverted Zr-SAND (IZr-SAND) with *p*-type and *n*-type semiconductors also exhibit sizable shifted threshold (V_T) and turn-on (V_{on}) voltages compared to those based on conventional Zr-SAND.[81] These significant changes were rationalized by the built-in polarity changes created by switching the organic component from PAE in the SAND to IPAE in I-SAND. A deeper understanding on the origin of this "polarity switch" requires a molecular/atomic-scale characterization that can structurally differentiate between the PAE- and IPAE-based SANDs. In particular, the behavior of the halogen counteranion associated with each of these two building blocks is of great importance because it allows us to identify the negative portion of each molecule, the molecular orientation and to understand the dipole inversion and self-assembly deposition process. This information is essential to correlate changes in charge transport with dipole-semiconductor interactions, which will ultimately lead to a better design and engineering of future SAND-based devices.

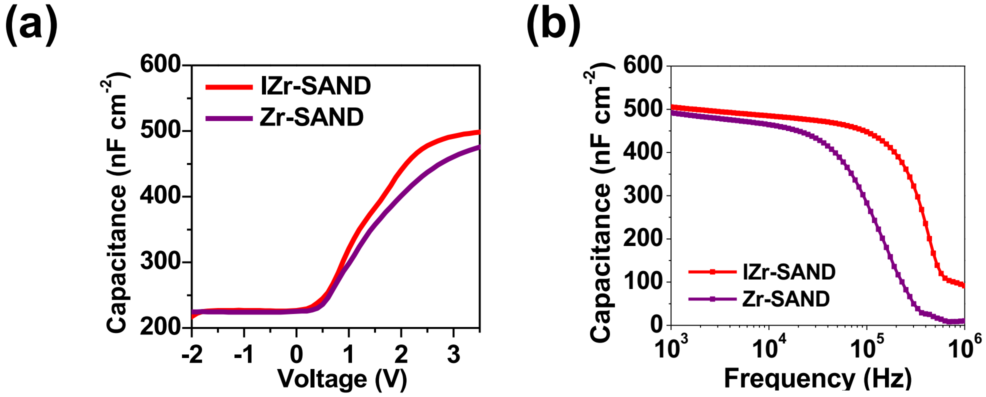

Figure 4.2: Capacitance measurements as a function of applied voltage (a) and frequency (b) for 4-layer Zr-SAND and IZr-SAND. Figure is adopted from REF[81]

4.2: Sample Preparation

To reduce the complexity in structure that would arise from a typical 4-layer structure, we designed a direct measurement to comprehensively analyze and compare the structure and halogen counteranion distribution in a single layer SAND and I-SAND. A trilayer SAND or I-SAND design containing a single PAE or IPAE layer sandwiched between a Zr oxide layer as the bottom prime layer and Hf oxide layer as the capping layer (as indicated in Figure 4.3) is utilized to facilitate structural analysis. The SAND or I-SAND trilayer films (Figure 4.3) were grown on Si substrates for XRR analysis and on Si/Mo multilayer substrates for XSW analysis. Both substrates possessed a native SiO_x surface layer. The sputtered multilayer substrate, which was designed to generate strong multilayer Bragg reflections, had 60 Si/Mo bilayers (period d = 6.0 nm with Si: ~4.5 nm and Mo: ~1.5 nm) with Si as the topmost layer.[64-66] Additional details about the synthesis of the trilayer SAND/I-SAND and Si/Mo multilayer substrate are described in the supporting information (SI). Dielectric films were grown with the same procedure on Si and Si/Mo so that the XRR-determined electron density profile could be directly compared to the XSW-determined Hf, Br and Zr atomic distribution profiles for the same film. XRF measurements of the Hf, Br and Zr coverages were made on Si/Mo substrate samples.

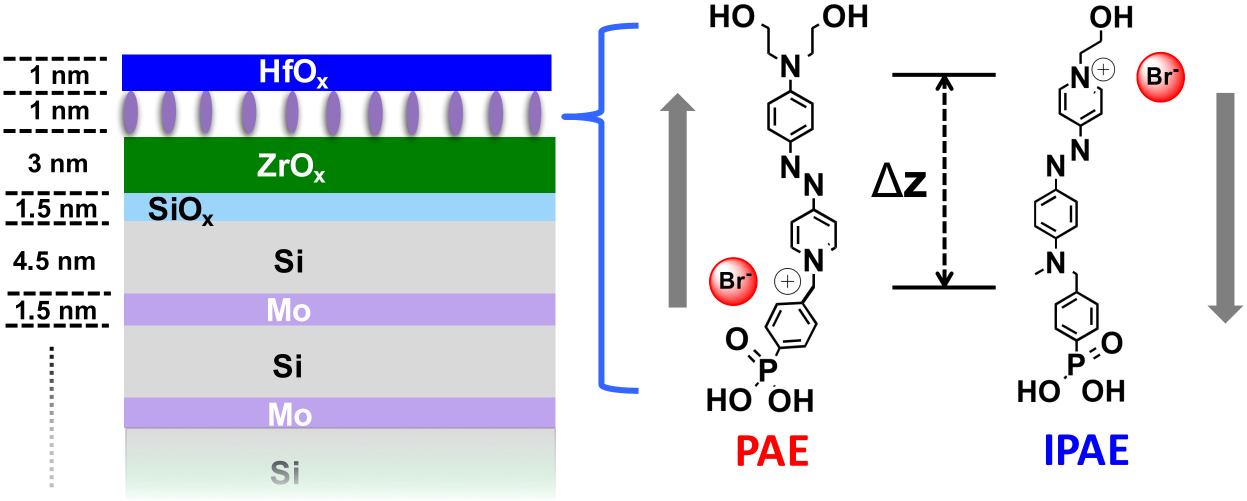

Figure 4.3: Side-view depiction of multilayer thin film structure with a HfO_x / PAE or IPAE / ZrO_x SAND trilayer deposited on the SiO_x top-layer of a Si/Mo periodic multilayer. The grey arrow indicates the polarization direction. The Br^- counteranion layer height difference is indicated by **Δz**.

4.3: XSW Experiment at 33BMC

All X-ray measurements were performed at the Advanced Photon Source (APS) station 33BM-C, where a Si(111) monochromator was used to select an 18.5 keV incident X-ray beam energy, suitable for exciting Br K, Hf L and Zr K XRF, while avoiding the strong Mo K XRF from the multilayer. In the XSW measurements, XRF spectra were collected at each incident angle with a Vortex silicon drift detector (SSD). The reflected X-rays for the XRR and XSW measurements was collected with a Pilatus 100K area detector. The intensity of reflected X-rays and background diffuse scatterings were recorded by setting region of interests (ROIs) on the area detector. The samples were kept in an inert, flowing He gas atmosphere throughout the experiment (Figure 4.4a). A typical XRF spectrum collected during XSW (at $\theta = 0.25°$ and $Q = 0.82\ \mathrm{nm}^{-1}$) measurement from the SAND on Si/Mo was shown in Figure 4.4b.

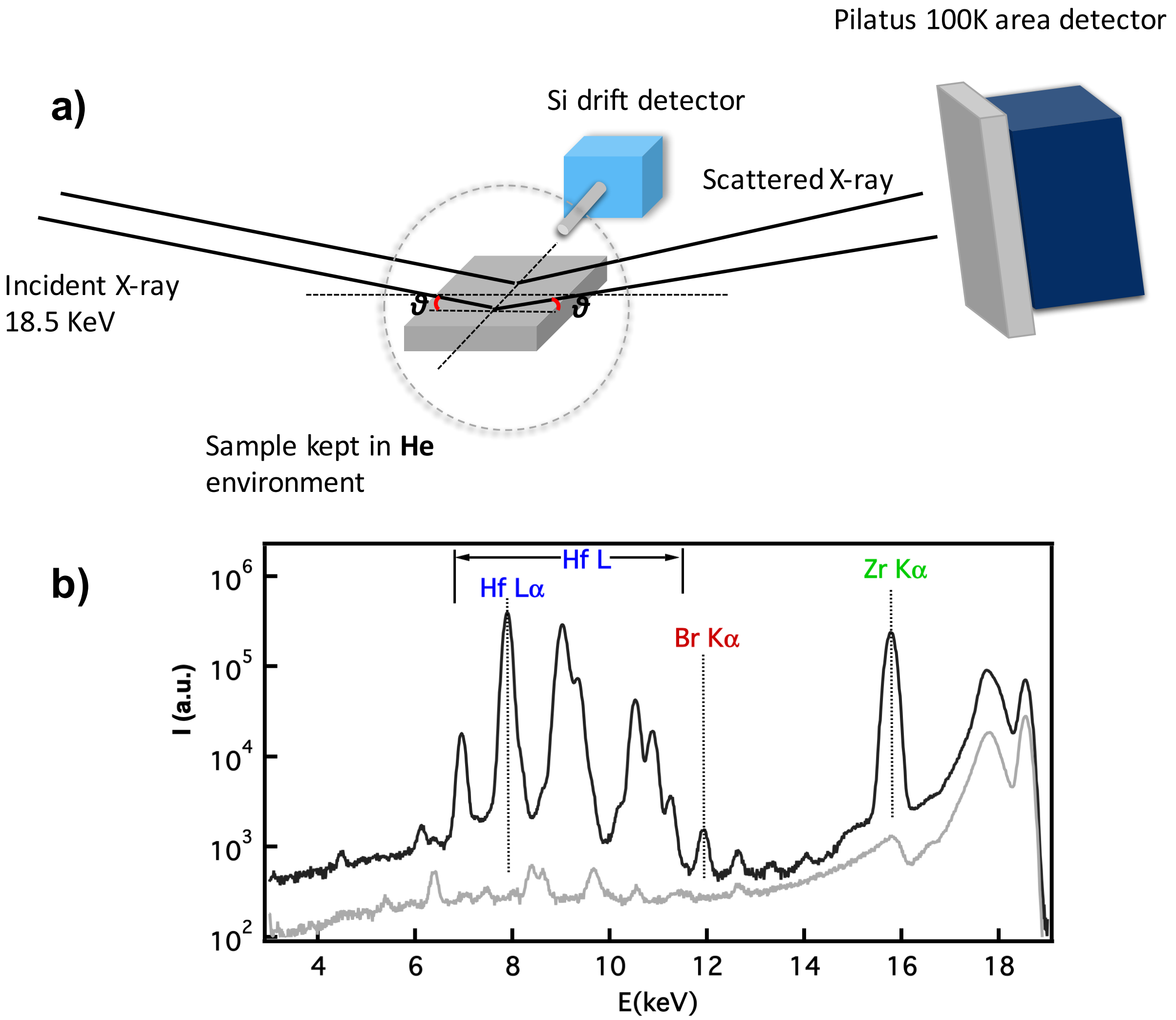

Figure 4.4: (a) Schematic of LP-XSW measurement setup. (b) A representative XRF spectrum of SAND on Si/Mo multilayer collected at $\theta = 0.25°$. The Hf Lα fluorescence peaks (blue), Br Kα fluorescence (red) and Zr Kα fluorescence (green) are highlighted. The gray line is

a XRF spectrum from a blank Si/Mo multilayer substrate at θ = 0.25° with the same experimental condition to ensure that the Hf, Br and Zr peaks were originating from the SAND film.

4.4: XRR Results

The X-ray reflectivity data of the SAND or I-SAND trilayers on Si substrates are presented in Figure 4.5. The derived electron density profiles[93] are used as the initial input for the XSW fitting model of each trilayer type on the Si/Mo multilayer substrates. This trilayer/Si/Mo XRR analysis used Parratt's recursion formulation[68] with an in-house developed least-squares fitting MATLAB program.[60]

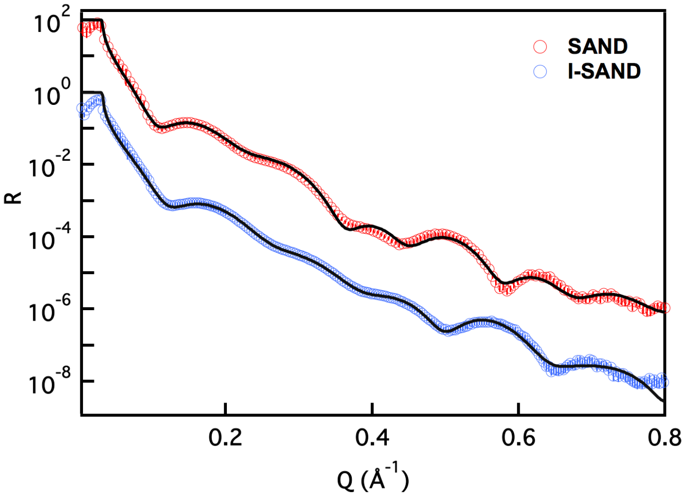

Figure 4.5: X-ray reflectivity of trilayer SAND and I-SAND deposited on Si substrate. The black solid lines are the best-fit results. The SAND data and curve are vertically offset by x100 for purposes of clarity.

4.5: XRF Results

The absolute areal atomic density of three heavy elements are calculated from XRF and listed in Table 4.1, indicating the overall similarity between SAND and I-SAND. The areal electron densities of HfO_x and ZrO_x layer from both XRF and XRR measurements of SAND/ISAND on Si are in a good agreement.

Table 4.1: The areal electron density of for Hf, Br and Zr. The first three columns are XRF-derived elemental coverages.

	Hf (nm^{-2})	Br (nm^{-2})	Zr (nm^{-2})	$HfO_2{}^a$ (e/Å^2)	$ZrO_2{}^a$ (e/Å^2)	$HfO_2{}^b$ (e/Å^2)	$ZrO_2{}^b$ (e/Å^2)
PAE	33.2	0.17	57.7	29.2	32.3	26.7	33.0
IPAE	30.9	0.18	54.7	27.2	30.6	26.2	30.4

a. Areal electron density calculated from XRF-derived elemental coverage. This is based on assuming the HfO_x and ZrO_x layers have the HfO_2 and ZrO_2 stoichiometry.

b. Areal electron density calculated from XRR-derived electron density profile. This is done by multiplying the electron density to the thickness of the layer.

An inert gas environment is recommended for synchrotron X-ray measurements of organic materials to avoid photochemically induced radiation damage. Without the inert environment, the beam damages are observed from measuring the Br fluorescence signals (Figure 4.6) from the same spot on the sample. While with the consistent flowing of He gas, the beam damages are minimized (Figure 4.7).

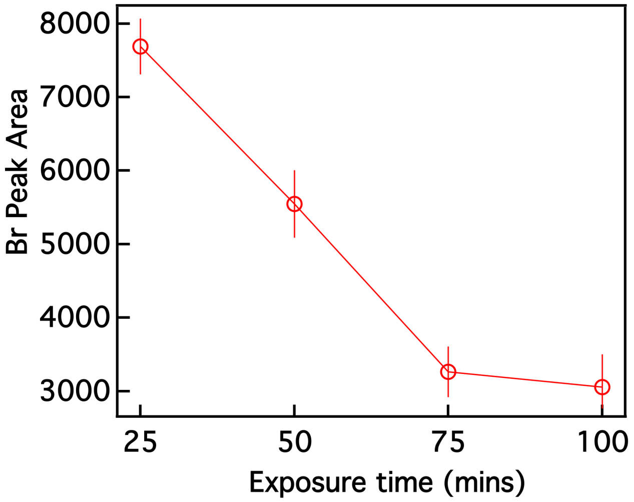

Figure 4.6: Radiation-induced Br desorption in air. The net area under the Br fluorescence signals from 4 consecutive coverage measurements on tri-layer SAND (HfO_x/PAE/ZrO_x) on Si substrate. For each measurement, the sample is illuminated by 0.05 mm (high) × 2 mm (wide), 18.5 keV X-ray beam for 25 mins with an incident photon flux of $\sim 10^{10}$ p/s at an incident angle of 0.6° corresponding to a surface intensity of 1.04×10^9 p/s/mm^2.

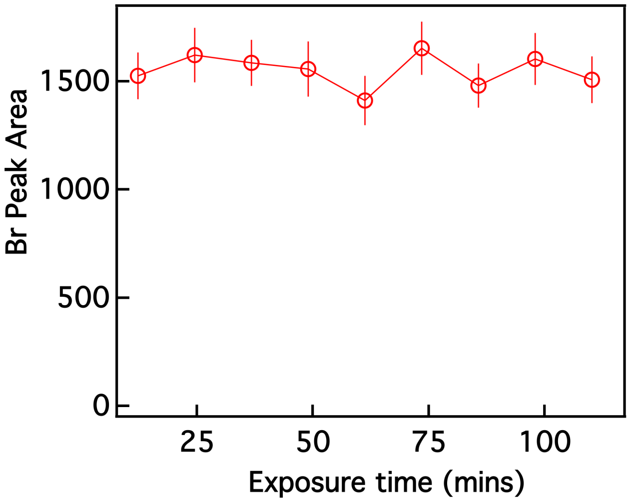

Figure 4.7: Radiation-induced Br desorption in He environment. The net area under the Br fluorescence signals are plotted as a function of exposure time. Each data point corresponds to a 12.25 mins exposure time, and the area is calculated by summing the first 10 points of each saveset for every 5 consecutive savesets of one XSW experiment. The sample is illuminated by 0.05 mm (high) × 2 mm (wide), 18.5 keV X-ray beam with an incident photon flux of ~10^{10} p/s at an incident angle of 0.08° corresponding to a surface intensity of 1.4×10^8 p/s/mm^2.

4.6: XSW Results

The Br^- counteranion layer mean height $\langle z\rangle$ and height difference Δz in the SAND and I-SAND trilayer films were determined by X-ray standing wave (XSW) measurements (Figure 3).[59, 60, 62, 63]

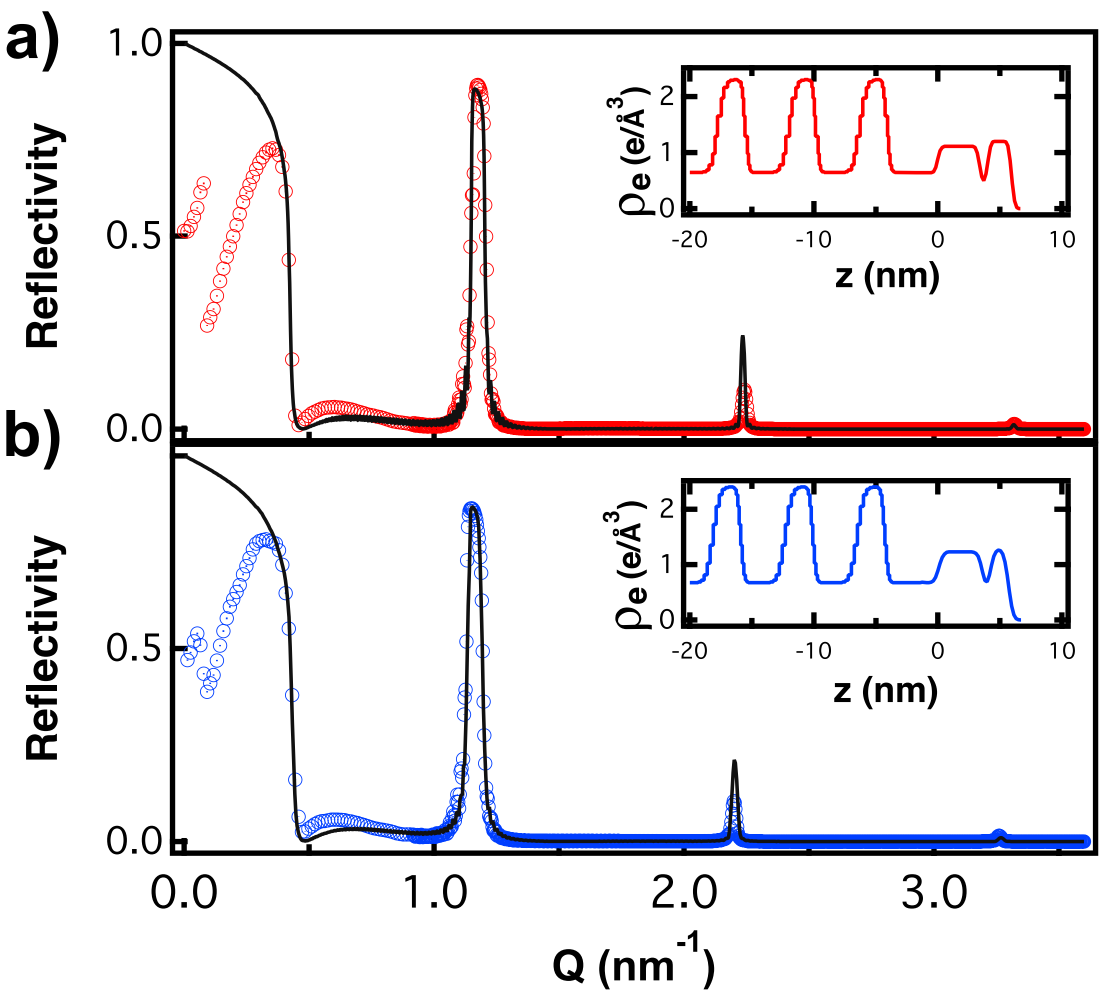

Figure 4.8: X-ray reflectivity data (open circles) and fits (solid black line) for the (a) HfO_x / PAE / ZrO_x and (b) HfO_x / IPAE / ZrO_x trilayers deposited on the SiO_x top-layers of Si/Mo periodic multilayers. The insets show the respective top several layers of electron density profile determined from the XRR fits with z-axis origin chosen to be located at the SiO_x/ZrO_x interface.

The XRR data for both SAND (red circles) and I-SAND (blue circles) on Si/Mo multilayers are presented in Figure 4.8. The reflectivity is plotted as a function of scattering vector magnitude *Q* and compared to a model fit. Intensities for the first three Bragg peaks (1st to 3rd orders) at *Q* = 1.17, 2.24 and 3.33 nm^{-1} are measured to accurately calculate the multilayer period. The 1st order Bragg peak has a high reflected intensity of R_{max} = 85%, indicating well-ordered periodic multilayers with sharp interfaces. The black solid lines are the best-fit results between Q = 0.4 and 3.5 nm^{-1}. The deviation of data from the theory in the low-Q region (Q < 0.4 nm^{-1}) is due to the beam footprint over-extending the length of the sample. The insets in Figure 4.8 show XRR-determined electron density ρ_e profiles for SAND and I-SANDs on Si/Mo multilayers, where z = 0 nm corresponds to the surface of SiO_x layer. The profile region from z = 0 to 6 nm corresponds to the trilayer SAND or I-SAND, which are derived from XRR measurement of their counterparts on the Si substrates. The alternating low and high e-density regions below z = 0 match closely to the expected bulk values for SiO_2, Si and Mo of 0.70, 0.71 and 2.56 e/Å^3, respectively.

The XSW analysis is conducted in the Q-region for total external reflection (TER) (0th order Bragg peak) and the 1st order Bragg peak. The 2nd and 3rd order reflections are omitted because of their low reflectivity. These normalized fluorescence yields for the Hf Lα, Br Kα, and Zr Kα from both the SAND and I-SAND samples are plotted in Figure 4.9. Qualitatively, each elemental normalized yield exhibits a strong, characteristic XSW-stimulated modulation across the 1st order Bragg peak indicating distinct distributions for each atomic species with a width on the scale of half the standing wave period: $\pi/Q_1 \sim 2.73$ nm. Note that, from Eqs. 1 and 2, a completely random distribution would show a modulation that simply follows $1 + R(Q)$, where the reflectivity $R(Q)$ can be seen in Figure 4.8. The distinctive asymmetric shapes observable in Figure 4.9 indicate that each of the atomic distribution profiles, as projected onto the z-axis from an ensemble-averaged 8-mm^2 X-ray footprint, is confined to a well-defined nm-scale distribution within the dielectric film. While the Zr XSW modulations for both SAND and I-SAND are qualitatively similar, the Hf and Br modulations differ substantially between the conventional and inverted structures.

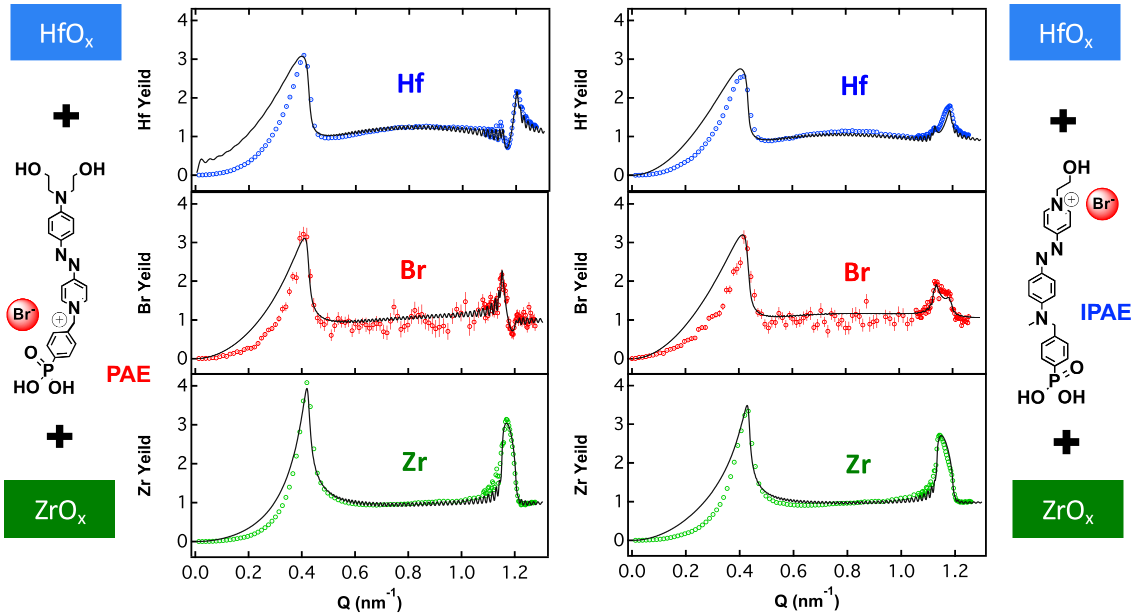

Figure 4.9: XSW induced normalized XRF yields of Hf (blue), Br (red) and Zr (green) (from the top to bottom) for both HfO$_x$ / PAE / ZrO$_x$ (left) and HfO$_x$ / IPAE / ZrO$_x$ (right) trilayer SAND/ISAND on Si/Mo multilayer substrates. These data were collected simultaneously with the reflectivity data shown in Figure 4.8.

Quantitative analysis of the XSW data allows us to determine the atomic distributions $\rho_{\mathrm{Hf}}(\mathrm{z})$, $\rho_{\mathrm{Br}}(\mathrm{z})$, and $\rho_{\mathrm{Zr}}(\mathrm{z})$ and create an elementally sensitive thin film profile. We model both ρ_{Hf} and ρ_{Br} as Gaussian distributions with two fitting parameters: mean positions z_M and widths σ_M. For the thicker ZrO$_x$ layer, ρ_{Zr} is modeled with a rectangular function convoluted with a Gaussian, with free parameters for the thickness t_{Zr} and the interfacial width σ_{Zr}. Each distribution also includes an extended uniform distribution $\rho_{\mathrm{E}_M}(z)$ to account for the atoms that are not contained within the modeled distributions. The range is set from z = 0 to 10 nm to account for a minority-disordered fraction of atoms that are randomly distributed within the film. The final model distribution is therefore $\rho(z) = \mathrm{C}\rho_{\mathrm{M}}(z) + (1-\mathrm{C})\rho_{\mathrm{E_M}}(z)$, where C is the ordered fraction and $\rho_{\mathrm{M}}(\mathrm{z})$ is the distribution profile for M = Hf, Br, or Zr. From the above model for each element and the calculated E-field intensities, $I(Q,z)$, the best-fit results of normalized fluorescence yields are generated and plotted in Figure 4.9 with solid black lines. The TER region has a continually decreasing XSW period from infinity to $2\pi/Q_c$ ~ 14 nm, which helps constrain the dimensions of the thick ZrO_x primer layer.[63] As for the other two elemental distributions, the first Bragg peak is the primary sensitive fitting range.

Table 4.2: Model parameters obtained from fitting the XSW results in Figure 4.9.

	t_{Zr} (nm)	σ_{Zr} (nm)	z_{Br} (nm)	σ_{Br} (nm)	z_{Hf} (nm)	σ_{Hf} (nm)
PAE	3.20	0.40	4.26	0.62	5.34	0.62
IPAE	3.65	0.59	4.66	1.35	5.27	1.16

The XSW model fit determined atomic distributions with z= 0 at the SiO_x/ZrO_x interface are shown in Figure 4.10a. The three elements show up in the expected sequence within each trilayer. The vertical green dash line marks the top surface of ZrO_x layer, and the red and blue dash lines mark the peak positions for the Br and Hf atomic distributions for both the SAND and I-SAND cases. The Hf and Zr results yield reasonable fits indicating the accuracy of this XSW measurement. The best-fit results are summarized in Table 4.2. when replacing PAE with IPAE in the trilayer SANDs, the Br peak position shifts outward by 0.2 nm from the top ZrO_x surface and also the Br peak moves 0.5 nm closer to the HfO_x peak. A slightly wider elemental distribution of I-SAND compared to SAND is observed. This may be partially due to the extracted elemental distributions are averaged across the mm^2 area that is illuminated by incident X-ray beam. The geometry effects and inhomogeneity across the film from solution-processing method can affect nm-scale measurement. However, the peak position remains valid since it shows the most probable location.

4.7: DFT Simulation

Density functional theory (DFT) computations were employed to find the most probable structures of PAE and IPAE by minimizing the total energy E of each molecule[94, 95]. Since Br^- position is subjected to the molecular orientation and tilting, a Boltzmann probability distribution $P_B = e^{\left[-\frac{E-E_{min}}{k_B T}\right]}$ is defined to evaluate the chances of other molecular configurations, where E_{min} is the total energy of the optimized structure, k_B is the Boltzmann constant and T is set at 300 K. The degree of molecular tilting is characterized by z_{N^+}, which is defined as the distance between the +1 quaternized nitrogen in the pyridine group and the bottom plane formed by the three oxygen atoms of PAE or IPAE molecule shown in Figure 4.10c and 4.10d. By manually tilting the molecule with different z_{N^+} values, the Boltzmann probability $P_B = e^{\left[-\frac{E(z_{N^+})-E_{min}}{k_B T}\right]}$ is calculated from the total energy $E(z_{N^+})$ variation. The probability distribution is analyzed by fitting to a Gaussian function to extract the full width at half maximum (FWHM). Additional computational details are referred to SI. Since Br^- is expected to locate near to the quaternized nitrogen, the probability distributions are also used to compare the Br^- distributions in PAE and IPAE.

4.8: Discussion

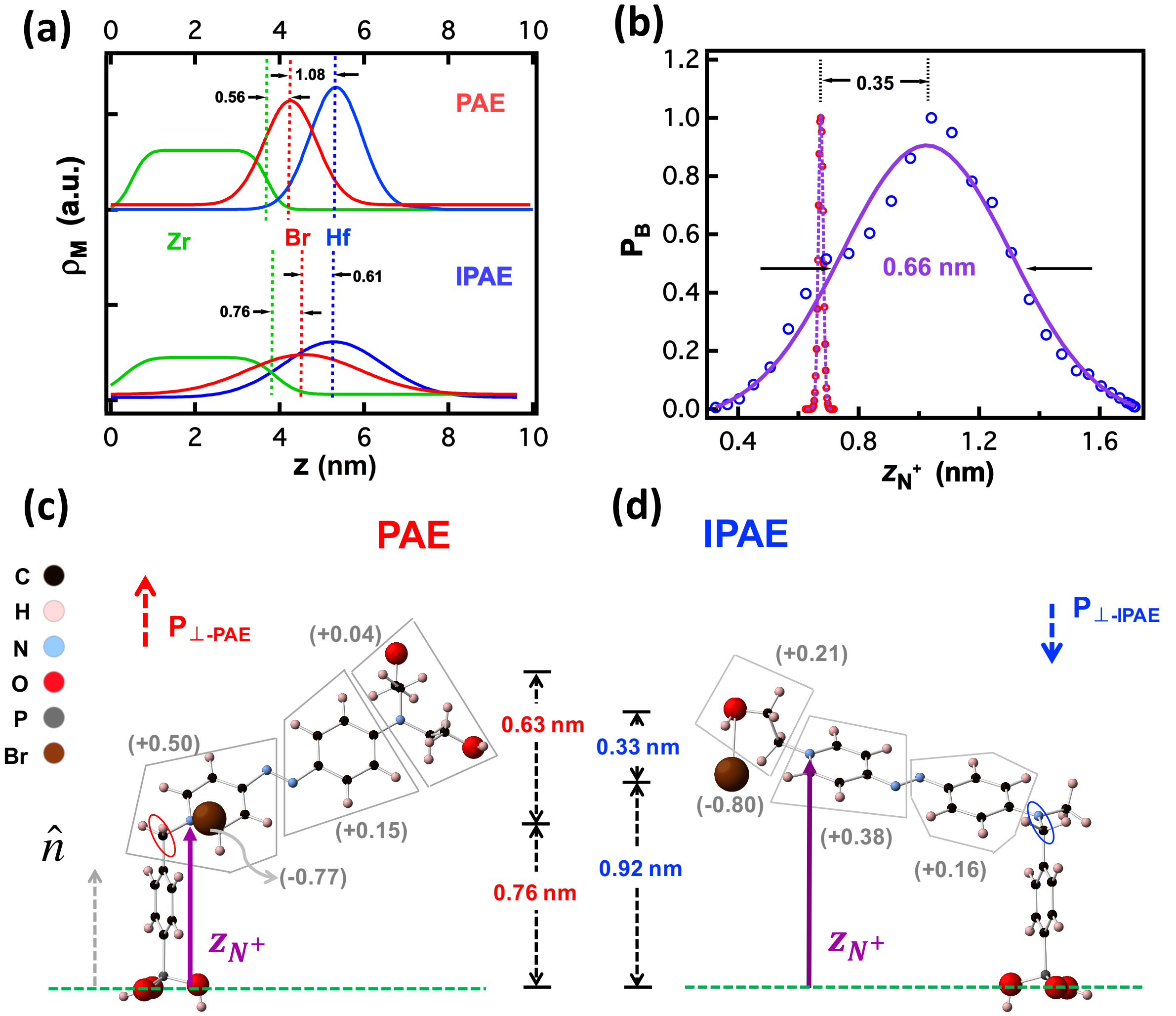

Figure 4.10: (a) The XSW-determined elemental distribution profiles for Zr (green line), Br (red line) and Hf (blue line) for both HfO_x / PAE / ZrO_x (upper) and HfO_x /IPAE / ZrO_x (down) trilayer SAND on Si/Mo multilayer substrates. (b) The DFT-calculated Boltzmann probability distribution P_B of for PAE (red circle) and IPAE (blue circle). Their Gaussian-fit results are plotted with purple dash line (PAE) and solid line (IPAE). The DFT-optimized molecular structures of PAE (c) and IPAE (d). The height of quaternized nitrogen (N^+) $\mathbf{z_{N^+}}$ is defined by

the purple arrow. Green dash lines represent the planes formed by the three oxygens at each phosphoric acid end. Net charges from Mulliken analysis are labeled for each moiety selected with grey solid lines. The bottom unselected parts of PAE and IPAE have net charges close to 0.

Complementary DFT simulations explore the molecular configurations of PAE and IPAE, and provide additional insights to the measured elemental distribution profiles. The optimized structures are shown in Figure 4.10c and 4.10d. Assuming the ZrO_x top surface is terminated with the plane formed by three oxygens of the phosphoric ends (green dash lines in Figure 4.10c and 4.10d)), the long molecular axes of both molecules are significantly tilted versus the surface normal direction ($\hat{n}$). The simulations predict the two molecular heights on the oxide surface are ~1.39 nm for PAE and ~1.25 nm for IPAE. This result agrees well with the XRR measurements with the organic layer thickness being 1.15 nm for PAE and 1.0 nm for IPAE. The smaller height of IPAE vs PAE is also in consistent with XSW measurement: shorter distance, 1.37 (= 0.61 + 0.76) nm, between the peak position of ρ_{Hf} to the ZrO_x surface in IPAE, compared to 1.64 (= 0.56 + 1.08) nm in PAE. DFT also predicts the optimum position of Br^- in IPAE is higher than that in PAE (0.92 nm vs. 0.76 nm), and closer to the bottom of the capping HfO_x layer (0.33 vs 0.66 nm). This is in accord with the XSW-derived Br peak positions, and the relative distances to the oxide layers shown in Figure 10a.

The Br elemental distribution in the IPAE molecule has a wider width than that in PAE (Table 4.2). Possible contributions may refer to the DFT-computed probability distribution P_B and Mulliken charge analysis. The Br^- is considered to locate next to the quaternized nitrogen (N^+) atom of the pyridinium ring for PAE or IPAE shown in Figure 4.3 or Figure 4.10c and

4.10d). Therefore, the distribution of Br^- is influenced by the long molecular axe tilting from normal direction. This effect is expected to be more profound in the IPAE molecule since its pyridine group and Br^- are at the upper end of the molecule. For IPAE molecule, the part highlighted by blue circle in Figure 4.10d, consists of one nitrogen atom and one carbon atom. The sp^3-hybridized bonds of these two adjacent atoms allow the freedom of rotation, which leads to the variation of N^+ height $z_{N^+}$and subsequently the Br^- position. P_B, shown in Figure 4.10b indicates the motion of N^+ has ~0.66 nm vertical height distribution. Similarly, the z_{N^+} distribution for PAE molecule yields a much narrower width (~ 0.02 nm). This is due to the relatively rigid sp^3 bond angle of the carbon atom, highlighted in the black circle (Figure 4.10c). Hence, an additional ~0.65 nm difference leads Br^- to have a broader distribution in IPAE than in PAE.

Another reason why Br^- has a broader distribution within I-SAND may be elucidated by the Mulliken charge analysis presented in Figure 4.10c and 4.10d, which probes the majority positive charges of the cations of both molecules. Indicated by the net charge distribution, the cation in PAE has a more localized positive charge compared to that in IPAE. Therefore, Br^- counteranion attached to PAE distributes more locally around the N^+ due to the strong electrical attraction force, and a narrower Br distribution should be observed. Hence, the DFT simulation results are in a reasonable agreement with XSW experiment regarding the molecular configuration and heavy anion distributions.

The diploe moments of PAE and IPAE are also computed from the Mulliken charge analysis. The projected magnitude along the surface normal direction $P_\perp$ are 3.04 and -0.70 D for the optimized PAE and IPAE structures, respectively. The negative sign indicates the inversion of dipole direction as shown by the arrows in Figure 4.10c and 4.10d. Experimental results show that when replacing PAE with IPAE molecular layer in SAND-based device, an additional negative shift in threshold voltage ΔV_T was observed.[81] This is in consistent with the following relationship, $\Delta V_T \sim NP_{\perp}/\varepsilon_0 k$. Hence, through this study, the designs and control of the dipole inversion, characterized by XSW measurements and DFT simulations, and demonstrated with OTFTs device performances, provide more flexibility in operating more complex circuits.

4.9: Summary of Dipole Inversion Determined by X-ray Measurements

A direct comparison of counteranion distributions within two self-assembled nano-dielectrics (SANDs) has been characterized and systematically studied by X-ray technique (XRR, XRF, and XSW) and complementary DFT simulation. The two SANDs share the same trilayer structures: a self-assembled high-k molecular layer of inverting dipole, and each sandwiched between a capping HfO_x layer and a bottom ZrO_x layer. The organic layer spacing from X-ray measurement is in a good agreement with DFT-optimized molecular height, indicating both molecules are tilted with respect the surface normal direction. The Br^- counteranions of PAE molecules were found to locate closer to the bottom ZrO_x layer and have a narrower distribution compared to that in IPAE. This result is in a good agreement with DFT simulations of the degree of molecular tilting, and with the results of Mulliken charge analysis. The experimental and computational results revealed how PAE and IPAE self-assemble and orient within SAND and I-SAND, and correlated the dipole inversion to the controlled voltage shifts when using IPAE as a polarizable layer in devices.

4.10: *In situ* XSW Measurement of SAND under an Externally Applied Electric Field

The study of Br^- displacement under an applied E-field would help us better correlate the dipole moment of the high-*k* molecular layer to SAND-based devices, and explain why SAND has such a high capacitance and its overall performance. The successful measurement of the dipole inversion within SAND and I-SAND (as discussed in Section 4.8) demonstrates the potentials to quantify the Br^- displacement induced by applying an external electrical field by using XSW technique.

The *in situ* experiment adopts the tri-layer SAND structure, and the bottom Si/Mo synthetic multilayer structure for the generation of XSW. The multilayers are sputter-deposited onto a conductive Si substrate. A highly conductive single-layer graphene is transferred onto the tri-layer SAND as the top electrode. X-ray-transparent graphene should be an ideal electrode for this experiment. A schematic drawing and photographic image of the experimental sample structure are shown in Figure 4.11 and Figure 4.12, respectively.

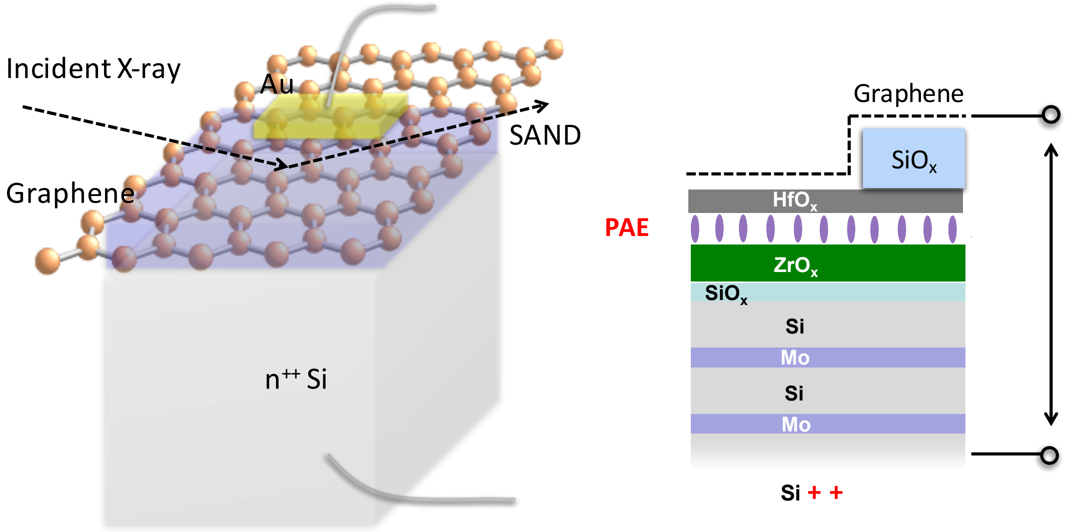

Figure 4.11: Schematic design for the *in situ* XSW measurement of HfO_x/PAE/ZrO_x using graphene as the top contact. The voltage is applied across the top graphene electrode and the bottom highly conductive Si substrate.

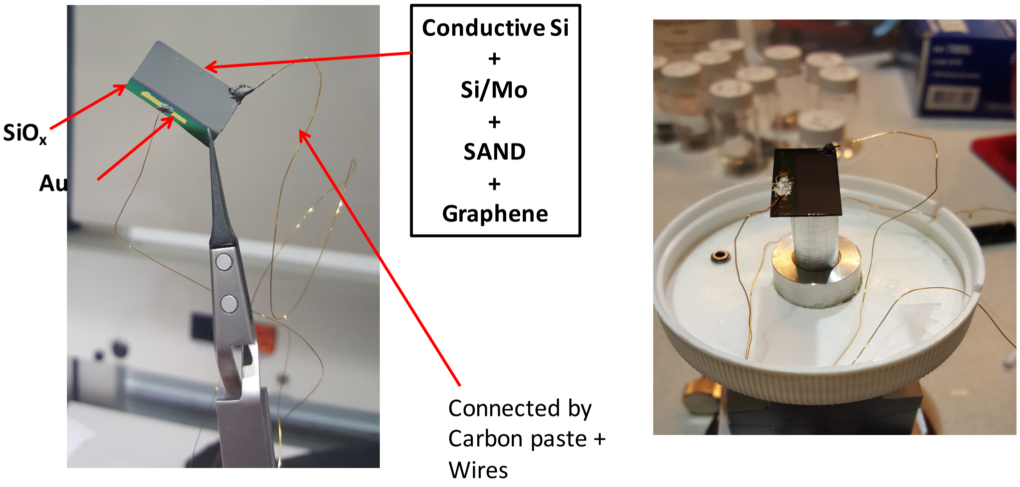

Figure 4.12: Photographic images of the sample (left) and the amounting stage (right) for *in situ* XSW experiment at sector 33BMC at APS. In addition to Figure 4.11 (left), a sputtered SiO_2 layer (100 nm) is deposited on the trilayer SAND before transferring the graphene, to prevent the device from shorting. The Au electrode (50 nm) is thermally evaporated onto the selective area of the top graphene layer to ensure a good electrical contact with the extended Cu wire.

The X-ray reflectivity is firstly employed to exam the structure of tri-layer SAND with top graphene layer (Figure 4.13). From the XRR results, the thickness of the graphene layer is about 2 nm. The bottom ZrO_x layer remains unchanged while the HfO_x has a slightly increased electron density and reduced thickness. This is due to the post-annealing treatment during the graphene deposition process.

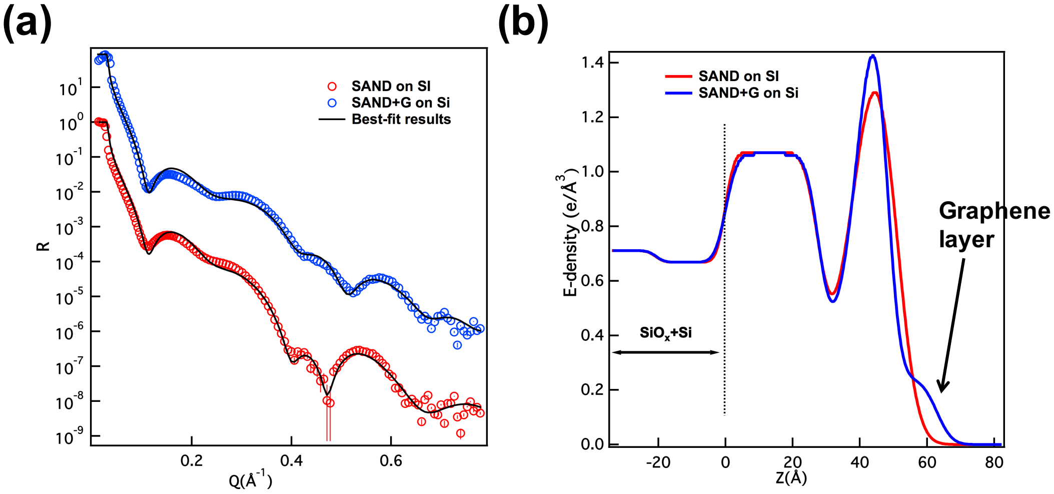

Figure 4.13: (a) X-ray reflectivity data of graphene-coated tri-layer SAND and pure SAND deposited on the Si substrates (blue circles). From the comparison between the two corresponding electron density profiles (b), the thickness of graphene layer is about 2 nm.

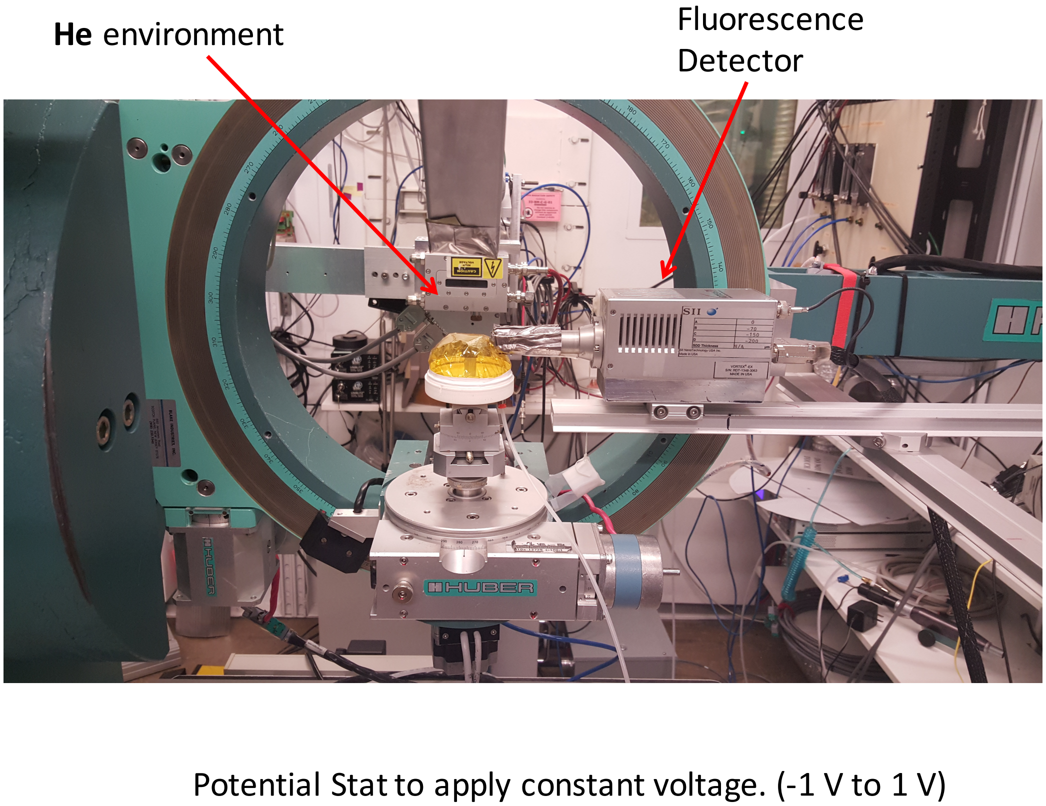

Figure 4.14: The *in situ* XSW experiment setup at sector 33BMC at APS. A potential stat is used to apply and hold the external voltage. Sample is kept in He environment during the entire measurement.

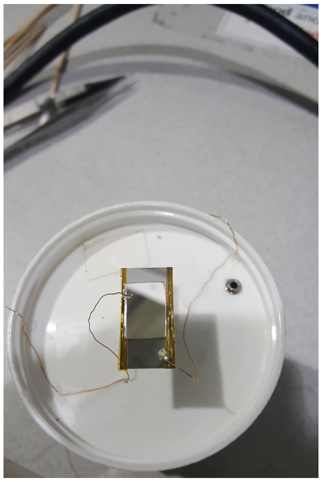

Figure 4.15: A photographic sample image. The differences compared to the design in Figure 4.12 are 30 nm thermally evaporated Al instead of graphene as the top contact and thin Kapton tapes replacing the sputter-deposited SiO_2 layer.

The *in situ* X-ray standing wave experimental setup is shown in Figure 4.14, which is very similar to the pervious XSW setup (Figure 4.4a). The preliminary results are shown in Figure 4.16. As marked by the red dash lines, the relative distances between the peak positions of the fluorescence yield and reflectivity data don’t show significant changes after applying a 1 V external voltage.

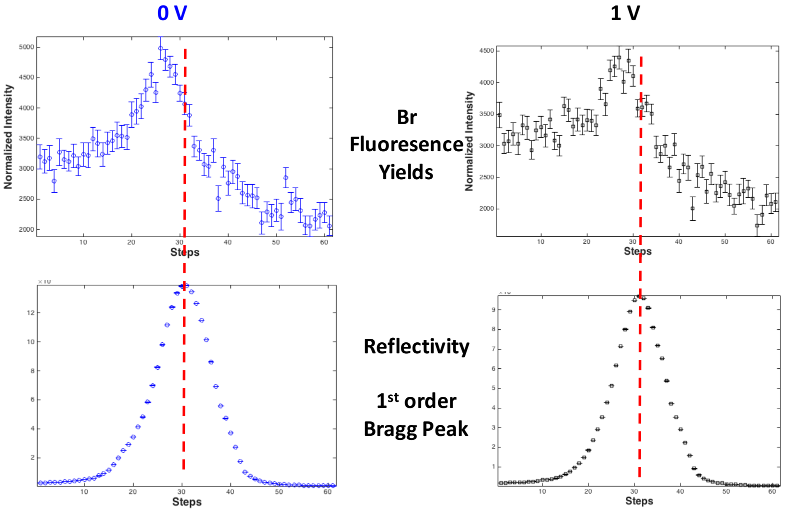

Figure 4.16: The preliminary results of Br fluorescence and the reflectivity data. No significant changes are observed after 1V is applied to our sample.

The simultaneously recorded current vs time curves (*I*-*t*) are listed in Figure 4.17 for four different external voltages. The low current flowing through the sample at 1 V or -1 V (Figure 4.17(a) and (b)) indicates a good insulting property. The current level (~10^{-5} A) is also sufficiently higher than the open-circuit current (~10^{-9} A), which indicates a good electrical contact. When the applied voltage is equal or higher than 2 V, the SANDs break down to generate a much higher current (~10^{3} A). Therefore, 1 V or -1V is recommended for the *in situ* XSW measurement.

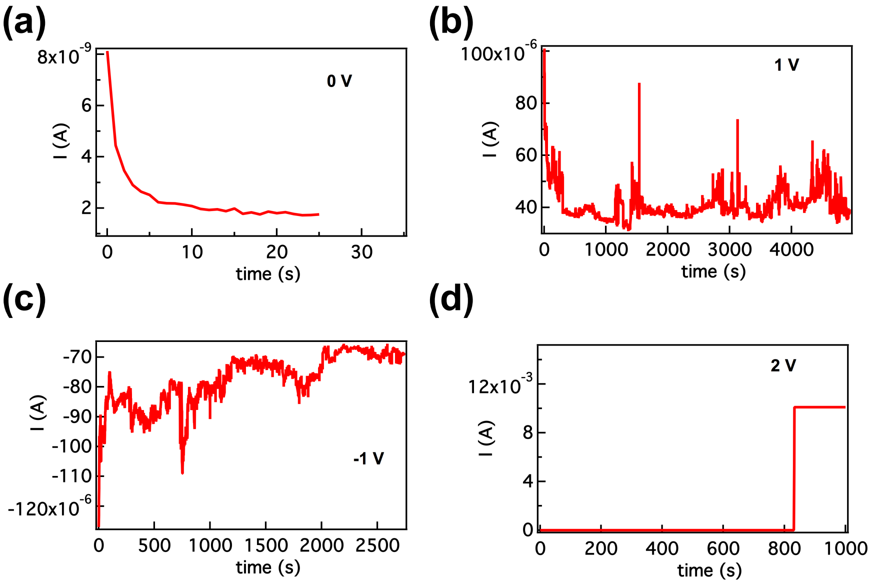

Figure 4.17: The *I-t* curves for sample under (a) 0 V (open circuit), (b) 1 V, (c) -1 V and (d) 2 V. At both 1 and -1 V, the current flows through the sample is at a very low level (~10^{-5} A), while at 2 V, after ~13 mins, the sample breaks down, which results in a much higher current (~10^{-3} A).

Discussions and Suggestions:

From the *in situ* XSW measurements, no significant changes are observed for the Br fluorescence signals at different applied voltages. Possible reasons and suggestions are listed as follows:

1. The applied voltage is not high enough. From the results of electrical measurement, the tri-layer SAND cannot stand voltage ≥ 2V for longer than 13 mins. This is not sufficient for building up statistics in XSW experiment. One way to increase the robustness of SANDs is to use the high-quality oxide films synthesized by ALD or PLD, instead of the solution-processed films. The physical vapor deposited oxide layers should have a better insulating property, which

has been discussed in section 2.4.3.

The other alternative is to increase the Br^- coverage so a good signal-to-noise ratio can be achieved before the device breaks down. More detailed discussion related to Br^- coverage is in the following section 4.11.1. Also, switching Br^- by a lower Z halogen, such as Cl^-, probably can increase the coverage of halogen in SAND due to a stronger electrical bonding.

2. A theoretical estimation is needed regarding whether Br^- will move or how much Br^- will move. From the DFT simulation results, it is possible that the displacement of Br^- is very small as shown in Figure 4.18. Assuming there is an electrical field with direction indicated by the black arrow, the negative charged Br^- along with the tilted long upper part of PAE molecule (positive-charged cation) will rotate so Br^- will reach a possible stable position (gray dash circle). However, in this case, the Br^- displacement is very limited, and likely to be smeared out by its thermal motion. Note that this rotation will result in a flipping of the dipole since the Br^- probably moves from below the cation to above.

In the TFT, the E-field (Figure 2.1) has an opposite direction compared to the one shown in Figure 4.18. In that case, the Br^- should move downwards. However, due to the strong electrical attraction between Br^- and cation, this is less likely to happen (Figure 4.10c).

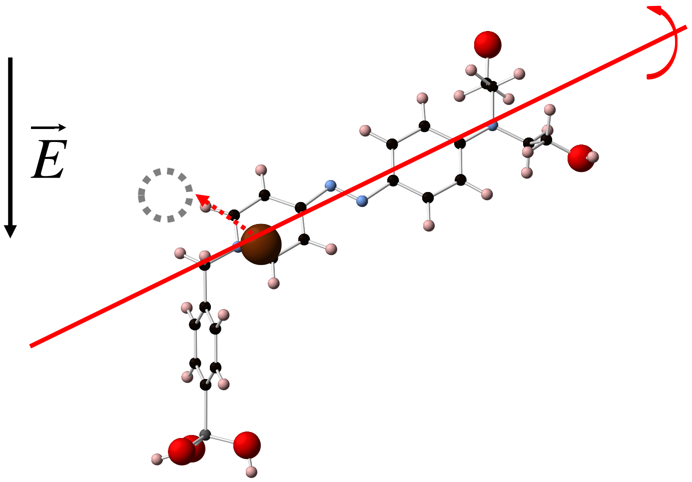

Figure 4.18: A schematic to show a possible Br motion under E-field.

Compared to PAE, using IPAE molecule for *in situ* XSW experiment may have a better chance to observe the Br$^-$ displacement since Br$^-$ is less localized (Figure 4.10d) and the freedom to rotation of the upper part may provide additional motion to Br$^-$.

4.11: Outlook and the Design criteria for High-*k* Molecular Layer

4.11.1: Molecular coverage derived from X-ray reflectivity

The molecular coverage and footprint of PAE molecule can be calculated from the XRR-determined electron density of the organic layer in SAND. Figures 4.19 and 4.20 show the XRR data and the corresponding e-density profile of the uncapped Hf-SAND film on Si substrate. To eliminate the effects from the spin-coated capping layer, the film consists of only two layers: the self-assembled PAE layer and the bottom prime HfO$_x$ layer.

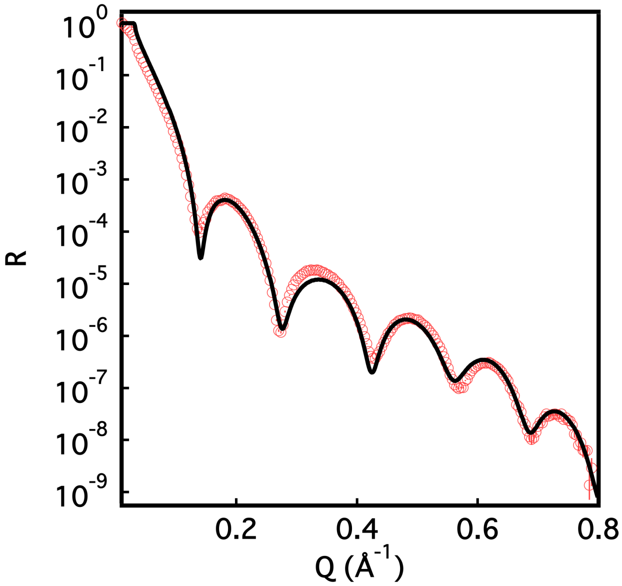

Figure 4.19: X-ray reflectivity data of PAE/HfO_x deposited on Si substrate.

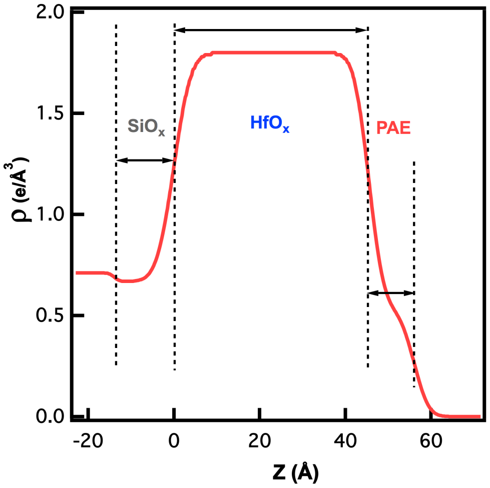

Figure 4.20: XRR-derived electron density profile of PAE/HfO_x deposited on Si substrate.

From the fitting result, the thickness of PAE layer is 1.06 nm and the electron density is 0.51 (e/Å^3). The coverage for PAE molecule Γ, chemical formula ($C_{22}N_4O_5PH_{26}Br$), can be calculated as:

$$\Gamma = \frac{0.51\times10.6}{(6\times22+4\times7+5\times8+15+26+35)} = 1.96\ (/\mathrm{nm}^2)\ ,$$

which corresponds to a 0.5 nm^2 footprint.

This result deviates from the previous XRF-determined Br coverage. Assuming one Br is associated with a PAE molecule, the molecular coverage should be the same as the Br coverage, which is 0.2 /nm^2. So, there are about 10 times difference in the results derived from these two approaches. A possible explanation is: during the self-assembled process, when the phosphoric end of PAE bonds to the hydroxyl group on the ZrO_x surface, a proton (H^+) is generated and takes away the Br^- from PAE by forming the gas-phase HBr. Therefore, it would necessary to use other methods to determine and confirm the molecular coverage, such as cyclic voltammetry (CV)[86, 96], and to improve our understandings to the self-assembly process of PAE molecule.

4.11.2: Limitations of DFT-Optimized Molecular Structures

The DFT-optimized structures of both PAE and IPAE molecules are obtained by assuming little intermolecular interactions. This is achieved by setting the simulation box of each molecule to be sufficiently large (30×30×30 $Å^3$). So, even though a 3D periodic boundary condition is used, the simulated system is treated as a dilute case. The reason why we end up using this approach instead of including the more realistic intermolecular interactions lies on the limitations of DFT theory. It is known as the “self-interaction error”. The DFT tends to delocalize the electron density and has challenges when dealing with the ionic molecules, such as PAE. Applying DFT simulation directly to the PAE molecule sometimes leads to the nonphysical simulation results, such as a covalent bond is formed between Br and the N in the pyridine group, or the Br is positively charged. The electronic structure of Br (35 electrons) is also quite complicated for the DFT simulations.

Hence, to address this problem, we first optimize only the cation structure without Br^- and the neighboring interactions. To balance the positively charged cation, a neutralizing negative charge background with uniformly distribution in the simulation box is introduced. This first part including the Boltzmann distribution (section 4.7) is calculated by using VASP simulation package. The later Mulliken charge analysis (section 4.7) is done by using the NWChem software.

Even though this approach focuses on the case of an isolated molecular structure, it is interesting to note that the DFT-calculated molecular heights, which do not include the neighboring molecular interactions, agree with the XRR-determined thickness of the organic layer thickness (section 4.8). And the study of single molecule case will certainly provide insights to the understanding of the molecular configuration, and anion motions.

More effective simulation approach is still under development, such as varying the size and shape of the simulation box. Eventually, we would like to better correlate the electrical properties and structural characterization of SAM to the DFT-predicted information.

4.11.3: Future Design Criteria for High-*k* Molecular Layer

The future design criteria for the high-*k* molecular layer are: high dipole moment along the normal direction or the applied field direction, high/dense molecular packing coverage, and defect-free ultrathin layer.

Many molecules, such as PAE and IPAE can have very high dipole moments. However, the effective dipole moments, which is along the surface normal direction, are much less pronounced. Therefore, synthesizing a molecule with a large dipole moment while managing to stand up and align with the neighboring ones would be the most important criteria. A highly-packed SAM layer can be more effective compared to that made of randomly orientated molecules, which also leads to the formation of the high-quality thin layer.

Chapter 5 : Amorphous to Crystalline Transition of In_2O_3 Films

5.1: Introduction

Transparent conducting oxides (TCO) and transparent oxide semiconductors (TOS) are candidate component materials for the next-generation of thin film transistors (TFTs) due to their excellent optical transparency, electrical mobility, and mechanical flexibility.[2, 30, 97, 98] Recently, a preference for amorphous TCO and TOS (a-TCO/TOS) over their crystalline counterparts has emerged due to the following advantages.[11, 29, 99] Because of the lack of grain boundaries, a-TCO and a-TOS thin films possess higher film uniformity, smoother surfaces, and enhanced mechanical flexibility. The lower deposition temperatures ($T_d < 250$ °C) for a-TCO/TOS enables fabrication on flexible substrates, such as plastics.[100-102] Another advantage is the ability to maintain a relatively high mobility (≥ 10 $cm^2V^{-1}s^{-1}$) while the structure is amorphous. Note that this is the opposite effect seen for the case of amorphous silicon (a-Si:H), where the mobility is ~2 orders of magnitude lower than crystalline Si. The mobility of a-TCO/TOS is relatively insensitive to the structural disordering because the large non-directional *n*s orbitals ($n \geq 4$) of transition metal ions provide dispersive electron conduction paths.[26] Therefore, a-TCO/TOS present a great potential and are attracting much attentions for applications in TFT fabrication.

Typically, a-TCO/TOS are In_2O_3 based amorphous metal oxides (AMOs) with the introduction of metal ion dopants such as (Zn, Sn, Ga, Y, La, etc.)[10, 32, 103], or organic species[104, 105]. Amorphous indium-gallium-zinc oxide (a-IGZO) is one of the most widely used AMOs with its industrial applications as a semiconductor layer in TFTs.[26, 31, 106] Much research has been conducted to synthesize AMOs with various methods, such as sputtering, pulsed layer deposition (PLD) and solution-processing[10]; to tune and optimize the electrical properties from either growth conditions or post-growth-treatments[107]; to study the structural-property relations theoretically and experimentally[7, 108-110]. In contrast, there are much fewer reported studies into the thermal properties of AMOs.[48, 111-115] Temperature is a critical parameter in thin-film processing that allows for the fine-tuning of structure and properties. For example, when lowering substrate deposition temperature ($T_d < 0$ °C), various techniques such as DC magnetron sputtering and PLD can grow a-TCO/TOS.[33, 34] Therefore, an improved understanding of a-TCO/TOS when subjected to thermal treatments, would be of great importance in terms of the cost, processing and applications of these materials.

To exclude the effects and ambiguity brought by dopants, this paper will concentrate on pure In_2O_3 since it is the key matrix material for a-TCO/TOS. In our prior research, a series of PLD-synthesized In_2O_3 thin films were made with substrate temperature T_d varying from -100 to 600 °C; as T_d increased the degree of crystallinity increased in these as-deposited films.[33] Our earlier detailed *ab initio* molecular dynamics simulation and X-ray absorption fine structure (XAFS) study of the as-deposited In_2O_3 films also indicated structural difference in the amorphous phase, such as local nanocrystalline inclusions (~3 nm), and InO_x polyhedral preferences and distributions.[34] These differences buried in the amorphous material could potentially alter the energy barriers for initializing crystallization and affect the overall crystallization kinetics. Herein, we designed and conducted a thermal stability study to compare the crystallization process for PLD grown amorphous In_2O_3 films deposited at different values of T_d.

5.2: Sample Preparation

In_2O_3 films with 300 nm thicknesses were grown on 10 x 10 x 0.4 mm^3 Si substrates by pulsed laser deposition (PLD) method (descripted in Chapter 2.4.3). A 248 nm KrF excimer laser with 25 ns pulse duration and operated at 2 Hz and a dense hot-pressed In_2O_3 target (25 mm diameter) were used for the PLD process. The 200 mJ/pulse beam was focused onto a 1 mm × 3 mm spot size. The target was rotated at 5 rpm about its axis to prevent localized heating. The target-substrate separation was fixed at 10 cm. The films were grown on silicon substrates in an O_2 ambient of 8 mTorr. The substrates were attached to the substrate holder with silver paint. Three sets of films were grown under three deposition temperature (T_d): -50 °C, -25 °C, and 0 °C controlled by using liquid nitrogen.[34]

5.3: In situ GIWAXS Experiment at 5BMC

In situ GIWAXS was employed to study the isothermal crystallization process of In_2O_3 films deposited at different T_d. The experiment (Figure 3.1) was performed at sector 5BMC of DuPont-Northwestern-Dow Collaboration Assess Team (DND-CAT) at Advanced Photon Source (APS). A monochromic 20.00 keV X-ray beam with 20 μm by 400 μm incidence beam size and ~10^7 photons/s flux was used. The incidence angle was fixed at α = 0.17° (α_c = 0.14° for In_2O_3 of electron density ρ = 1.6 e/$Å^3$) with ~200 nm penetration depth to ensure that only the film would be probed by the incident X-ray beam. The samples were annealed under vacuum condition (~ 2×10^{-4} mBar) controlled in a mini-chamber with a beryllium-dome, mounted on the diffractometer, with a pyrolytic boron nitride-coated pyrolytic graphite (PBN/PG) heating stage. The sample temperature was monitored with a thermal couple in contact with the film surface. For a set of In_2O_3 films deposited at the same T_d, each was annealed isothermally at a fixed annealing temperatures T_A. For example, the three films deposited at T_d = -25°C were annealed at 180°C, 190°C, and 200°C, respectively. In total, nine crystallization transitions were measured and studied to estimate the effects of initial growth conditions and summarized in Table 1. A Mar165CCD (2048 by 2048 pixels; pixel size 79 μm) area detector was placed ~180 mm away from the sample to collect a 100 s exposure-time GIWAXS diffraction pattern in 120 s time intervals. The 2D area detector was calibrated by XRD from a lanthanum hexaboride (LaB_6) standard powder sample. An X-ray shutter-closed, dark image was recorded for background subtraction.

5.4: Images Reduction and Crystallinity calculation

The Nika package was used for 2D image data reduction.[116] The beam center position, sample to detector distance L, and detector tilting angles were refined from the calibration of LaB_6 standard. These refined parameters were then input to convert experimental 2D images into q space ($q = 4\pi \sin\theta/\lambda$ is the momentum transfer). A 1D profile ($I(q)$ *vs.* q) was generated by circularly averaging the diffraction rings on the 2D images, which is later used for the degree of crystallinity calculation. Equation (3.7) underestimates the crystalline fraction because $I_c(q)$ does not include diffuse scattering due to thermal induced atomic vibrations and lattice imperfection. Hence, a Therefore, a lattice imperfection factor D was proposed to compensate this effect and approximated by a Gaussian function:

$$D = e^{-kq^2}, \tag{5.1}$$

in which k is a coefficient evaluating the disorder of sample. Therefore, the degree of crystallinity can be redefined as:

$$\chi_c = \frac{\int_0^\infty q^2 I_c(q)dq}{\int_0^\infty q^2 I(q)dq}\frac{\int_0^\infty q^2\overline{f^2}dq}{\int_0^\infty q^2\overline{f^2}Ddq}, \tag{5.2}$$

in which $\overline{f^2} = \sum N_i f_i^2/\sum N_i$ is the mean-square atomic scattering factor, and the f_i is the atomic scattering factor of type i atom with N_i number in the stoichiometric formula.[117, 118] Since the degree of crystallinity χ_c should be independent of q range ($q_0 \sim q_f$) used for calculation in eq. S3, by tuning the value of k and the range of q, the accurate degree of crystallinity χ_c for each set of T_d and T_A will be extracted. In all the cases, we chose q_0=1 Å^{-1} as the start calculation range and varied the end range $q_f \leq 4$ Å^{-1} to assess the k parameter in Eq.(S1).

$$\chi_c = \frac{\int_{q_0}^{q_f} q^2 I_c(q)dq}{\int_{q_0}^{q_f} q^2 I(q)dq}\frac{\int_{q_0}^{q_f} q^2\overline{f^2}dq}{\int_{q_0}^{q_f} q^2\overline{f^2}Ddq} = \text{constant} \tag{5.3}$$

The thermally induced structural evolvement was monitored by GIWAXS. Indium oxide has bixbyite structure (space group Ia$\overline{3}$, ICSD #169420, Figure 2.6) with a = 10.117 Å. A simulated 1D diffraciton pattern is included in Figure 5.1 (lower). A time-sequence of 1D diffraction patterns from an In_2O_3 film that was deposited at T_d = -25°C and held at T_A = 180°C is presented in Figure 5.2. For the first ~2 h the patterns exhibit two broad amorphous scattering peaks, after which In_2O_3 diffraction peaks grow in time with the reduction of the amorphous peaks. After ~12 h the amorphous to crystalline transitions approaches completion and sharp diffraction peaks indicate the formation of large crystalline domains. Using the Ruland's methods (Eq. 5.3), the degree of crystallinity $\chi_c(t)$ as a function of annealing time t is extracted from the data Figure 5.3a. This crystallization process curve demonstrates the typical "S" shape with three regions:

the beginning region is related to a long incubation time for initial nuclei to precipitate and overcome the activation energy; followed by a middle region with a steep slope where fast crystallization and crystallites growth occur; and finally, as the crystalline grains expand and meet at the grain boundaries, the film slowly approaches full crystallinity. Similar analysis was carried out to generate crystallization curves for each T_d, T_A combination.

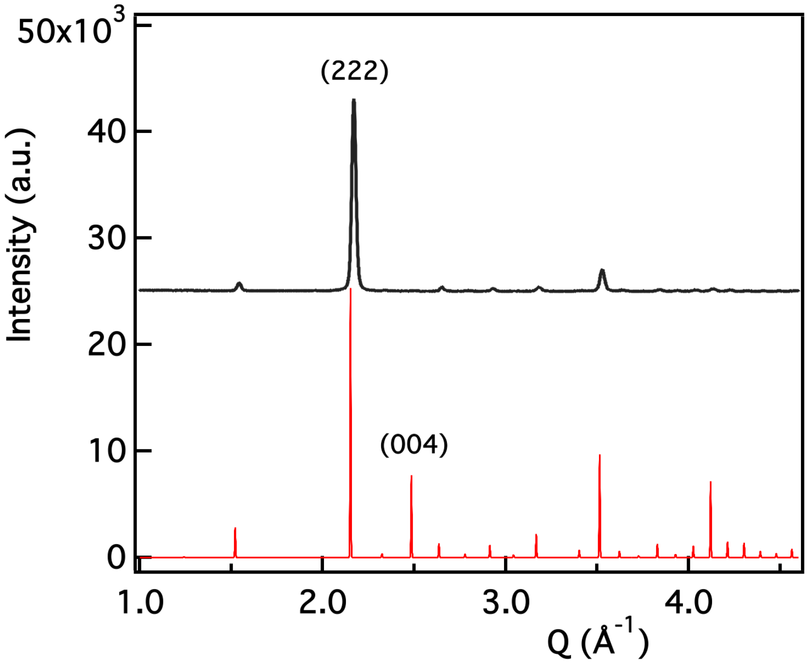

Figure 5.1: GIXRD of In_2O_3 thin film deposited at T_d= 400 °C. Rigaku ATX-G 1D pattern collected at fixed incident angle of $\alpha = 0.5°$ and variable out of plane exit angle β (upper). And the simulated powder X-ray diffraction pattern of In_2O_3 from CrystalMaker (ICSD #:169420) software (lower).

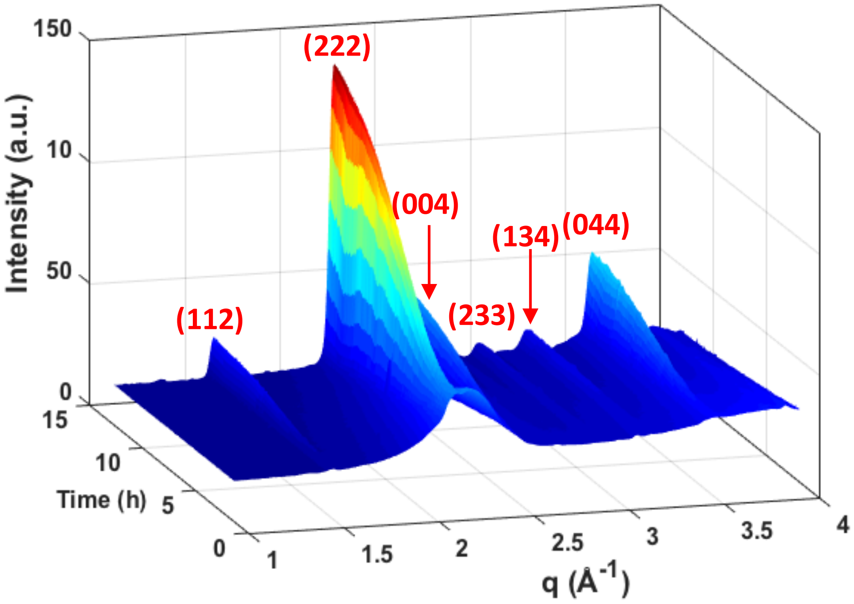

Figure 5.2: Time-sequence of 1D X-ray diffraction patterns from In_2O_3 film (T_d= -25°C, T_A = 180°C). The 0 to 2 h patterns (not shown) are essentially identical to the data at 2 h.

Before introducing a quantitative model-dependent simulation to interpret the evolvement of the degree of crystallinity, a simple approximation of the crystallization time τ_C is computed by the time difference between the film reaching 10% and 90% crystallinity as shown in Figure 5.3a. The extracted crystallization times for all nine samples are plotted in Figure 5.3b. For films deposited at the same T_d, lowering the annealing temperature T_A requires a longer annealing time τ_C. Lower T_A leads to a lower grain growth rate and nuclei formation rate, which results in a longer annealing time. Another way to interpret Figure 5.3b is to estimate the required annealing temperature if all films crystalize within the same time. For example, if three films deposited at T_d = 0, -25, and -50°C are expected to have the same τ_C ~ 4 h, the annealing temperature T_A would be ~ 135°C, 180°C and ~ 220°C, respectively. There is ~40°C increase in T_A as T_d decreases by 25°C. Therefore, even though as-deposited films are amorphous, there are intrinsic structural differences resulted from the disposition temperature T_d, which affect the subsequent crystallization.

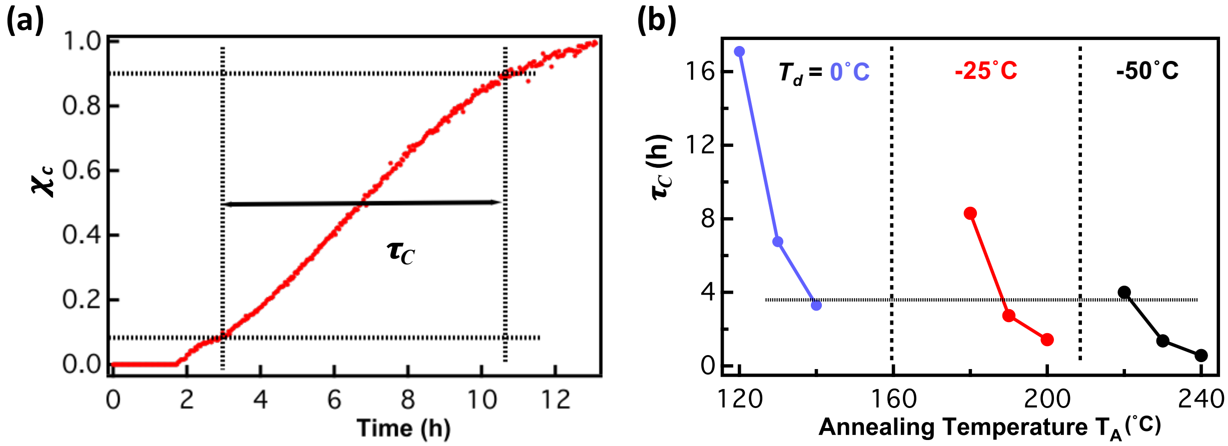

Figure 5.3: (a) Based on Eq. 5.3, experimentally determined degree of crystallinity (χ_c) as function annealing time. This example is for the film deposited at T_d = -25°C and held at T_A = 180°C. All nine crystallization curves are shown in Figure 5.6. Crystallization time τ_c is defined as the time interval between $\boldsymbol{\chi_c = 0.1}$ and $\boldsymbol{\chi_c = 0.9}$. (b) Crystallization time as a function of annealing temperature T_A for the three films deposited at each T_d (0, -25, and -50°C).

5.5: Domain Size Calculation

The domain size D_{hkl} in certain (*hkl*) directions at the final crystalline phase ($\chi_c \rightarrow 1$) is determined by applying Scherrer formula to the peak width Δq ($D_{hkl} = 1.8\pi/\Delta q$).[53] However, the observed width is typically broadened due to the instrumental effects. In our case, the use of very small incident angle (α_i) will result in a large footprint on the sample, and cause a geometrical smearing Δq_{geo} on the area detector, as illustrated in Figure 5.4(b). Therefore, Δq_{geo} needs to be considered and subtracted from Δq_{exp} to derive the sample-specific diffraction width Δq_{cry}:

$$\Delta q_{\mathrm{exp}} = \Delta q_{\mathrm{geo}} \otimes \Delta q_{\mathrm{cry}}\,. \tag{5.4}$$

Δq_{geo} is calculated at the exit angle 2θ:

$$\Delta q_{\mathrm{geo}} = \left(\frac{4\pi}{\lambda}\right)\cos\left(\frac{2\theta}{2}\right)\left(\frac{w\tan 2\theta}{2L}\right), \tag{5.5}$$

in which λ is the wavelength of X-ray, w is the incident beam footprint on the sample ($w \propto 1/\sin\alpha_i$) and L is the sample to detector distance. Our approach is: when increasing the incident angle α, Δq_{geo} is suppressed since the footprint w is reduced. So, assuming Δq_{cry} remains constant for polycrystalline sample despite of the choice of α, Δq_{cry} can be de-convoluted from the experimental result, and extrapolated by increasing incident angle α (= 2°, 3°, 4°, 5° and 6°).

A pseudo-Voigt function is generally used to extract the diffraction width Δq_{exp}. The extracted width satisfies the following general relation with its Gaussian $\Delta q_{\mathrm{exp,G}}$ and Lorentzian $\Delta q_{\mathrm{exp,L}}$ components:

$$\Delta q_{\mathrm{exp}}{}^2 = \Delta q_{\mathrm{exp,L}} \cdot \Delta q_{\mathrm{exp}} + \Delta q_{\mathrm{exp,G}}{}^2. \tag{5.6}$$

Since the de-convolution rule of either Gaussian or Lorentzian component is known, the diffraction width related to the crystalline domain size (Δq_{cry}) in the film can be determined by subtracting geometric effect Δq_{geo} from each component:

$$\Delta q_{\mathrm{cry,L}} = \Delta q_{\mathrm{exp,L}} - \Delta q_{\mathrm{geo,L}} \tag{5.7}$$

$$\Delta q_{\mathrm{cry,G}} = \sqrt{\Delta q_{\mathrm{exp,G}}{}^2 - \Delta q_{\mathrm{geo,G}}{}^2}, \tag{5.8}$$

As pointed out in the reference[119, 120], Δq_{geo} typically has a Gaussian distribution so its Lorentzian component is assumed to be 0. Eq. 5.7 becomes:

$$\Delta q_{cry,L} = \Delta q_{exp,L} \tag{5.9}$$

Once the Gaussian $\Delta q_{cry,G}$ and Lorentzian $\Delta q_{cry,L}$components are derived, the general relation (Eq. 5.6) also applies to Δq_{cry}:

$$\Delta q_{cry}{}^2 = \Delta q_{cry,L} \cdot \Delta q_{cry} + \Delta q_{cry,G}{}^2 \tag{5.10}$$

$$\Delta q_{cry} = \frac{\Delta q_{cry,L} + \sqrt{\Delta q_{cry,L}{}^2 + 4\Delta q_{cry,G}{}^2}}{2}. \tag{5.11}$$

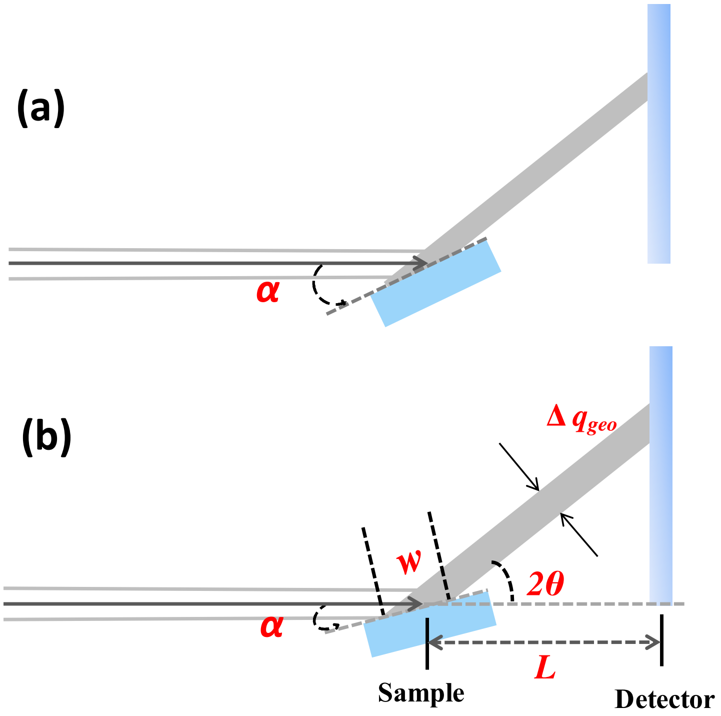

Figure 5.4: Schematics of the geometric broadening effect with 2D detector under grazing incident condition. This effect, as indicated with the width $\mathbf{\Delta q_{geo}}$ from (b) to (a), can be reduced by increasing the incident angle (α).

The domain sizes, D_{hkl}, of the after-annealed crystalline films are extracted from the (222) and (004) diffraction peak widths and presented in Table 5.1. For films deposited at T_d = -25°C and -50°C, $D_{222} \approx D_{004};$ while for the films deposited at T_d = 0°C, the domain sizes along the two directions diverge (D_{004} > 50 nm, D_{222} < 40 nm). This is consistent with the texturing analysis. For the textured film, the initial nanocrystalline inclusions align their (004) lattice planes perpendicular to the surface normal direction, the growth of crystallites along the surface normal direction is less likely to be interrupted by their neighboring ones, and result in a longer length.

Electron microscopy images of the surface and grain morphology of the crystalline film (T_d = 0°C and T_A = 130°C) are shown in Figure 5.5. Note that even though some of the domains in the SEM image showed ~μm size dimension, they are not necessary to be the single crystal domains. Therefore, the domain size derived from X-ray analysis is still valid.

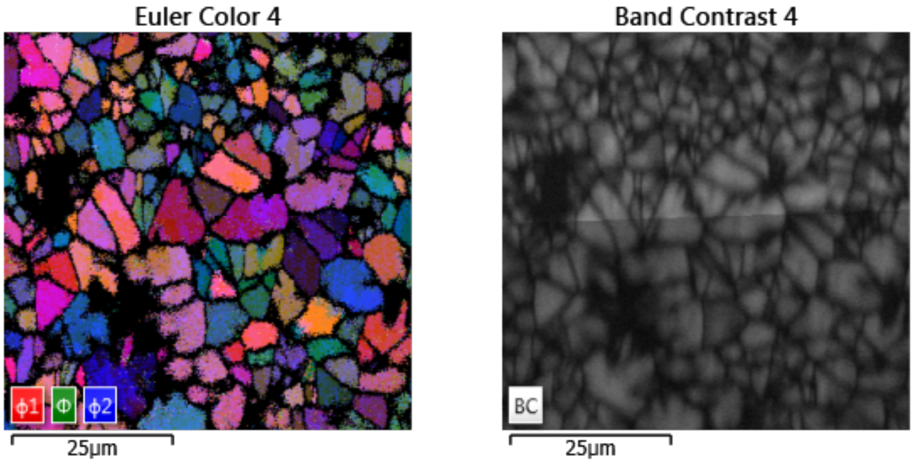

Figure 5.5: EBSD image (left) and SEM image (right) of the after-annealed film (T_d= 0 °C, T_A= 130 °C) show the crystalline domain orientations and size distributions.

Table 5.1: Summary of crystallization time τ_C, Aramid constant *n*, and post-annealed domain size *D*

Sample #	T_d (°C)	T_A (°C)	τ_C *(min)*	*n*	D_{222} (nm)	D_{004} (nm)
1	-50	220	376	2.48	45.9	44.4
2	-50	230	79	3.85	45.7	39.3
3	-50	240	46	3.87	41.1	33.5
4	-25	180	678	2.56	45.2	47.9
5	-25	190	278	2.41	42.8	40.3
6	-25	200	132	2.60	45.5	43.3
7	0	120	1520	2.66	39.9	55.8
8	0	130	496	2.42	38.0	50.5
9	0	140	250	2.52	36.9	53.0

5.6: Texturing Analysis

The time-sequenced collection of the crystalline GIWAXS patterns (Figure 5.6) also provides information about the preferred crystallite orientation, i.e. thin-film texture, from which the crystallite growth directions can be traced. GIWAXS patterns with uniform Bragg diffraction rings correspond to polycrystalline films without preferred orientation. Strong texturing occurred for the three films deposited at the highest temperature of $T_d = 0$°C.

The (001) pole density shown in Figure 5.7a (bottom) of the $T_d = 0$°C, $T_A = 130$°C fully crystalline film was collected at the 2θ for the (004) Bragg condition in reflection geometry (i.e., at $\alpha = \beta = \frac{2\theta}{2}$, where α and β are the incident and scattered directions relative to the surface). The concentrated pole density in the center, at tilt angle $\chi = 0$, indicates that the crystallites have a preferred direction that aligns cubic unit cell axes along the surface normal direction of the film. The outer uniform ring at $\chi = 90°$ corresponds to the other unit cell axial directions lying in-plane with no preferred azimuthal ϕ orientation. Because the (222) Bragg ring lies close to the (004), as seen in Figure 5.2, the collection of the 004 PF also allowed for simultaneous collection of the (222) PF as displayed in Figure 5.7a (top). The uniform azimuthal density of the 222 poles at $\chi = 54.7°$ is consistent with a cubic film having cube texture. This is also confirmed by the PF results from EBSD (Figure 5.7b). An example of non-textured polycrystalline PF from EBSD measurement is shown in Figure 5.8 for comparison. A line-cut profile extracted from the X-ray (004) PF image of Figure 5.7a (bottom) is shown in Figure 5.7c. This quantitatively describes the orientation distribution of the crystallites (004) poles about the surface normal direction as having a width of 23°. This information will be used below in the LSM simulation as pre-defined nuclei-orientation input.

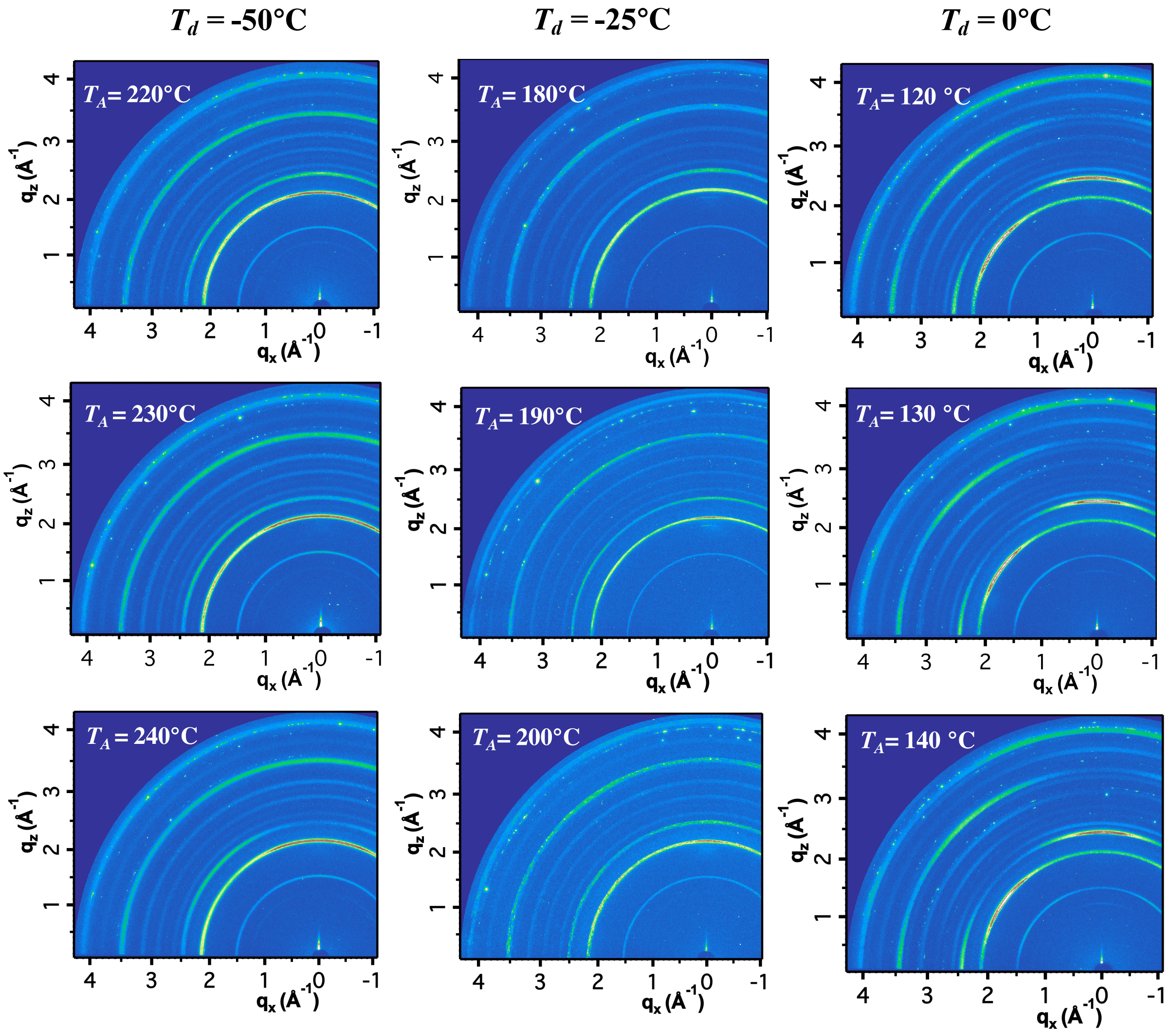

Figure 5.6: Summery of after-annealed crystalline GIWAXS patterns of all nine samples.

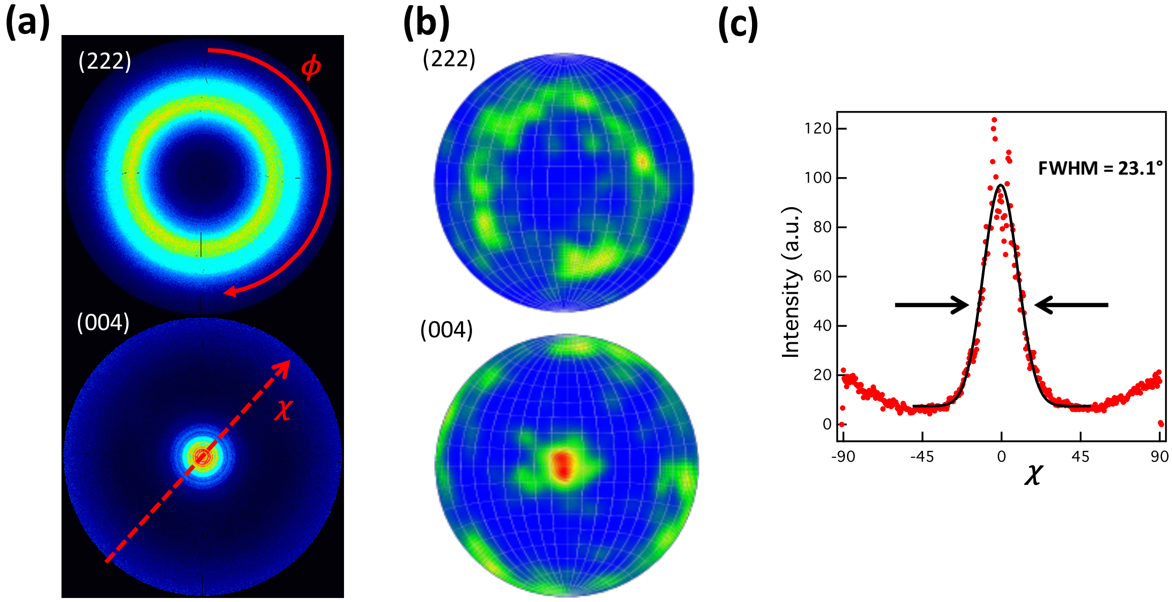

Figure 5.7: PF from both X-ray (a) and EBSD (b) measurements of the crystalline In_2O_3 thin film (T_d = 0°C, T_A = 130°C) at (222) (upper) and (004) (lower) Bragg conditions. (c) The line-cut profile from X-ray PF (a, lower) with its Gaussian fit yielding a FWHM = 23.1°.

This observed texturing suggests that films grown at a sufficiently high temperature (0°C) may have nanocrystalline In_2O_3 inclusions within an amorphous matrix that have cube texture. Whereas, within the amorphous films grown at lower T_d (-25 and -50°C), the nanocrystalline inclusions could be non-textured. Therefore, in addition to the above effects of T_d shown on the crystallization time τ_C, the higher T_d leads to a lower energy barrier for the nanoscale crystallites to align with their preferred orientations.[43]

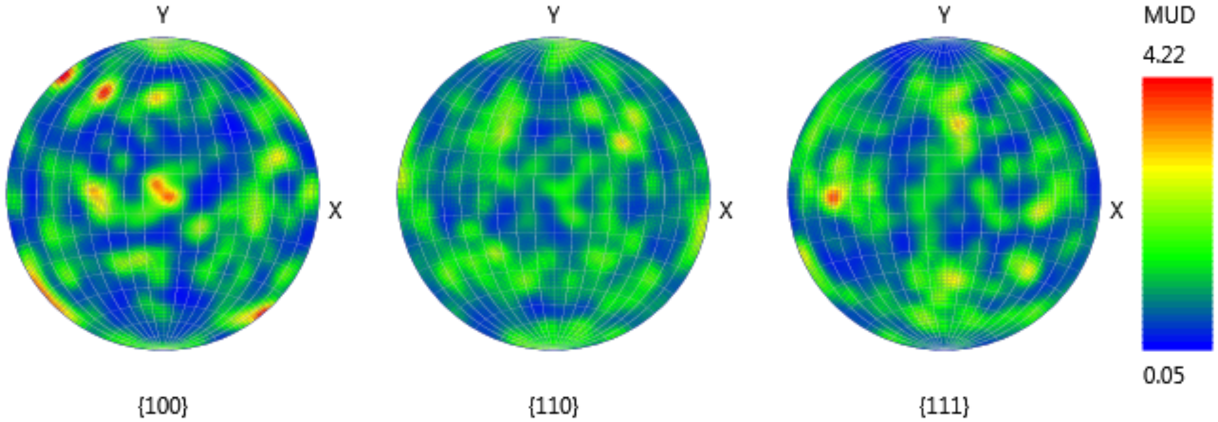

Figure 5.8: Pole figures (a) measured along three major plane normal directions of the after-annealed film (T_d = -25 °C, T_A = 190 °C) indicating the film is non-textured polycrystalline.

Note that even though the (004) is the observed preferred orientation, it does not necessarily mean the crystalline films deposited at higher T_d (> 0°C) will always present the same (004) texture. A grazing incident XRD (GIXRD) pattern of 300 nm In_2O_3 film PLD-deposited on Si substrate at T_d = 400°C is shown in Figure 5.1. It suggests that the film is highly crystalline, and possibly has a 222 texture since the peak intensity ratio $I_{(222)}/I_{(004)}$ is much higher than the simulated ratio for a perfect In_2O_3 powder. Similar results were also observed from previous GIXRD patterns of crystalline In_2O_3 films deposited on quartz substrates.[33, 34] At the same T_d = 400°C, the feature of a (222) texture was shown for 60 nm film, while a (004) texture for 300 nm film.

5.7: Level-set Simulation

The isothermal annealing condition is chosen for this set of experiments, since it allows for one variable: annealing time t. Isothermal crystallization traditionally can be described by the Johnson-Mel-Avrmai-Kolmogorow (JMAK) equation:

$$\chi_c = 1 - e^{-Kt^n}, \tag{5.12}$$

where n is the Avrami exponent, $K = K_0 \exp(-E_a/k_B T_A)$ is a temperature dependent rate constant, E_a is the activation energy, k_B is the Boltzmann constant, and T_A is the annealing temperature, which is held constant.[121, 122] The JMAK equation is generally more accurate in describing the bulk transformation of isotropic growth than the thin film case, but the average value of Avrami exponent n can still be helpful to determine the growth dimensionality (Dim) and understand the nucleation mechanism. For the site saturated nucleation (SSN) case, $n = Dim$, while for the constant nucleate rate (CNR) case, $n = Dim + 1$.[123] A more rigorous approach namely the level-set method (LSM) is also employed in this report. It is a numerical route used to track the time-dependent evolution of shapes and interfaces by providing topology changes of nuclei growth and collisions, which also has the advantages of versatility and flexibility of modeling: initial crystalline fraction, interface velocity, and object dimensions.

Level-set method (LSM) is a strong simulation scheme for describing moving boundary problems and complex topology evolution.[124, 125] The inherent geometrical nature of this method makes it an ideal approach for studying interface-controlled kinetics phenomena like crystallization from amorphous state or relaxation of polarized domain in ferroelectrics.[126] The major distinction of this method from other simulation methodologies is its capability to evolve on experimental length and time scales, which provides unique opportunity for comparing simulation results with experimental measurements directly. In this approach, for a single crystal, the level-set function is defined as a continues signed distance function $\emptyset(x,t)$, where the interface between crystal and amorphous is implicitly described by $\emptyset(x,t) = 0$ then it evolves through the equation of motion as shown in Eq. 5.13, where V is the interface velocity.

$$\frac{\partial \emptyset}{\partial t} + V \cdot \nabla \emptyset = 0 \tag{5.13}$$

Eq. 5.13 is numerically solved using forward Euler time discretization scheme in 3D Cartesian coordination. In isotropic case, V is a scalar parameter, which results in spherical growth with constant rate. In anisotropic case, interface velocity becomes a function of different parameters like curvature, orientation, concentration and temperature. Previous studies on Indium Oxide systems are shown fully faceted cubic crystal growth during crystallization.[49, 127-129] Hence, in this work, we are going to consider the situation where V only depends on orientation. Therefore, the interface evolution is defined as $V = \gamma(n)n$, where n is an interface normal at given point and Eq. 5.14 changes to its new format as follow.

$$\frac{\partial \emptyset}{\partial t} + \gamma(n) \cdot |\nabla \emptyset| = 0 \tag{5.14}$$

To determine $\gamma(n)$, we employ Russo-Smereka's approach[130] for faceted growth, which has been proven to deliver correct Wulff construction for given morphology. In this approach $\gamma(n)$ is defined as shown in Eq. 5.15

$$\gamma(n) = v_F + u\sqrt{1 - (n \cdot n_F)^2} \tag{5.15}$$

Here, $v_F$and u are facet normal and tangential velocity and n_F denotes facet normal direction. Eq. 5.15 matches every single point of the interface to its closest facet based on their normal directions. For instance, in cubic growth, surface normal adapts one of the six directions of cubic facets <100>. Tangential term imposes sharp growth at the edges and ensures fully faceted evolution of the grain. Detailed implementation of Russo-Smereka's approach and its integration into our LSM algorithm for simulation of faceted crystallization is discussed in previous study.[129]

The temporal evolutions of the crystallization process for different film deposition temperature (T_d) at different annealing temperature (T_A) are shown in Figure 5.9. As expected, for each deposition temperature, by increasing annealing temperature, incubation time for starting transformation decreases and system undergoes faster crystallization, which agrees with the qualitative analysis in Figure 5.3b.

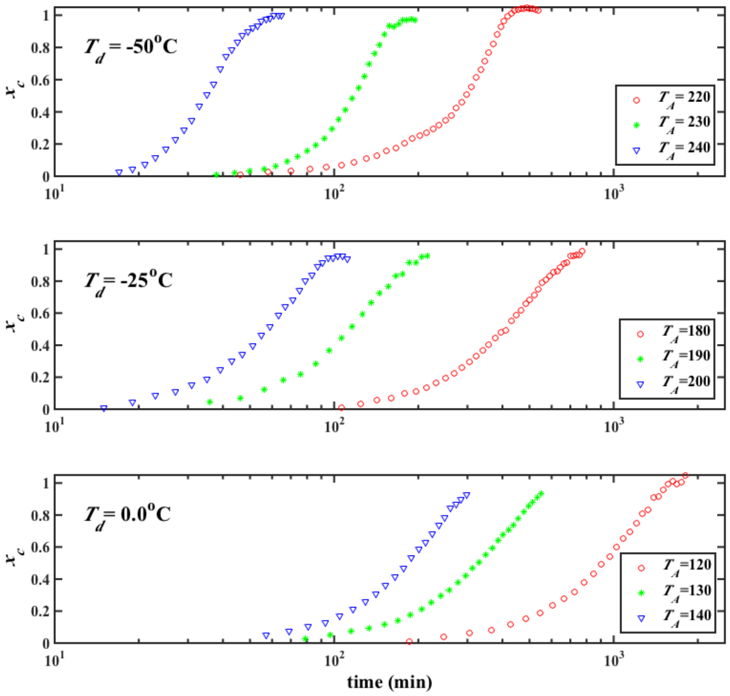

Figure 5.9: The degree of crystallinity evolvement for In_2O_3 films. For film deposited at the same T_d, three annealing temperature (T_A) are explored.

First step to simulate kinetics of crystallization via level-set method is to identify nucleation mechanism in crystallization process, which can be done by calculating Avrami exponent (n) from crystallinity (χ_c) vs. time *(t)* data. The determination of Avrami exponent (n) starts with the re-arrangement of eq. 12 as follows:

$$\ln[1/(1-\chi_c)] = \ln(k) + n\ln(t) \tag{5.16}$$

From Eq. 5.16, the slope of the linear region shows the average value for Avrami exponent (n). Avrami exponent for all samples has been summarized in Table 5.1 along with domain size information and crystallization time (τ_c). Even though the governing assumption of JMAK equation (bulk transformation with free isotropic growth) is inaccurate in thin film crystallization, previous studies show that the average value of Avrami exponent n still can be referred as a most probable possibility for nucleation mechanism.[129]

Avrami exponent results (Table 5.1) suggest that except sample 2 and 3, all other samples deposited are most likely undergone crystallization through Site-Saturated Nucleation (SSN). Taking that into account, sample 8 (T_d = 0°C; T_A = 130°C) is chosen for more detailed kinetics simulation via LSM method due to additional texture information extracted from the PF measurement.

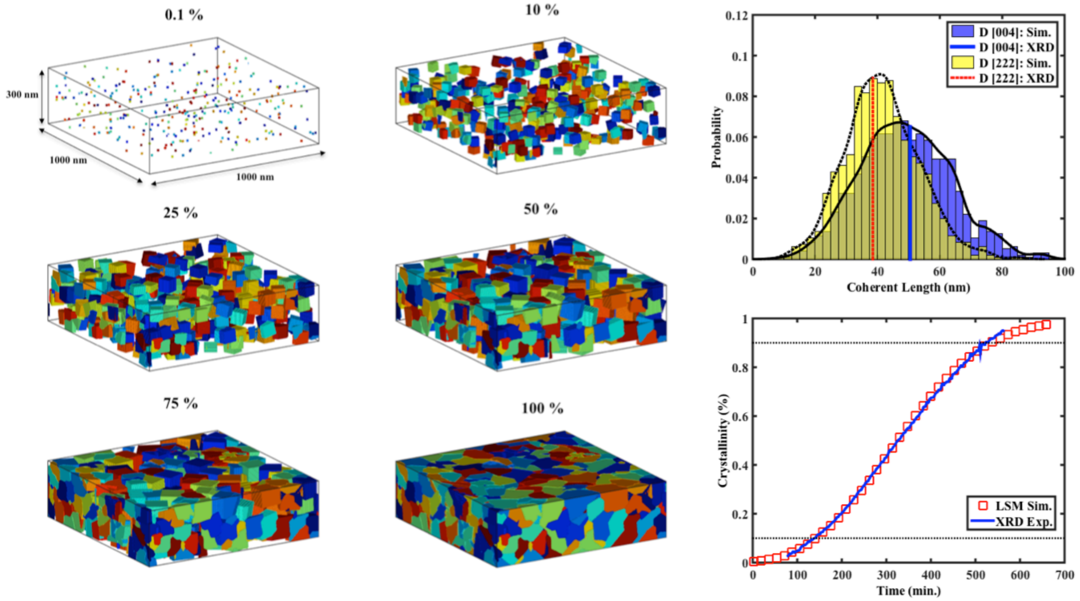

Figure 5.10: Simulation results (a) visualization of crystallization process modeled by the level-set method for site-saturated nucleation and cubic growth. The transformed volume has been shown. (b) Probability distribution of domain sizes along (004) and (222) plane directions. (c) Experimental and simulated crystallinity vs. time plot, used to extract the interface velocity.

In simulation box, XY plane is setup as $1000\times1000\,nm$ and Z direction fixed as $300\,nm$. Periodic boundary conditions are imposed only on film lateral sides (both X and Y directions) to avoid size effects. The Z direction is along the film normal with box size equals to the average film thickness. Furthermore, to acquire statistically enough microstructure data, all simulation results are averaged over 20 runs with different initial configurations of the nuclei. Since the nucleation mechanism for sample 8 is identified as site-saturated case, simulation starts with fixed number of nuclei at the beginning of the crystallization. Orientation of each nucleus is assigned based on χ and ϕ angles (Figure 5.11), to resemble texture structure observed in Figure 5.7c. The tilting angle (χ) with respect to (004) is drawn from Gaussian distribution (FWHM= $23.1°$) and rotating angle (ϕ) around (004) is randomly assigned between $0°$ and $360°$. By changing the nucleation density (N_V) as a fitting parameter, it is found that $N_V = 1.066\times10^{-6}\,nm^{-3}$ generates the closest microstructure to the sample 8 case. Figure 5.10b shows simulation results for probability distribution density of the domain size D along (004) and (222) plane normal direction. The comparative results for domain sizes from X-ray diffraction (XRD) measurement and LSM simulation are summarized in Table 5.2.

Having a reasonable prediction of the microstructure in hand, one can match a dimensionless time unit in simulation with according to the τ_c in the experiment to determine

$\{001\}$ interface facet velocity (v_F), which for sample 8, it results in $v_F = 0.11\ (nm/\text{min})$. To determine interface velocity films with the same T_d but annealed at other, similar simulations are performed on sample 7 & 9 with the same texturing assumption. The results are calculated as 0.04 and $0.21\ (nm/\text{min})$ respectively. These temperature dependence values are then used to determine activation energy of growth via Arrhenius relation. The activation energy is found to be -0.5 eV, which only includes growth process. Table 5.1 data reveals that there is no significant change in domain size for samples deposited at $T_d = 0^{\circ}$C, which indicates relatively similar nucleation densities at different annealing temperatures. This is consistence with the formation of nanocrystalline inclusions during the film deposition, confirms SSN mechanism. Formation of nanocrystalline particles can be seen at lower deposition temperatures as well. Only at relatively high annealing temperatures (samples 2 & 3), system can gain enough thermal energy to overcome energy barrier of homogeneous nucleation and initiate nucleation with constant rate during the crystallization process. This observation is in a good agreement with higher values of Avrami exponent for samples 2 & 3, as well as reduction trend in domain size at $T_d = -50^{\circ}$C samples, which is in consistence with increase of number of nuclei with temperature.

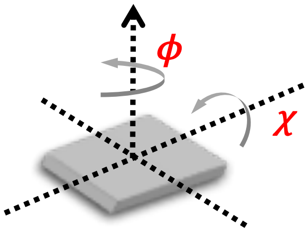

Figure 5.11: The definition of the sample tilt angle χ and azimuthal angle ϕ.

Table 5.2: Comparison of crystal domain sizes along (004) and (222) derived from both GIWAXS and LSM.

Domain size (nm)	(004)	(222)
GIWAXS peak widths	50.5	38.0
LSM simulation	50.	42.

5.8: Discussion and Conclusion

In situ GIWAXS measurements and level-set simulation were carried out to characterize the isothermal crystallization processes of PLD-deposited In_2O_3 thin films. Three sets of In_2O_3 films with the same thickness but differed in deposition temperatures T_d (-50, -25, 0 °C) were prepared and each set was investigated under three annealing temperatures T_A. The real-space structural evolvements were monitored and recorded by 2D diffraction images, from which the degree of crystallinity χ_c as a function of annealing time t was extracted and calculated. It is found that for the films deposited at the same T_d, as annealing temperature increased, incubation time for starting transformation decreased and system undergoes faster crystallization. Moreover, a higher T_A was required for films with lower T_d if all films have the same transition time. The 2D diffraction patterns of the after-annealed crystalline film showed texturing feature for film deposited at 0 °C. Pole figure from both EBSD and X-ray measurements confirmed a highly-textured film formed with a preferred orientation along the (004) direction, and the analysis of the line-cut profile yielded a 23.1° angular distribution. These results indicated that for films deposited at higher T_d (0°C), more relaxed structure was formed, along with the formation of possible nanocrystalline inclusions in the as-deposited amorphous film. Finally, a more detailed understanding of crystallization kinetics was revealed by level-set simulation based on experimental parameters derived from X-ray measurements. Interface growth velocity and nucleation density were calculated for the textured microstructures, and the activation energy associated with growth was calculated as well. It was also shown that the formation of nanocrystalline inclusions is probably the origin of heterogeneous site-saturation nucleation (SSN), which can be accompanied by constant nucleation rate (CNR) at higher annealing temperatures.

Chapter 6 : Amorphous to Crystalline Transition of In-X-O Films

6.1: Introduction

The research described here is an extension from the previous chapter. In Chapter 5, I investigated the effects of deposition temperature on the thermal stability of PLD-synthesized In_2O_3 films. While in this chapter, I will focus on the effects caused by the doping of secondary metal cations.

As motivated in Chapter 5, compared to the electrical properties of AMOs, the thermal properties lack of enough attention.[7, 48, 111-115] In particular, when the dopants are introduced into the amorphous matrix of In_2O_3, the influence of the altered local structures on the subsequent material thermal stability remains unanswered. There is not a clear understanding nor an effective approach for the ternary MO system, such as tin-doped indium oxide (ITO). To address this, a comprehensive thermal stability study of three classic ternary MO systems is carefully designed and conducted to concentrate on the effects of the doped metal cations.

A series of amorphous $(In_{1-x}M_x)_2O_3$ thin films (M=Sn, Zn and Ga), each with four atomic doping concentrations (x = 5%, 10%, 20% and 30%) were deposited by PLD. All films were deposited under the same growth condition so the deposition effects, such as deposition temperature and film thickness, were minimized. The $(In_{1-x}M_x)_2O_3$ thin films were then annealed under the isochronal annealing condition. The amorphous to crystalline transition of each film was measured by employing *in situ* grazing incident wide-angle X-ray scattering (GIWAXS) technique. By analyzing the time-sequenced diffraction images, the time-evolved degree of crystallinity (χ_c), crystallization time (τ_c) and crystallization temperature (T_c) are determined. The detailed phase and texturing information of the after-annealed crystalline films are also studied.

6.2: Sample Preparation

$(In_{1-x}M_x)_2O_3$ films (M= Sn, Zn and Ga; x=0.05, 0.10, 0.20 and 0.30) with 300 nm thicknesses were grown by PLD using dense hot-pressed In_2O_3, ZnO, SnO_2, and Ga_2O_3 targets (25 mm diameter). PLD was accomplished with a 248 nm KrF excimer laser with 25 ns pulse duration and operated at 2 Hz. The 200 mJ/pulse beam was focused onto a 1 mm × 2 mm spot size. The targets were rotated at 5 rpm to prevent localized heating. The target-substrate distance was fixed at 10 cm. To achieve films with two metal cations, a computerized shuttle was used to alternate ablation between two targets, and the ratio of the pulses for each metal oxide in each cycle was adjusted to obtain the desired film composition. To ensure uniformity of film composition, less than one monolayer of material was deposited in a typical cycle. The films were grown on silicon substrates in an O_2 ambient of 8 mTorr. The substrates were attached to the substrate holder with silver paint and grown at a temperature of -25 °C to result in their amorphous phase. A convenient notation is defined here for all the films: IMO-x, where M is T for Sn, Z for Zn and G for Ga respectively, and *x* is the doping concertation from 5% to 30%.

6.3: In situ GIWAXS Experiment at 5BMC

In situ GIWAXS technique was employed to study the crystallization process of In-M-O system. The experiment was performed at sector 5BMC (DuPont-Northwestern-Dow Collaboration Assess Team) at Advanced Photon Source (Argonne National Lab, IL). A monochromic 20 keV X-ray beam with 20 μm by 400 μm incidence beam size was used. Incidence angle was fixed at α_i = 0.23° (critical angle α_c = 0.14° for In_2O_3 of electron density ρ=1.6 e/Å^3) with ~200 nm penetration depth to avoid scatterings from substrates. All films except IGO-20% and IGO-30% samples were annealed by using a Be dome mini chamber

(Appendix A-1). The annealing temperature gradually increased from T_0 =140 °C with β = 0.5 °C/min and annealing temperature $T_A = T_0 + \beta t$ was monitored with a thermal couple gently touching the surface. The other two IGO (x = 0.20 and 0.30) films were annealed by switching to the Anton Parr heating stage (Appendix A-2) to meet the higher annealing temperature requirement. The ramping rate of annealing process was set to be $\beta = 1$ °C/min due to the instrumental limitation. All samples were annealed under 40 mTorr air pressure so the oxygen partial pressure was 8 mTorr. A Mar165CCD (2048 by 2048 pixels; pixel size 79 µm) area detector was placed ~180 mm away from the sample to collect a 100 s exposure-time GIWAXS diffraction pattern in 120 s time intervals. The 2D area detector was calibrated by XRD from a lanthanum hexaboride (LaB_6) standard powder sample. An X-ray shutter-closed, dark image was recorded for background subtraction. The diffraction images were then subsequently converted from pixel into Q-space, where Q (= $4\pi\sin\theta/\lambda$) is the momentum transfer.[116]

6.4: Qualitative Analysis of Kinetics of Crystallization Process

Similar to Figure 5.2 in section 5.4, the time-sequenced 1D $I(Q)$ *vs.* Q diffraction patterns for all 12 $(In_{1-x}M_x)_2O_3$ films can be converted from the 2D GIWAXS diffraction images, which are summarized in Figure 6.1. Each subplot is made of a series of 1D patterns with the increase of annealing temperature to show the amorphous to crystalline transition. Using ITO-5% film as an example, from 140°C to 230°C, the patterns exhibit two broad amorphous scattering peaks, after which the diffraction peaks grow in time with the reduction of the amorphous peaks (235 to 245°C). A set of strong and sharp crystalline peaks are formed when temperature reaches 250°C showing the formation of large crystalline domains. The diffraction peaks are found to correspond to the bixbyite In_2O_3 structure (Figure 2.6).

It is interesting to note that for IZO-20% film, additional diffraction peaks are shown located between Q = 2~2.5 Å^{-1} when the annealing temperature is higher than 400°C. This indicates the formation of a phase apart from the typical cubic In_2O_3.

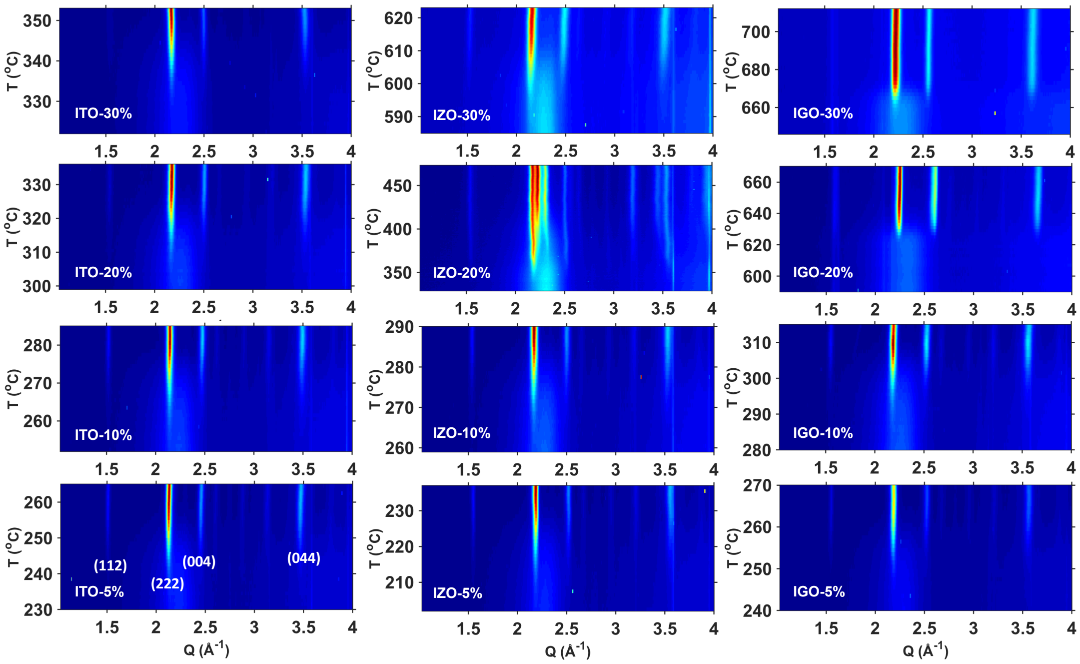

Figure 6.1:1D X-ray diffraction patterns converted from 2D diffraction images plotted as a function of annealing temperature for $(In_{1-x}M_x)_2O_3$ films (M= Sn, Zn and Ga; x=0.05, 0.10, 0.20 and 0.30) respectively. The narrower bright lines scattered between Q = 3.5 Å^{-1} to 4 Å^{-1} in IZO-20% and 30% cases are due to the Be dome scattering. The graphite dome scattering has been marked out for IGO-20% and IGO-30% cases before the conversion.

To make a more qualitative comparison, the time-evolved degree of crystallinity χ_c is extracted by analyzing each 1D diffraction pattern with the Ruland's methods[117, 118] (Chapter 5.4). A representative degree of crystallinity χ_c as a function of temperature plot is presented in Figure 6.2a. χ_c has a 0 to 1 transition over the chosen temperature range, which corresponds to the amorphous to crystalline transition.

➢ Crystallization temperature T_c and crystallization time τ_c

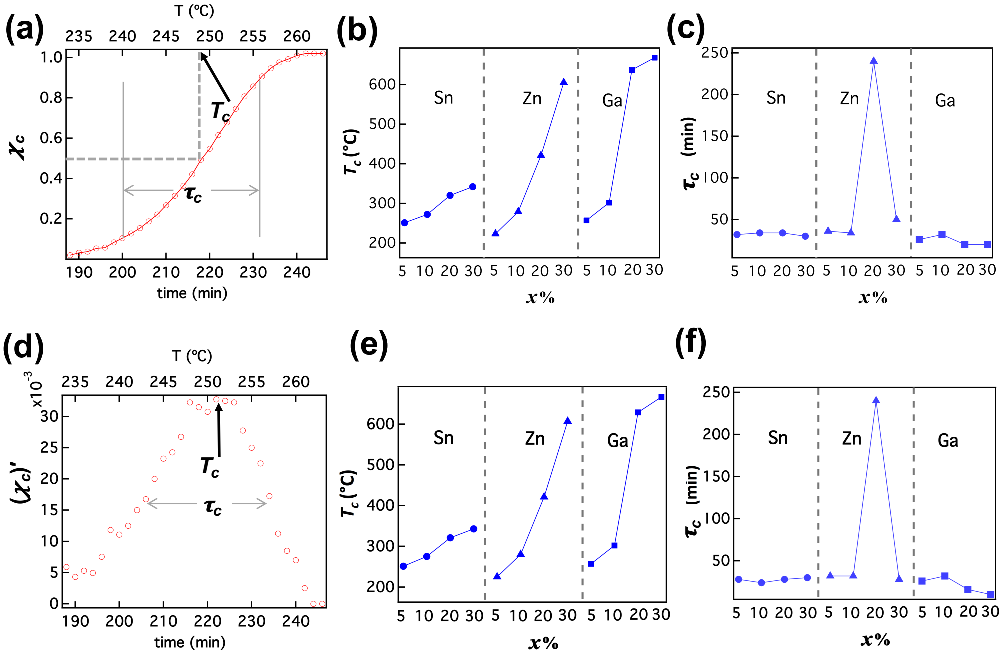

Figure 6.2: (a) The degree of crystallinity χ_c evolvement as a function of annealing temperature T or annealing time (t) for the ITO-5% sample. The characteristic crystallization time (τ_c) and crystallization temperature (T_c) is defined and indicated by arrows in (a). Based on this definition, the extracted T_c and τ_c of all 12 crystallization curves are summarized in (b) and (c) respectively. (d) An alternative definition of T_c and τ_c by extracting the peak position and width of the gradient profile of χ_c. The corresponding results are summarized in (e) and (f).

A simple approximation of the crystallization time τ_c is computed by the time difference between the film reaching 10% and 90% crystallinity (the same as in Chapter 5). For our isochronal annealing case, there is no explicit definition about crystallization temperature T_c since the temperature is continuously increasing. So, T_c is defined as the annealing temperature at 50% crystallinity for convenience.

The summary of extracted crystallization temperatures T_c and time τ_c for all crystallization curves is shown in Figure 6.2b and 6.2c. Note that the crystallization temperature of pure indium oxide thin film deposited at the same T_d = -25 °C is ~ 180°C (Chapter 5). Hence, all the $(In_{1-x}M_x)_2O_3$ thin films have higher crystallization temperature than that of In_2O_3. This indicates the introduction of secondary metal ions will hinder the crystallization process and elevate the crystallization temperature.

For the ITO case, T_c values are 251, 272, 320 and 342 °C for x = 5%, 10%, 20% and 30%, respectfully. The relation between crystallization temperature and concentrates is relatively linear. A similar trend is observed for IZO case, but the relation becomes more exponential. T_c values are 223, 279, 421 and 605 °C for x from 5% to 30%, respectfully. At the higher doping concentration (20% and 30%), much higher T_c is needed for Zn. This suggests that doping of Zn is more thermally stable than Sn. When doping Ga at low concentration x (5% and 10%), IGO films have comparable T_c (257°C and 302°C) to the ITO and IZO films. However, at higher concentration x (20% and 30%), even higher crystallization temperatures are needed. Not that the ramping rate changes from 0.5 to 1 °C/min due to the switch of heating stage. This often leads to a higher crystallization temperature. However, partially or no crystalline features were shown for IGO-20% and -30% films when using Be dome heating stage and reaching the limitation at 600 °C. Hence, the T_c for the IGO-20% and IGO-30% cases should be at least > 600 °C, which still points out that Ga is more thermally stable than Zn.

The comparison of crystallization time τ_c is also important to estimate how fast the crystallization process is. As shown in Figure 6.2c, besides IZO-20% case, the crystallization time of the rest films ranges about 28~36 mins. It means that once the crystallization starts, the transition time for all the films is about the same. Note that a faster crystallization time τ_c is observed for IGO-20% and 30% cases, which likely result from the larger ramping rate β and higher annealing temperature T_A. The τ_c of IZO-20% (240 mins), is much larger than the rest. This is related to the new phase forming during the amorphous to crystalline transition. The detailed crystallization process will be described later.

6.5: ITO Case

The crystalline diffraction pattern at the end of the crystallization process is also informative to understand the crystallite orientations, phase separation and indications of the nucleation and growth of the crystallites.

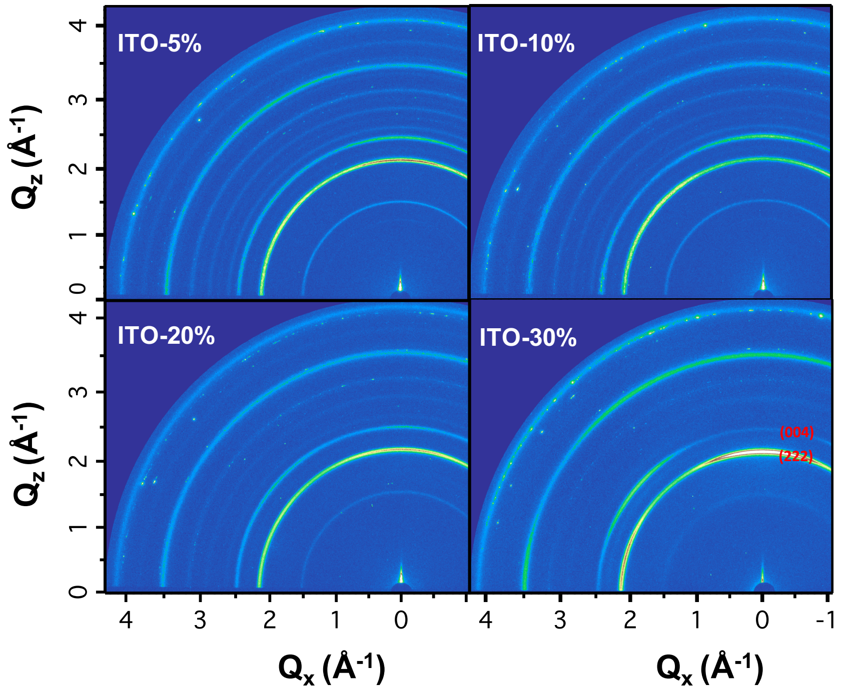

Figure 6.3: The 2D crystalline diffraction patterns at the end of crystallization process ($\chi_c \rightarrow \mathbf{1}$) for $(In_{1-x}Sn_x)_2O_3$ with x=0.05, 0.10, 0.20 and 0.30.

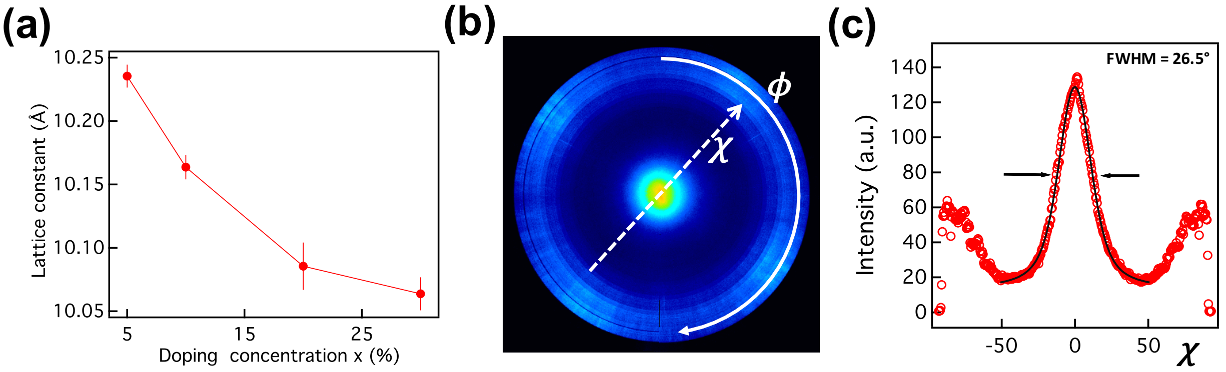

Figure 6.4: (a) Lattice constant a derived from 1D X-ray patterns as a function of doping concentration for ITO films; (b) (111) pole figure of ITO-30% sample showing (111) texturing; (c) quantitative line-profile generated along the dash arrow in (b) with a Gaussian fitting.

The diffraction images of the crystalline Sn doped In_2O_3 thin films are presented in Figure 6.3. All four patterns showed polycrystalline features with peak positions matching to typical bixbyite In_2O_3 structure (space group# 206, $Ia\bar{3}$) without the presence of SnO_2 diffraction peaks. This indicates that Sn is the substitute of In in the ITO samples. The lattice constant *a* variation induced by doping Sn can be studied as well. The result derived from fitting 1D crystalline XRD pattern is presented in Figure 6.4a. All four samples have a larger lattice constant *a* than that of the ideal bulk In_2O_3 (10.01 Å). A decreasing trend in lattice constant is observed as the doping of Sn is increased. This can be explained because Sn has a smaller ionic radius (Sn^{4+} = 83 pm) than In^{3+} (94 pm), which leads to a smaller lattice parameter.

The other phenomenon that is worth investigation is the texturing presented in ITO-30% case. For $x \leq 20\%$, the intensities of diffraction rings are uniformly distributed indicating a non-textured film formed at the end of the crystallization. However, for $x = 30\%$, a strong (222) diffraction peak and the omition of the (004) peak along the Q_z direction indicates that the crystallites have a preferred orientation along the [222] direction. A pole figure measurement at (222) diffraction condition was conducted to quantitatively analyze this texturing. The result is presented in Figure 6.4b. A bright spot located in the center of the pole figure means the orientation distribution concentrates along [222] direction. A line profile extracted from Figure 6.4b is presented in Figure 6.4c. A Gaussian fit to the line profile data shows the preferred orientation is (222) with an angular distribution of 26.5°. Therefore, at high doping concentration of Sn, the texturing induced by dopants is observed during the amorphous to crystalline transition.

6.6: IZO Case

The summary of 2D diffraction patterns of after-annealed IZO films are presented in Figure 6.5. The diffraction patterns of IZO-5% and 10% show the similar polycrystalline feature as in the ITO case, which indicates the formation of non-texturing polycrystalline film with bixbyite In_2O_3 crystal structure. The lattice constant analysis yields a = 9.96 Å and a = 10.0 Å for IZO-5% and IZO-10% films, respectively. These results are comparable to the lattice parameter of the bulk In_2O_3, showing no significant strain effects. Additional diffraction peaks are seen when increasing Zn atomic composition to 20%, which suggests the formation of new phase. At last, when concentration increased to 30%, In_2O_3 diffraction peaks are observed without the presence of additional peaks and the extracted lattice parameter is a = 10.0 Å, which is similar to the 5% and 10 % cases.

To further investigate the new phase in the IZO-20% case, time-sequenced 1D diffraction patterns are selectively chosen to represent the detailed feature of the amorphous to crystalline transition and illustrated in Figure 6.6a. At T = 329 °C, a crystalline diffraction peak (Q = 2.18 Å^{-1}) merges on the top of a broad amorphous diffraction peak with its position matching with bixbyite In_2O_3 (222) diffraction. When T is gradually ramped up to 348 °C, the main (222) peak becomes stronger and the other diffraction peaks of bixbyite structure start to show up indicating the growth of crystallites. Starting from T = 329 °C, an additional set of peaks located at Q = 2.21, and 2.32 Å^{-1} appear, and the intensity of the peaks become higher and supersede the (222) peak. This implies the formation of a new phase. To further identify its crystal structure, the diffraction pattern at T = 458°C is analyzed and shown in Figure 6(b). The peaks are fitted with a Pseudo-Voigt function on a linear background. The analysis reveals that the additional peaks most likely originate from the In_2O_3-based rhombohedral structure (space group# 167, $R\bar{3}c$). This is supported by some previous reports on the observations of rhombohedral In_2O_3 or Zn doped In_2O_3.[131] Therefore, two crystalline phases coexist within the IZO-20% crystalline film.

The kinetics of the crystalline phases during the annealing process are explored as well since the transition time (τ_c) deviates from the rest (Figure 6.2b). From Figure 6.6a, the two crystalline phases do not transform simultaneously. The cubic phase appears before the rhombohedra phase. Hence, two sets of peaks are chosen in Figure 6.6b to quantitatively represent the amorphous to crystalline transition of both crystalline phases. The major diffraction peaks (222) and (004) of the cubic bixbyite structure are selected and denoted as C-(222) and C-(004). Another two peaks related to rhombohedral structure are selected and denoted as R-(014) and R-(110). The areas under the four peaks are calculated for the time-resolved 1D X-ray diffraction patterns to illustrate the peak evolution. The result is presented in Figure 6.6c. The C-(222) and C-(004) peaks have a sharp increase at *T* ~360 °C suggesting the transition temperature of amorphous phase to cubic crystalline phase. The transition of R-(014) and R-(110) peaks happens later at *T* ~405 °C. The simultaneity of the R-(014) and R-(110) transition curves points out that they are originated from the same crystal structure. At the end, all the areas gradually approach relatively steady values. The overall evolution indicates that part of the amorphous phase transforms to cubic crystalline phase first, and then the rest transforms to rhombohedra phase, and finally result into a coexisting phase. The four peaks used in the previous analysis have also labeled in 2D crystalline diffraction pattern (Figure 6.6d). The diffraction peaks from the rhombohedra structure have a strong texturing with R-(110) pointing along the in-plane direction. On the contrary, diffraction peaks from cubic crystalline phase do not have textured features.

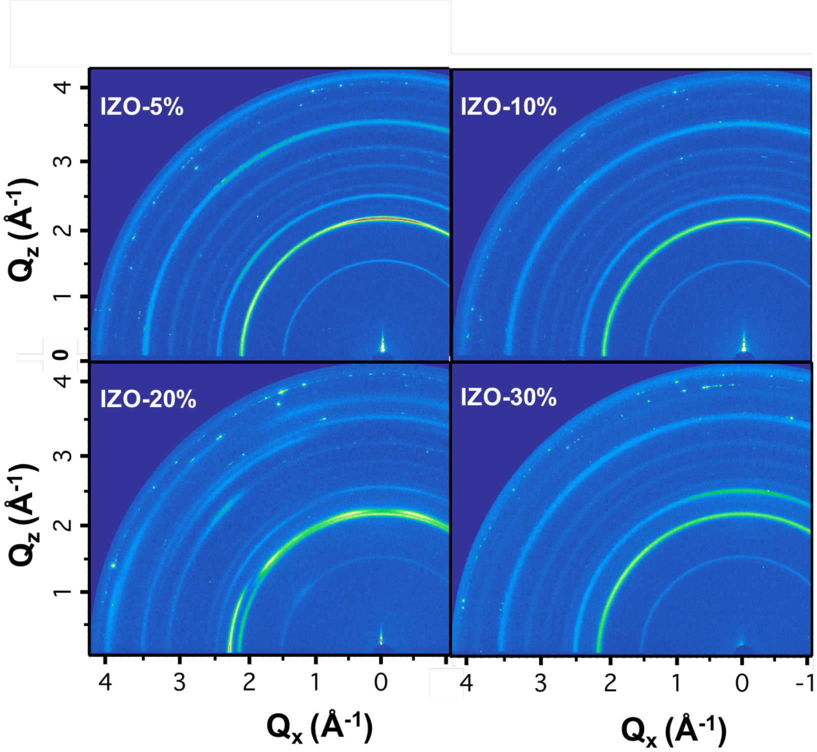

Figure 6.5: The 2D crystalline diffraction patterns at the end of crystallization process ($\boldsymbol{\chi_c} \rightarrow \mathbf{1}$) for $(In_{1-x}Zn_x)_2O_3$ with x=0.05, 0.10, 0.20 and 0.30.

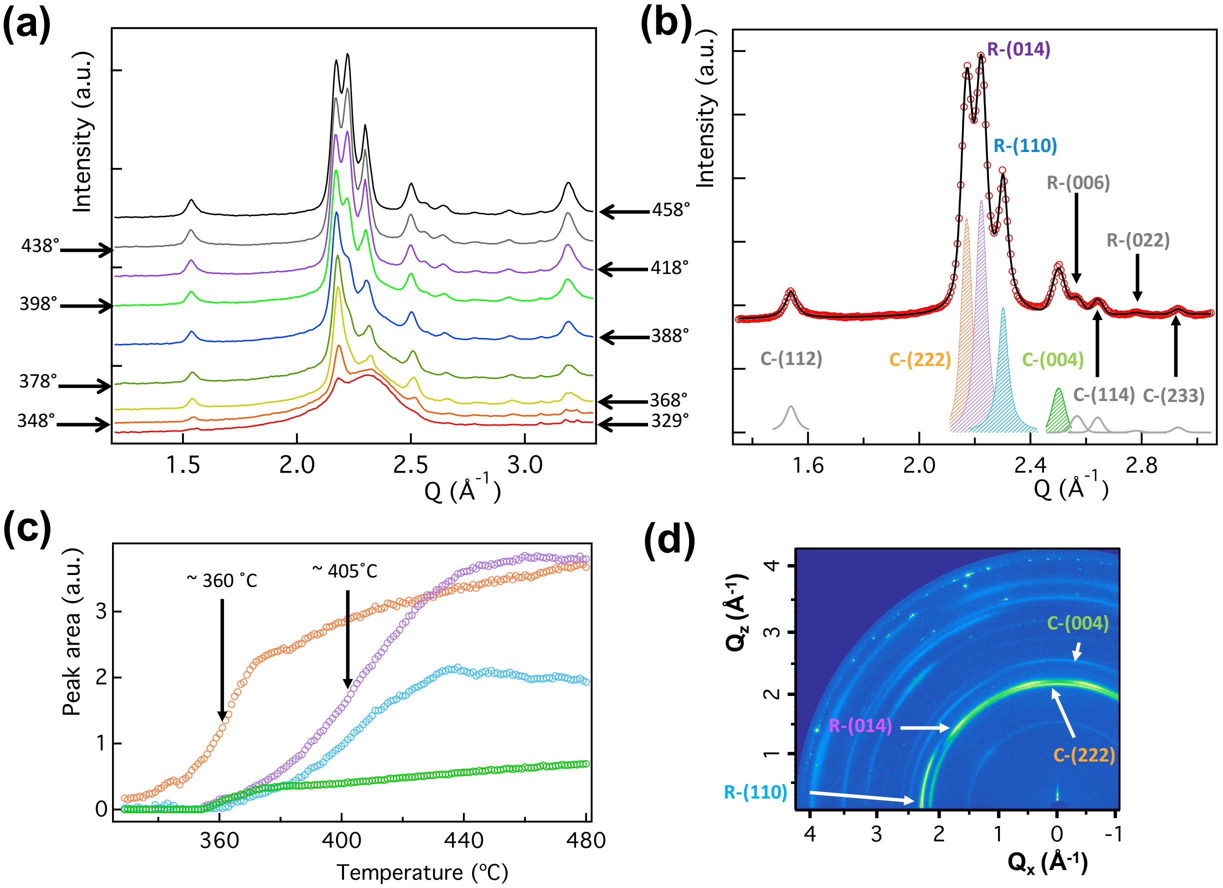

Figure 6.6: (a) Temperature dependent 1D X-ray patterns of IZO-20% film; (b) XRD pattern of after-annealed crystalline IZO-20% film and its peak fit results based on both rhombohedra (R) and cubic structure (C). The area under the four major peaks are color labeled; (c) The evolution of peak areas, defined in (b), as function of annealing temperature; (d) 2D diffraction image of crystalline IZO with four major peaks labeled.

6.7: IGO Case

When Ga is doped into In_2O_3 films, similar but different features are observed compared to the doping of Sn and Zn. The 2D GIWAXS images are shown in Figure 6.7. IGO-5% has the same polycrystalline diffraction rings showing the formation of bixbyite structure. Uniform intensity across each diffraction ring indicates the non-texturing polycrystalline feature. The derived lattice parameter a = 9.96 Å is close to that of IZO-5% and bulk In_2O_3. A (004) texturing is first shown when increasing the Ga atomic doping percentage to 10%. However, at the same percentage, both ITO and IZO films do not show the texturing feature. A more pronounced (004) texture is observed for IGO-20% film. This implies the doping of Ga would facilitate and constrain the growth of crystallites in the preferred direction. This effect has not been observed for the Zn and Sn cases. Strong texturing is also illustrated by the IGO-30% 2D diffraction pattern but its feature is different from that of IGO-20% film. Bright diffraction spots on the top of polycrystalline (222) diffraction rings suggests the formation of large crystallites within the film. Pointed out by the white arrows between (044) and (004) diffraction peaks, the higher order (*hkl*) peaks are absent from the diffraction pattern. This is likely due to structure distortion from the incorporation of Ga in the In_2O_3 lattices. These high order (*hkl*) peaks are intrinsically weak peaks compared to (222) and (004), therefore, the incorporation of Ga into the lattice will further diminish it. Similar effects have also been seen for both Sn and Zn cases at high doping percentages but those peaks are still observable. The detailed analysis of the texturing of the IGO-20% and IGO-30% was carried out by the pole figure measurement and presented in Figure 6.8. From Figure 6.8a, the two sets of rings at different χ positions indicate that IGO-20% film has two major preferred orientations. The first one located at $\chi = 54°$, and this corresponds to the (004) orientation. The other located further at $\chi = 71°$, which corresponds to $(2\bar{2}2)$ orientations. Combined with GIWAXS pattern in Figure 6.7, (004) texture is dominated along the out of plane direction. As opposite to IGO-20% film, the IGO-30% shows a preferred (222) orientation along the out of plane direction with a bright spot located in center of the pole figure, and another preferred orientation is $(2\bar{2}2)$ with a narrow ring located at $\chi = 71°$. Note that as suggested by GIWAXS pattern of IGO-30% in Figure 6.7, there are still a portion of non-textured polycrystalline feature shown.

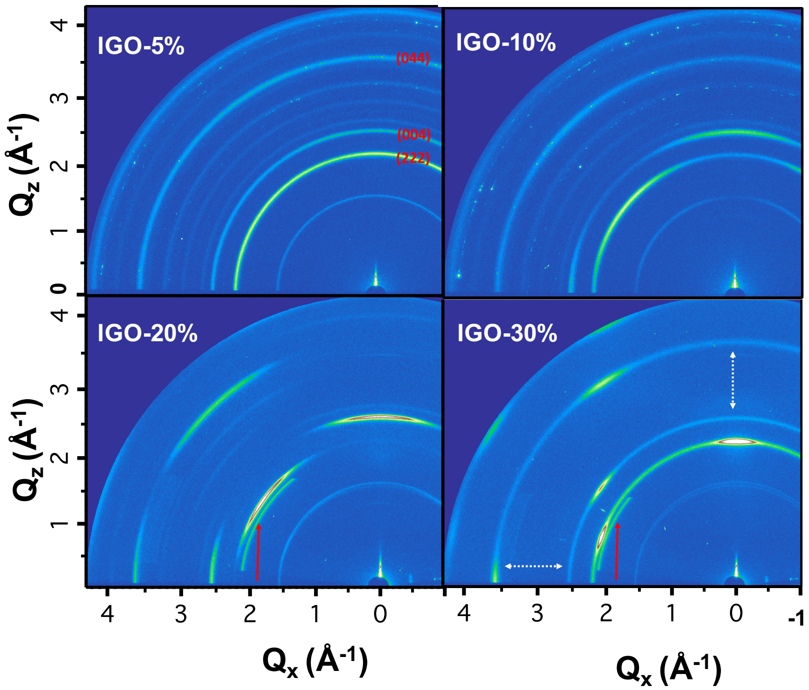

Figure 6.7: The 2D crystalline diffraction patterns at the end of crystallization process ($\boldsymbol{\chi_c} \rightarrow \mathbf{1}$) for $(In_{1-x}Ga_x)_2O_3$ with x=0.05, 0.10, 0.20 and 0.30. The diffraction from the graphite dome is also indicated by red arrows for both IGO-20% and IGO-30%.

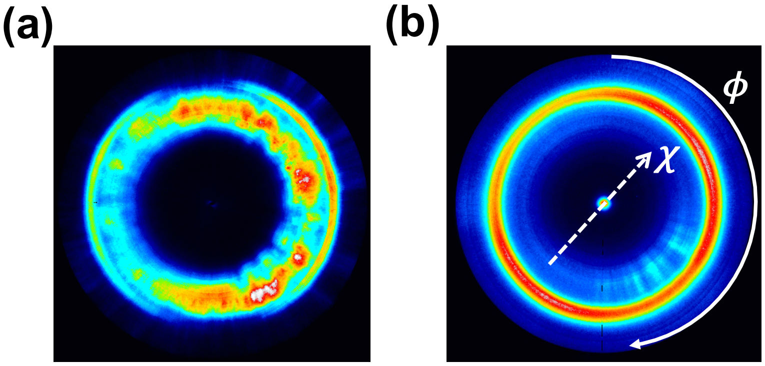

Figure 6.8: Pole figures measured at (222) Bragg condition for IGO-20% (a) and IGO-30% (b).

6.8: Conclusion

In situ GIWAXS measurements were carried out to characterize the isochronal crystallization processes of PLD-deposited In_2O_3 thin films doped with Sn, Zn and Ga. Through the symmetric comparison of crystallization time and crystallization temperature, the effects of the secondary metal cations on the thermal stability of AMOs were revealed. It shows that the introduction of dopants elevates the crystallization temperature, and enhances the thermal stability compared to the pure In_2O_3 thin films. For each of the three dopants, the increase of dopant concentration from 5% to 30%, also improves the thermal stability of AMOs. Compared to Sn, the doping of Zn and Ga are relatively more effective in maintaining the amorphous state. This difference should result from the local distortion induced from the dopants. Hence, due to the similarity of Sn cation radii and chemical properties, the elevation of crystallization is less apparent than the Zn and Ga. The Zn is known as the “amorphosizer” to the MO system, while the Ga has a high connectivity with the neighboring oxygens. The doping of both cations lead to the formation of more thermally-stable amorphous phase.

Texturing is observed in the final crystalline diffraction patterns for dopants at higher concentration. This could be due to the required high annealing temperature. For most cases, the diffraction patterns of doped In_2O_3 films matches well with the bixbyite In_2O_3 structure, but additional diffraction peaks observed for IZO-20% cases indicate the formation of a new phase. It is later determined as rhombohedral structure. Similar observations reported by a few other groups points out the doping of Zn at 20% facilitates the formation of rhombohedral phase or induces a unique co-existence of two phases, which typically requires high annealing temperature or high pressure. The rest cases with well-matched diffraction patterns confirm the role of dopants as a substitute.

Chapter 7 : Towards the Understanding of Amorphous Structure

7.1: Introduction

In this chapter, both the microscopic and macroscopic characterization of AMOs will be discussed. As stated in Chapter 2.4.2, the properties of AMOs can be tuned through various doping, such as doping of secondary or multiple metal cations. Due to the lack of long-range ordering, the study of AMOs switches to the detailed local characterization, namely the coordination environment around the interested metal cations, and how it evolves after introducing the dopants. Hence, I will first introduce a few doped AMOs systems, and how to probe and understand the amorphous phase by using the EXAFS technique (Chapter 3.3.2). With the help from advanced simulation techniques such as density functional theory (DFT), the band structure, electrical and optical properties, and a statistical averaging of local environments can be obtained as well.

The other approach to understand amorphous phase is by comparing the density of materials, especially to the expected bulk density. Typically, amorphous phase should have smaller density than the crystalline phase since the latter one is more structurally relaxed. For the solution-processed films, the exothermal reactions produce gases and evaporates the solvents while rapidly form a solid-phase oxide film. The consequence is the creation of large holes in the freshly prepared films. And this porous structure will certainly expect to have a smaller density compared to the ideal bulk structure. The direct measurement of mass density is rather inaccessible for the thin film structure. So, the electron density measured from X-ray reflectivity (Chapter 3.2.3) provides alternative way to determine both the mass density with the known stoichiometry, and the porosity by comparing to the ideal bulk or single crystal material.

7.2: Secondary Metal Ions Size (Sc, Y and La) Effects

Chapter 7.2 is adapted from a published work REF[103].

The doping of secondary metal ions has been discussed in Chapter 2.4 along with some of the famous ternary and quandary crystal structures. However, besides the well-known ones, such as Ga, In or Zn, there are still many transition metals in periodic table that largely remained unexplored. Sc, Y and La are in the same column in the periodic table with very similar chemical properties but differ in ionic radii: range from 0.95 $R_{ionic}(\mathrm{In}^{3+})$ to 1.25 $R_{ionic}(\mathrm{In}^{3+})$. The size of the cation, which is determined by its electron configuration, will therefore be the dominant variable in this series and is expected to result in changes to the oxide properties. In this contribution, we focus on the In-X-O system, where X = Sc, Y, La, with X concentrations varied between 2.5 and 12.5 at%, which crosses the crystalline-to-amorphous transition while maintaining complete oxide solid solutions. Samples are all made through "combustion" solution processing methods with step by step spin-coating and post-annealing. Two annealing temperatures 250˚C and 300˚C were used to produce two sets of In-X-O films.

X-ray absorption spectroscopy (XAS) analysis (Chapter 3.32, eq. 3.11) is one important method used to probe AMO materials on the ~5 Å length scale and provides information on coordination number (CN), average atomic separations (R), and atomic positional disorder (σ^2) of the different shells surrounding the central absorbing atom. The experiments were conducted at sector 5BMD of the Advanced Photon Source of Argonne National Laboratory (ANL). A Si(111) double crystal monochromator was used to produce a 12 mm (horizontal) by 1 mm (vertical) beam. The incident beam energy was tuned to near the In K-edge (27940 eV). Films were placed 45° from the incident direction, and data were collected under fluorescence mode by using a four-element silicon drift detector (SII NanoTechnology). The reference powders were uniformly spread on Scotch tape (3M Corp.) and measured through transmission mode by using ionization chamber (Oxford-Danfysik).

EXAFS spectra were extracted and normalized by using ATHENA software packages. [132] The intrinsic loss factor (S_0^2) for fitting the indium *K* edge was obtained by modeling of the reference powders for each absorbing atom, and kept fixed when fitting the film data. The bond distances, coordination numbers, and Debye-Waller factors were obtained by the FEFF simulations using a cluster of the bixbyite structure with a radius of 6 Å centered on the absorbing atom. All the normalized absorption coefficients χ(k) were Fourier transformed using a Hanning window over the specified *k*-range and fit in *k*-space with *k*-weight 3. The summery of fitting parameters of the first two shells are listed in Table 8.1 based on eq.(3.11).

Table 7.1: EXAFS fitting parameters for the first In–O and In–M (M = In or X) shells.

	T_a (˚C)	N_i		R_i (Å)		σ_{Ri}^2 (10^{-3} Å^2)	
		In–O	In–M	In–O	In–M	In–O	In–M
In-Sc-O	250	5.62	3.04	2.152	3.358	6.45	7.02
In-Y-O	250	5.54	2.20	2.151	3.316	7.45	8.13
In-La-O	250	5.11	2.4*	2.156	3.340	7.10	9*
In-Sc-O	300	5.95	4.21	2.166	3.363	6.29	4.46
In-Y-O	300	5.75	3.62	2.155	3.365	6.96	7.46
In-La-O	300	5.56	3.32	2.147	3.368	7.69	13.5

For all films the calculated radii R_i are relatively constant at 2.16 Å for the In–O shell and 3.36 Å for the In–M shell, which are comparable to the radii for crystalline In_2O_3 reference powder samples. The reductions in peak intensities in the *p*-RDF especially for shells beyond the first In–M correspond to a decrease in the coordination number and increased Debye-Waller factor in these shells, which are commonly seen as films become semi-crystalline or amorphous. As the size of the secondary cation, X, increases N_i decreases whereas σ_{Ri}^2 increases. This effect is much more pronounced for the In–M shell, suggesting that InO$_x$ polyhedral remain relatively intact in the amorphous structure while disorder arises from distortions to the polyhedral network, i.e., their interconnectivity. When comparing films annealed at 250 and 300˚C, the lower processing temperature leads to a greater drop in In–M coordination number—between 2.1 ~ 3.0 at T_a = 250˚C versus 3.3 ~ 4.2 at T_a = 300˚C. We can thus conclude that the introduction of larger secondary cations and/or lowering the processing temperature increases the amorphous network disorder moving further away from the crystalline structure. In particular, for the most amorphous samples we are approaching the "EXAFS-free" case where all shells beyond the first In–O have very low intensities. This even makes extraction of a unique In–M coordination number and Debye-Waller coefficient impossible in the In-La-O case with T_a = 250˚C (the symbol * in Table 7.1). It is important to note that the effect of the 50˚C change in T_a seems to have a larger effect than moving from X = Sc to X = La.

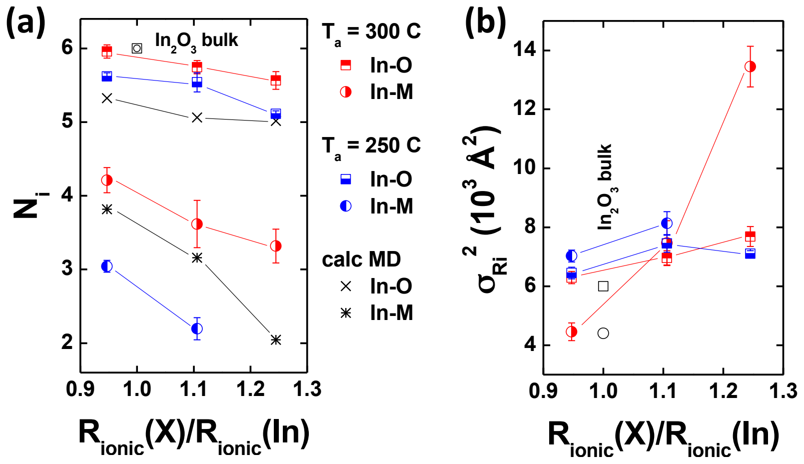

Figure 7.1: Fitting parameters from the IXO EXAFS measurements and *ab initio* MD simulations plotted as a function of the ionic radius of the X cation normalized to the radius of In^{3+}. (a) The change in coordination number, *N,* for both the In–O and In–M (M = In or X) shells. (b) The same for the change in Debye-Waller factor coefficient, σ_{Ri}^2.

Note that this case also indicates that the EXAFS characterization technique has its own limitation when apply to amorphous materials; in our case, it is the inability to distinguish the second and third shells scatterings.

7.3: The Effects of Polymer Doping to Metal Oxides

Adding polymer to the precursor solutions have shown to be an effective route to form high-quality materials. Besides the physical vapor deposition, and solution-based processing methods (Chapter 2.4.3), polymer assisted deposition (PAD)[133], provides another strategy for the growth of thin films. Unlike the sol-gel based precursor solutions, in which metal cations are coordinated with solely hydroxyl group (OH^-) or nitrate group (NO_3^-), the PAD typically is an aqueous chemical solution route which coordinates metal cations with polymers. The use of polymers to bind metal cations forms much larger metal-organic complexes, which allows for the filtration of unbounded species. The decomposition and removal of polymer chains also facilitate a gentler and more ordered formation of materials. Thus, PAD has been used and demonstrated to be successful for many oxides and nitrites systems.[134, 135]

Our research did not follow the exact same procedure as PAD method, but it led to the idea of introducing polymers into the conventional solution processed route to facilitate the formation of thin films with higher mechanical flexibility. Moreover, by adding polymer with potential electron doping capability, the tunability of device mobility can also be achieved.

In the next two sections, I will present the detailed structural characterizations of In_2O_3 thin films made from different polymer doped precursor solutions by using EXAFS and XRR.

7.3.1: The Doping of PVP

Chapter 7.3 is adapted from a published work REF[105].

The first example is adding poly(4vinylphenol) (PVP) into precursor solutions. The thin films are made with the following procedures:

- the In_2O_3 "combustion" precursor is first prepared: 177.4 mg $In\cdot(NO_3)_3\cdot xH_2O$ is dissolved in 10 ml of 2-methoxyethanol before the addition of 55 μL of NH_4OH and 100 μL of acetylacetone. PVP was also dissolved in 2-methoxyethanol overnight to form 10 mg/ml solution. Approximately 4 h prior to the spin-coating, the In_2O_3:polymer precursor solutions were prepared by mixing and stirring In_2O_3 combustion precursor and PVP with various concentrations. For the EXAFS study, only two concentrations are explored 1 and 5 wt %.
- The neat In_2O_3 and In_2O_3:polymer precursor solutions are deposited by spin-coating at 3500 rpm for 30 s, and then annealed on a hot plate at temperatures of 250 °C for 30 min for each layer. This process was repeated 4 times to achieve desire thickness.

The EXAFS experiment was conducted to study the microstructures within the PVP doped MOs. Three thin film samples were prepared through "combustion" process with 250 °C processing temperature: neat In_2O_3 film, MO:polymer films with 1% and 5% PVP concentrations. EXAFS at In *K* edge experiments were also performed at sector 5 at advanced photon source (APS) at Argonne national lab (ANL). However, instead of putting the sample 45°

from the incident beam, a grazing incident geometry is used. The setup was very similar to Figure 3.14, without an area detector. Two 4-element fluorescence detectors were placed perpendicular to the X-ray beam and pointing at the samples vertically.

Figure 7.2 presents the comparison of the *p*-RDFs and fitting results of three films samples and In_2O_3 reference powder with a two-shell model and fitting range of k=3 ~ 11 Å^{-1}. The first shell In-O CN of In_2O_3:polymer films: 5.7 for MO:1% PVP, and 5.6 for MO:5%PVP, showing slightly under-coordinated compared to CN=6 for bulk In_2O_3 powder and undopped film. While for the second shell, CN decrease more apparently from 6 in In_2O_3 powder and 5.08 in neat In_2O_3 film to 4.05 in MO:1% PVP, and 3.81 in MO:5%PVP. The reduce of CN of first and second shells of and the increase of Debye-Waller factor of In_2O_3:polymer system indicating the crystallization was frustrated by adding PVP.

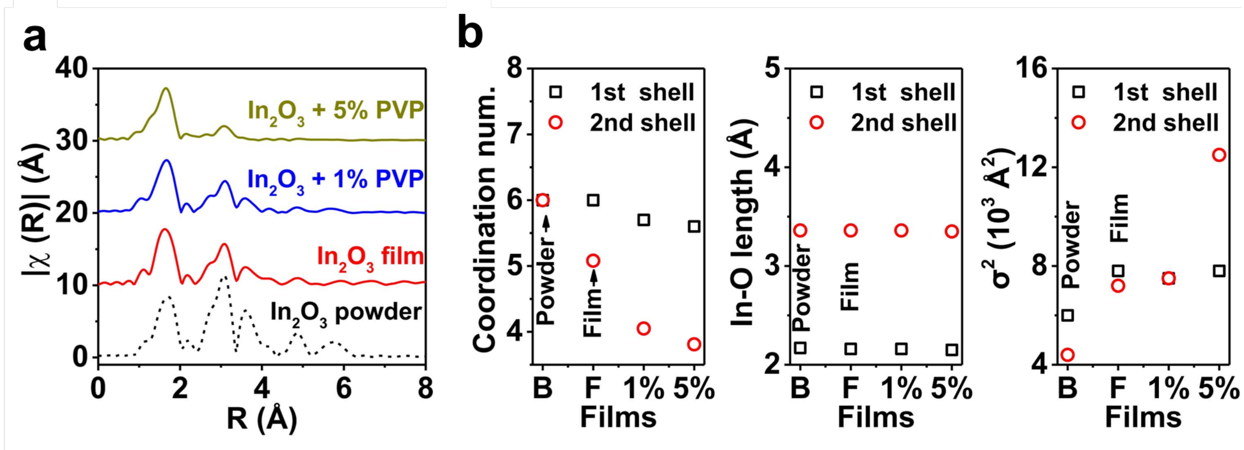

Figure 7.2: (a) Comparison of the In K-edge *p*-RDFs of In_2O_3 powder, neat In_2O_3 film, In_2O_3:polymer films with 1% and 5% PVP concentrations; (b) Coordination numbers, In-O bond length, and σ^2 of the identical films.

7.3.2: The Doping of PEI

Chapter 7.3.2 is adapted from REF[104].

The previous work of PVP doped In_2O_3 thin films results in high-performance, transparent, and mechanically flexible amorphous TFTs. However, the electron mobility (μ_e) of PVP-doped In_2O_3 TFTs monotonically falls when increasing the PVP concentration, from ~3 cm^2/Vs for the neat In_2O_3 matrix to ~1.5 – 0.2 cm^2/Vs for 10 – 20 wt% PVP doping due to the concomitant PVP charge trapping and film amorphization. The optimal device performance of an amorphous phase has an I_{on}/I_{off} of ~10^6-10^7, a V_T of ~1.2 V, and a μ_e ~ 2 cm^2/Vs, is obtained when ~5 wt% PVP is added. Consequently, as in the case of doping In_2O_3 with light elements, high on/off ratio, proper V_T, and stability are achieved by sacrificing the carrier mobility of the In_2O_3 matrix.

We studied the polymer doping of solution-processed In_2O_3 with polyethylenimine (PEI) , which also enables superior transistor performance, including the electron mobility, versus the pristine MO matrix but with a different the mechanism by which PEI operates is very different from that of PVP, by carefully controlling the polymer concentration (1-1.5 %), high mobility (maximum ~9 cm^2/Vs on 300 nm SiO_2/Si) and excellent on/off ratios (~10^7) are achieved with performance exceeding those of the pure In_2O_3 matrix (maximum μ_e ~4 cm^2/Vs). For the above reasons, EXAFS techniques were applied to gain more insight into the atomic scale structural variations of these mostly amorphous blends, in particular, the changes in the local InO_x polyhedral evolvement on introduction of PEI. For In_2O_3 powders, the three peaks for $R \leq 4$ Å correspond to the In-O (CN = 6; $R_1 = 2.19$ Å), In-In (CN = 6; $R_2 = 3.35$ Å) and In-In (CN = 6; $R_1 = 3.82$ Å) shells. Since the EXAFS peak height is related to CN while the peak position relates to bond distance, a qualitative interpretation of the blend samples can be made by comparison to

In_2O_3 powder. As shown in Figure 7.3a, with the increasing of PEI addition, the first shell CN decreases, while the second and third ones have a monotonically decline in intensity.

Quantitative EXAFS data analysis next focused on the first two shells (In-O and In-In), and data were fitted in *R*-space with *k*-weight 2. An intrinsic loss factor ($S_0^2 = 1.06$) for fitting the In *K* edge was obtained by modeling In_2O_3 powder, and held fixed when fitting the film data. The results on bulk In_2O_3 powder, a pristine In_2O_3 film, and 1.5%, 3% and 6% PEI doping are shown in Figures 7.3b and 7.3c. The CN of the first two shells of bulk In_2O_3 were both fixed at CN = 6 for reference. Unlike the first shell, the CNs of the second shells shows a stronger PEI content dependence, varying from 6 (powder) to 5.35 (0%) to 4.64 (1.5%) to 4.05 (6%), and showing increased local disorder on PEI doping. This result is consistent with the TFT mobility trends for higher PEI contents, since PEI disrupts lattice and electron conduction pathways. The derived bond lengths in both first and second shells do not vary significantly: 2.15 – 2.18 Å for first shell, and 3.37 - 3.38 Å for second shell. Overall, PEI doping disrupts lattice order, albeit to a lesser extent than PVP (see Figure 7.2)[105], leaving a sufficient density of connected InO_X polyhedra for efficient charge transport.[136]

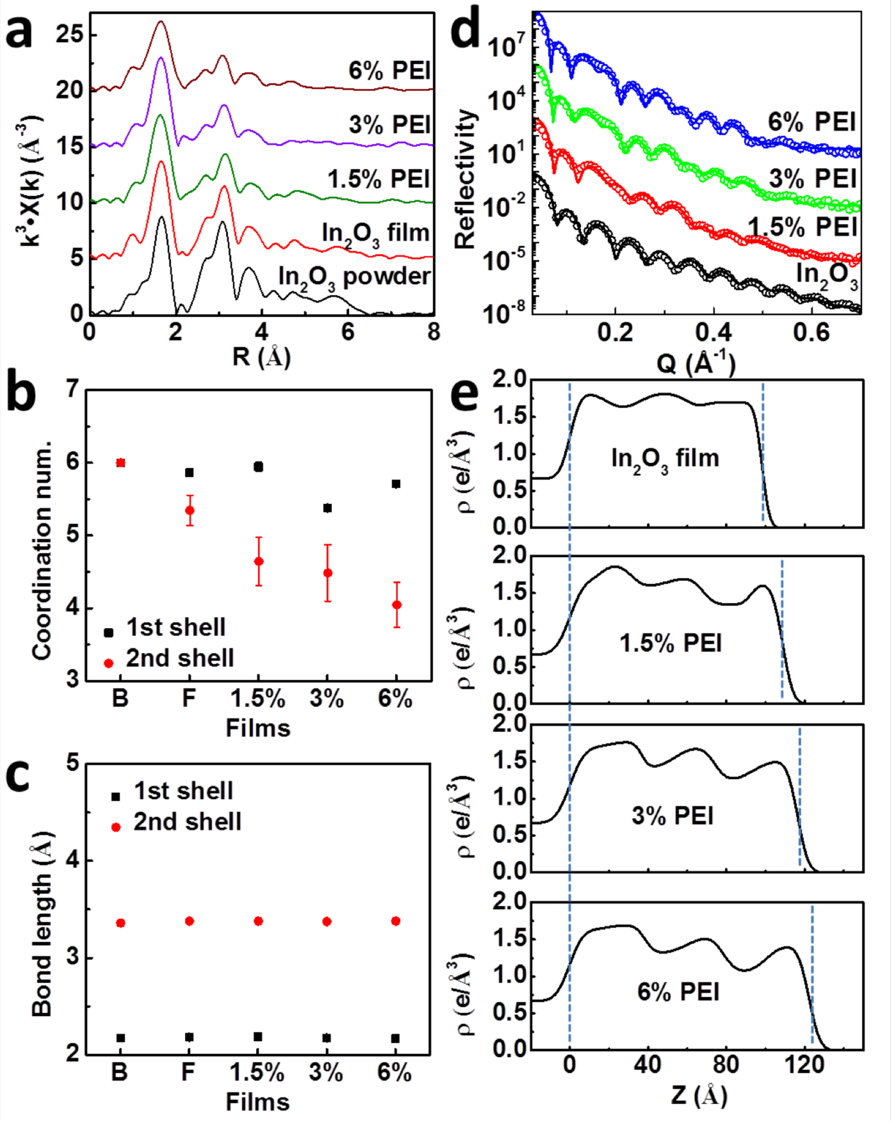

Figure 7.3: a) Comparison of the In K-edge *p*-RDFs of In_2O_3 powder, a neat In_2O_3 film, In_2O_3:x% PEI blend with 1.5%, 3% and 6% PEI concentrations. b, c) Derived coordination number, In-O bond lengths for the indicated films. d) XRR plots and e) corresponding electron densities profiles of the indicated In_2O_3:x% PEI blend films.

X-ray reflectivity (XRR, Chapter 3.2.3) was utilized to examine film quality and structural evolution upon PEI doping and step-by-step spin-coating process, since it is sensitive to film electron density, layer spacing, and interfacial roughness (Figures 7.3d and 7.3e). Recall that the In_2O_3:x% PEI films consisted of trilayers spun with the same precursor formulation. The extracted the electron density profiles are shown in Figure 7.4e. As the PEI content increases (from 0% to 6 %) the film thickness gradually increases (from ~9.8 to 12.3 nm) and the calculated average electron density decreases monotonically from ~1.7 e/Å^3 (neat In_2O_3) to ~1.6 e/Å^3 (1.5% PEI) to ~1.4 e/Å^3 (6% PEI). Furthermore, the neat In_2O_3 film exhibits a relatively uniform electron density distribution throughout the film thickness (1.6 - 1.8 e/Å^3) in spite of the first, second, third layers are annealed at 250 °C for different times. However, the electron density distributions of the In_2O_3:x% PEI blends are not as uniform as that of neat In_2O_3 (Figure 4e). For instance, for the In_2O_3:1,5% PEI film, the electron densities of the second and third layers, 1.61 e/Å^3 (second layer) and 1.40 e/Å^3 (third layer), are lower than that of the first layer (1.69 e/Å^3). Note the XPS derived M-O-M content for all films remains constant even though the film crystallinity decreases dramatically, indicating that the overall metal oxide formation remains efficient and most electron density decrease most likely reflects structural relaxation and porosity formation in the second and third In_2O_3 layers.

Chapter 8 : Recommendations for Future Directions

This dissertation focuses on the detailed structural characterization of novel channel layer and dielectric layer materials by using powerful synchrotron tools. I demonstrated the capability to design and measure the dipole inversion within high-*k* molecular layer by probing the position of heavy ions. A systematic study of thermal stability of AMOs from *in situ* X-ray scattering experiments was also carried out to show the effects from both the processing conditions (deposition temperature), and the introduction of dopants. Finally, the quantification of the local structures around the interested metal cations from XAFS study can effectively differentiate the structurally amorphous materials.

A general recommendation is to perform structural characterizations under device synthesis and/or working conditions. To this end, there are efforts to add growth chambers to several beamlines. For example, APS 33ID-E has a molecular beam epitaxy (MBE) deposition chamber for detailed layer-by-layer growth characterization. High-resolution X-ray reflectivity can probe and reveal how the new layer is deposited and interact and reorganize with the beneath substrate or newly deposited top surface. Another example, beamline 8ID-E has successfully installed a spin-coater onto a diffractometer, for *in situ* GISAXS-GIWAXS studies of transformations of as-spun solutions to films.

8.1: The Design of New High-*k* Molecules

The design of the IPAE molecule to replace the PAE in SAND is the first step in revolutionizing the organic layer. The inorganic layer has its limitation since both ZrO_2 and HfO_2 are already among the dielectric materials with the highest *k*-value. Hence, to further push the limitation, the synthesis of new organic/inorganic hybrid dielectrics will rely on the innovation of organic molecules. Here are some recommendations to continuing this project:

1) From DFT simulations of both PAE and IPAE molecules, the position of the anions strongly affects the dipole moment of each molecule. I have already introduced a concept of probability distribution of molecular configurations. For ionic molecules, the position of anions can be easily affected by both thermal fluctuation, the surface morphology of bottom oxides, and the intermolecular electrostatic interactions. Hence, a single molecular configuration from DFT simulation is not necessarily accurate for presenting and explaining the device performance. A weighted averaging based on probability distribution would be more scientific to calculate the dipole moment of a molecular layer.
2) It would be interesting to see effects of different anions. The role of anions is mainly to balance the molecular charge. However, different anions will have different radii size or effects on the molecular configuration. So, the dipole moments of the molecular layer would be different, which will reflect on the device performance.
3) The fundamental reason why there are many possible configuration and dipole moment values is the anion is ionically bonded, which gives another degree of freedom within the molecule. For molecules with covalent bonds, this is not the case since the molecule can be treated as a complete object. Hence, if a new molecule can be designed with constraints on the motion of the anions, then combined with X-ray and DFT, we can quantitatively understand the role of anions when the device is under working conditions.

8.2: Thermal Stability of AMOs doped with Secondary Anions

The fundamental goal of my research on AMOs is to understand the amorphous structure for which I have presented a variety of methods, such as directly probing the local polyhedral, or annealing the sample, tracing the structural evolvement and reexamining the original amorphous structures. However, this was limited to amorphous structure with oxygen as the only anion. The doping of anions has been poorly explored. One of a few examples is the fluorine-doped SnO (FTO), which indicates that for anion doping, a similar conductive mechanism (the formation of oxygen vacancies) can be achieved. Also, from solution processing, C, N, or H can result from carbonization of the solution and can still exist within the amorphous matrix. However, this study is limited by the sensitivity or resolution of the instruments. As an X-ray experimentalist, an effective method to quantify the role of anions inside AMOs is as interesting as the cation doping. Since hard X-rays are more sensitive to high-Z elements, X-ray absorption fine structure will be challenging to characterize low-Z anions without XAFS with soft X-rays. A possible solution is instead of directly probing the local structure, using X-ray photon emission technique to look at the energy band difference, especially the deep trapped state or localized band. These states can greatly affect the device performance. Another experiment is to perform similar crystallization experiment, and see how non-oxygen anions are incorporated into the amorphous matrix. A series of films with different secondary anions doping levels can be made through solution processing. The thermal stability will reflect on the local distortion, coordination and bonding, which can be linked to the device performance, and DFT simulations.

Appendix

Appendix A: Heating Stages

This is a user manual for the two small portable heating chambers we use for performing *in situ* synchrotron experiments. These are stored in a cabinet at APS 5BMC shown in Figure A.1. The top two shelves have the temperature control units, including controllers, connecting cables, gas tubes, pressure gauge, and transformer. The bottom shelf has the two chambers inside big black boxes. Each consists of a base and an X-ray semi-transparent dome of Be or graphite. The use of either dome requires extreme caution. Please handle each very fragile dome carefully, monitor the dome temperature, and do not over-pressurize. Due to the toxic nature of beryllium, APS has very strict rules for using the Be dome. Please consult the beam scientists before using. Also, please make sure Dr. Denis Keane or Dr. Mike Guise know if you would like to borrow the domes and use them at other beamlines.

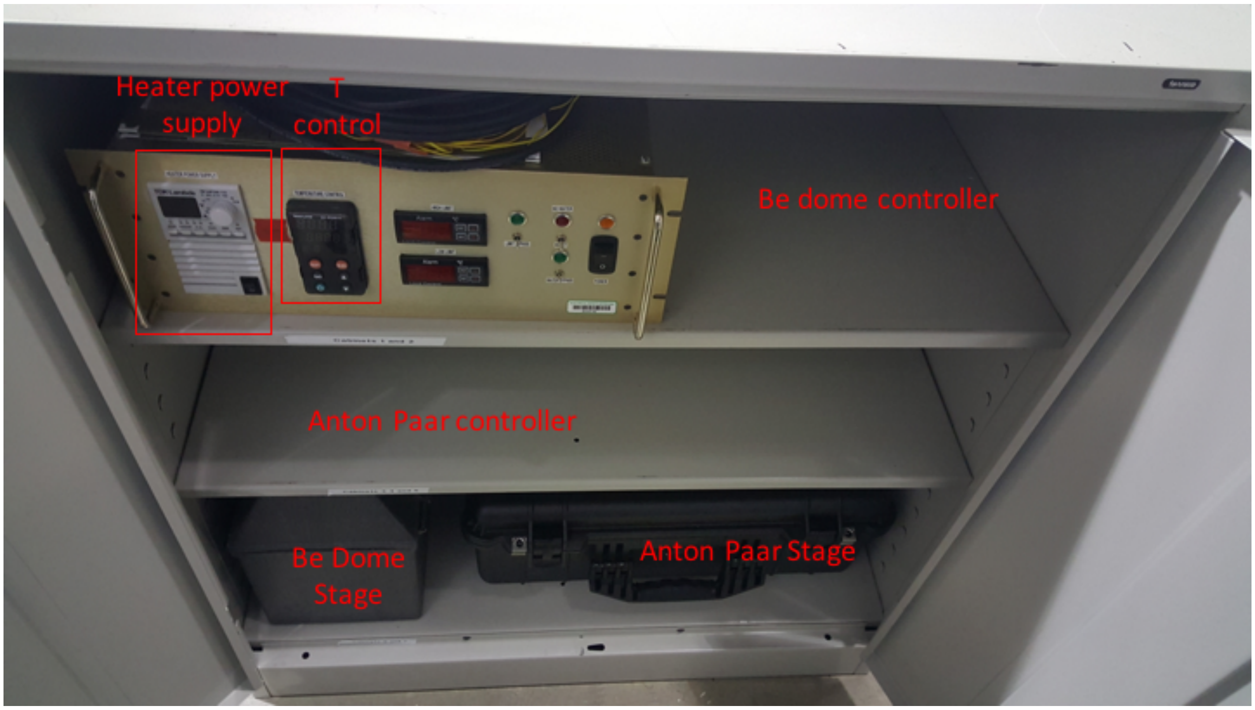

Figure A.1: The storage cabinet for both Be and graphite dome chambers. The Anton Paar controller is not included in the figure, but will be shown in Figure A.6.

Appendix A-1: Be dome heating stage

The Be dome mini chamber is customized and designed by the Bedzyk group, and has been used for many published *in situ* experiments. It can anneal samples under controlled environments, such as vacuum, oxygen or hydrogen for redox reactions. The highest temperature the dome can achieve is 600°C in vacuum condition. The Be dome temperature needs to be monitored during the heating process, and should not exceed 80°C. Typically, a fan is used to cool the dome, but if necessary, please use the water cooling channel surrounding the Al base of the dome.

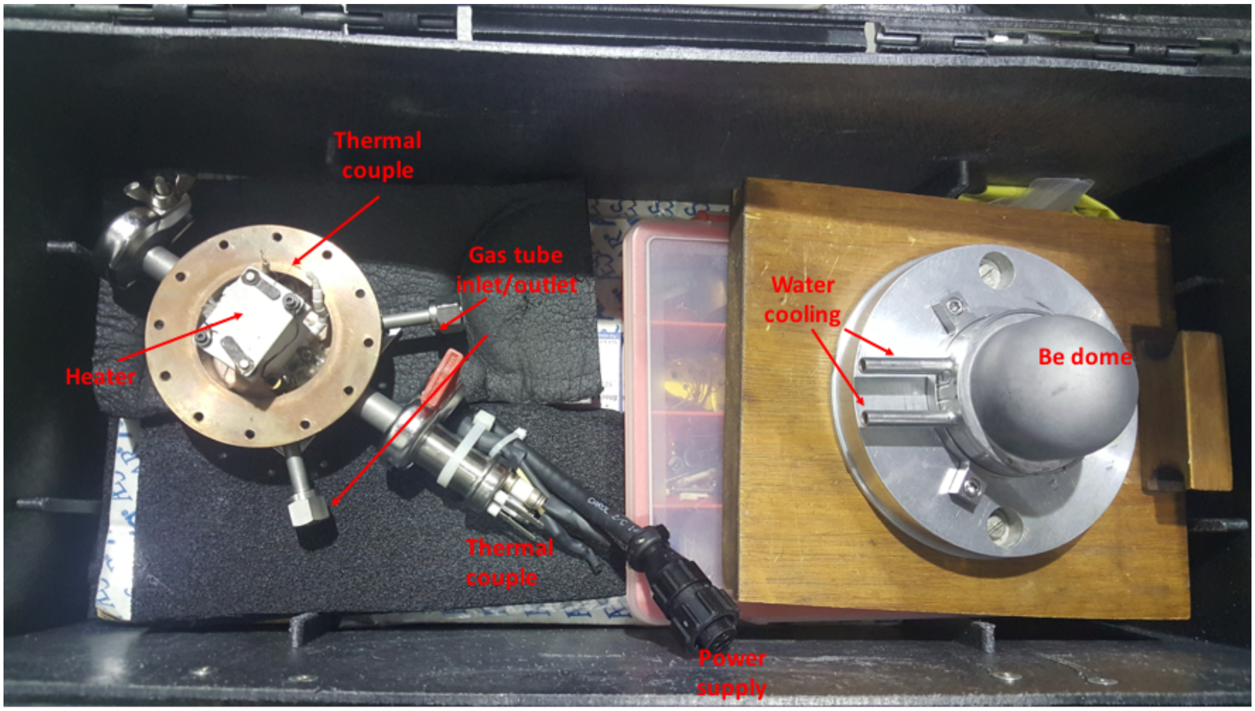

Figure A.2: The Be dome heating base (left) and beryllium-dome (right) inside the box indicated in Figure A.1. Below are the tool box and backup components of the heating stage.

Figure A.2 presents more details inside the big black box in Figure A.1. On the left is the heating stage with a pyrolytic boron nitride-coated pyrolytic graphite (PBN/PG) heater. The samples can be fixed by using the two clips to ensure good thermal contract. A thermocouple is used to monitor the samples temperature. The environment is controlled through the gas tubes shown in Figure A.2. For example, a vacuum environment can be achieved by sealing the bottom tube, and connecting the upper one to a vacuum pump. It is also possible to connect the upper one to a gas tank and leave the bottom one open or attach to a flow meter.

As shown in the Figure A.2, the Be dome can be mounted and secured by fastening the three screws to the circle of holes of the heating stage (left). The water cooling tube is also highlighted to maintain the low temperature of the Be dome at high annealing temperature. The Be dome stage has a typical Huber threaded attachment ring and base so the entire stage can be mounted on the commonly used Huber head at synchrotron. Figure A.3a shows an example setup of Be dome heating stage mounted onto a 2-circle Huber diffractometer.

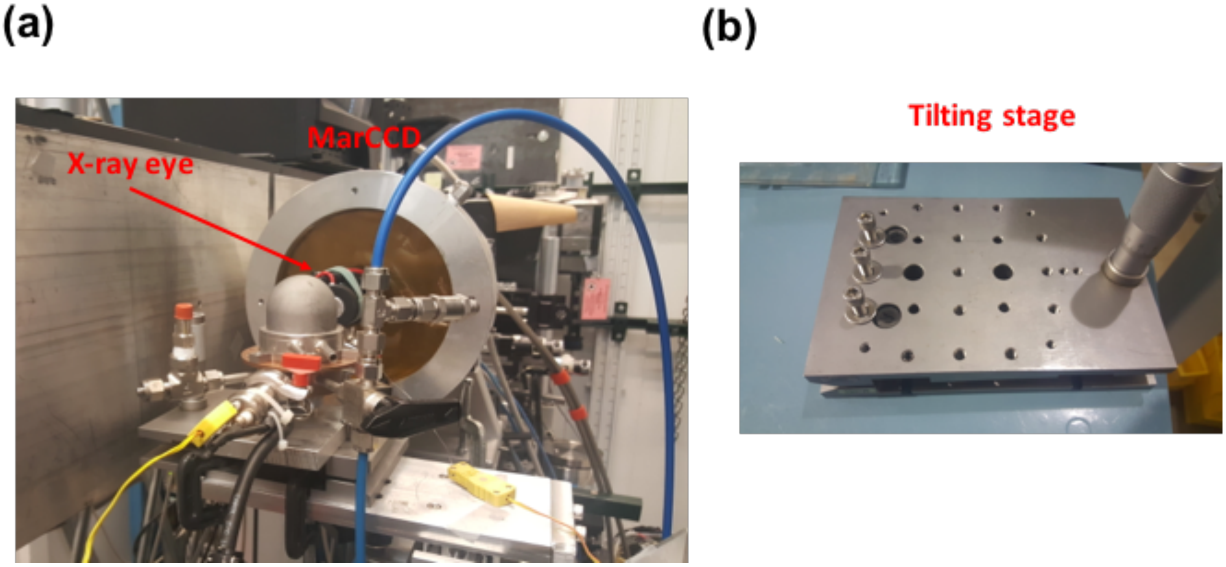

Figure A.3: (a) An example GIWAXS setup and mounting of Be dome heating stage at sector 5BMC. The 2D MarCCD detector is placed downstream to collect the scattering pattern. The X-ray eye is used for the half-beam alignment. (b) A tilt stage can be used to compensate the sample tilting (χ).

For the GIWAXS experiment, a proper alignment is necessary to determine the correct incident angle and sample position relative to the incident X-ray beam. To address this issue, an X-ray eye is implemented between the sample and the areal detector to provide both live images of X-ray beam, and a reading that is proportional to the received X-ray intensity. After the alignment, to avoid the interference with X-rays and have a clear 2D diffraction image, X-ray eye will be vertically moved down and beneath the beamstop.

Appendix A-2: Anton Paar heating stage

The DHS 1100 Anton Paar hot stage (Figure A.4) is a commercial heating unit with similar capability as the Be dome, but with a graphite dome. The most attractive features are: graphite is nontoxic, and the heating stage is capable of annealing samples up to 1100°C in air. Similar to the Be dome, the sample can be annealed in a variety of environments. The connector shown in Figure A.4b is a hose connecter together with a feed-through adapter used as an outlet for gas discharge. Other possible connectors are blind plug or pressure relief valve. The former one is provided for the measurements under vacuum, while the latter one is a safety device which opens when an overpressure of 0.35 bar relative pressure is generated in the dome.

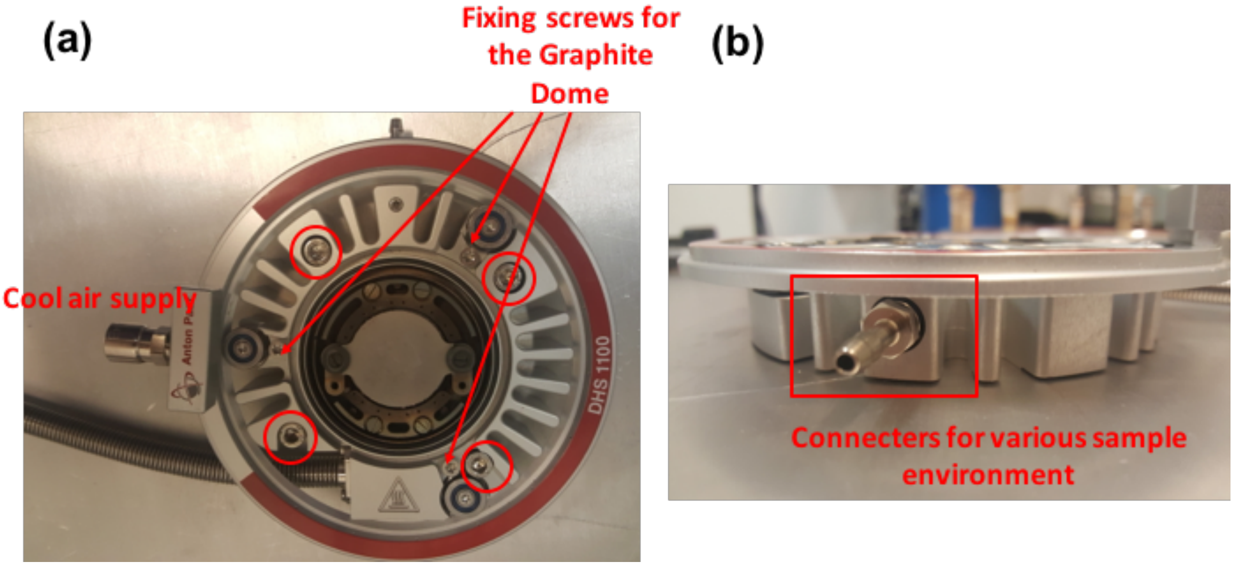

Figure A.4: (a) Top view of Anton Paar DHS 1100 domed heating stage without the graphite dome. (b) Side view of the heating stage.

Figure A.5 shows two mounting adaptors. In Figure A.5a, the black dash lines highlight a hole pattern: the corner four holes are designed to adapt to the Kappa diffractometer in sector

5IDC, and the five holes along the vertical and horizontal median lines are made for mounting on the tilt stage (Figure A.3b) used in 5BMC. While in Figure A.5b and 5c, the adapter is tailored for the typical Huber goniometer head. For both adaptors, the four screws passing through the bare holes (Figure A.4a, red circles) will fix the Anton Paar stage onto the adaptor plates, which enables the use of heating stage on the different diffractometers.

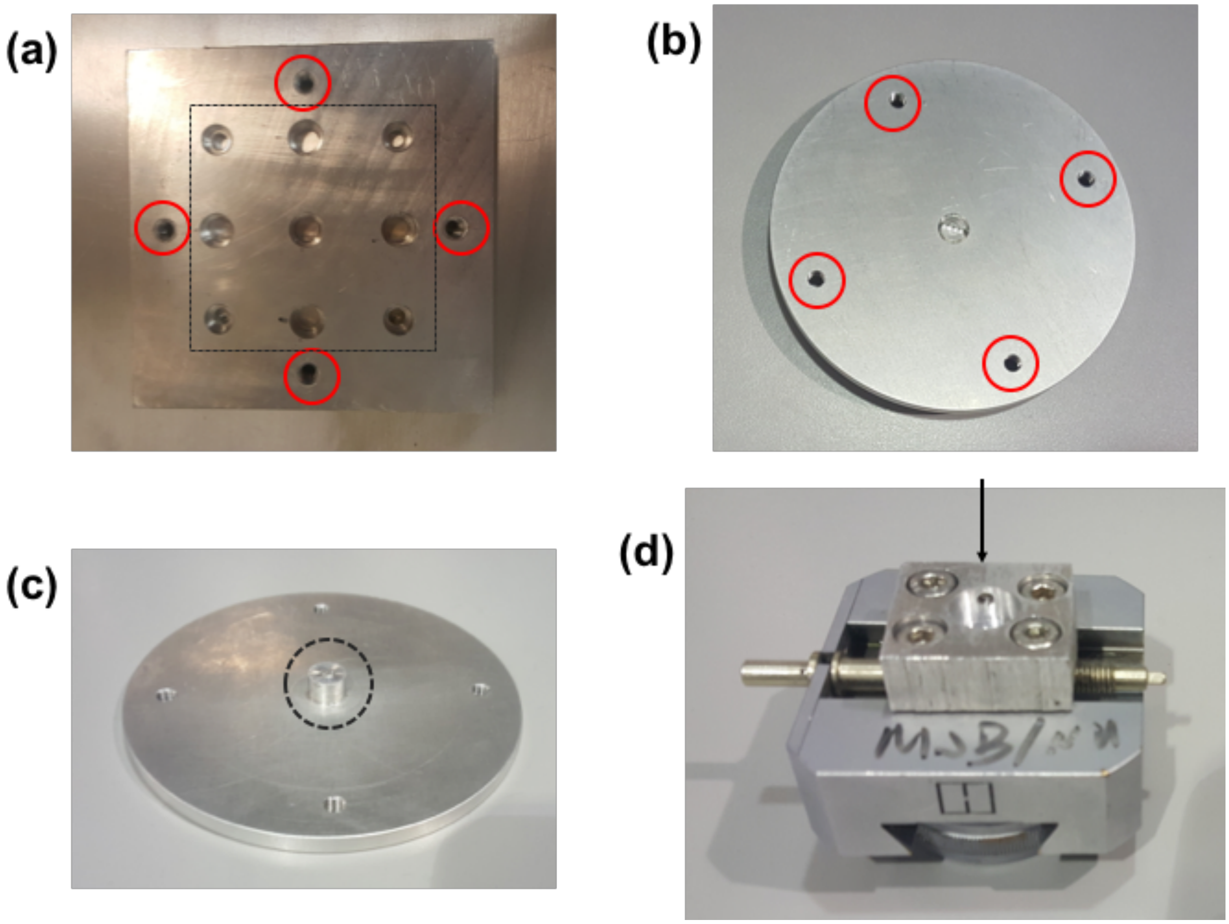

Figure A.5: (a) Adaptor plate for mounting Anton Paar onto Kappa diffractometer in 5IDC or tilting stage (Figure A.3b) used in 5BMC. The top (b) and bottom (c) views of the adaptor plate for common Huber 1003 goniometer head. The four screws in Figure A.4a (red circles) correspond to the four mounting holes (also highlighted by red circles) in (a) or (b). (d) A customized stage for doing grazing incident XAFS at sector 5BMD with Anton Paar heating stage.

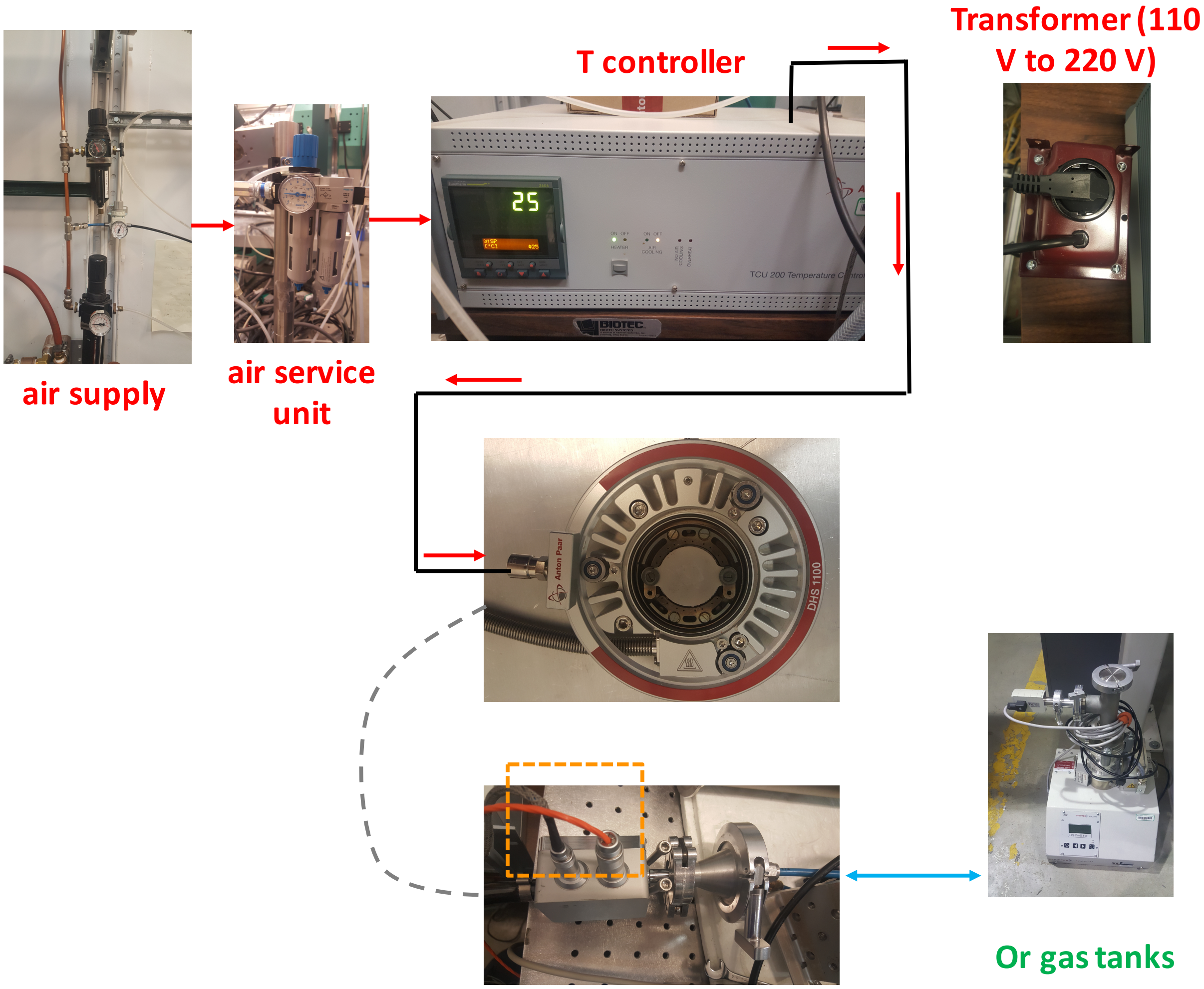

Figure A.6: The component diagram of Anton Paar heating unit.

Figure A.6 presents each component of the Anton Paar stage. The connection device of the heating stage terminates with the supply hose (grey dash line) of the DHS1100, which contains the electrical wires of the instrument and is used to evacuate the instrument or to fill it with gas (blue double arrow). The orange dash lines marked two connectors: the black wire is for thermocouple, and the orange wire is for the power supply. Both connectors are hooked up to the back of the temperature controller (Figure A.6, top). A transformer is used to convert the standard 110 V to provide the 220 V working voltage for the temperature controller. Finally, a cooling air is required to operate the stage. The red arrows indicate the flow direction. The controller automatically stops flowing cooling air when the sample temperature is below 200°C, and starts blowing air to the graphite dome once the temperature is above.

A few things to note:

1. The cooling air must be free of oil and dust. The pressure should be set between 2 and 4 bar relative to the atmospheric pressure ("air service unit" in Figure A.6).
2. The sample can be fixed on the sample holder with springs. The springs are supplied in the accessory box, and can be placed in the small bore holes around the sample holder. There are 5 and 10 mm length springs to accommodate the samples with different size. The springs may start to lose tension after 700°C.
3. The graphite dome itself can generate diffraction peaks, which may interfere with the diffraction measurements.
4. Inside DHS 1100 dome, a vacuum of $< 6\times10^{-1}$ mbar can be achieved with a standard vacuum pump with 4.8 m^3/h capacity.

Reference:

[1] B.M. Al-Hashimi, System-on-chip: next generation electronics, IET2006.

[2] A. Facchetti, T. Marks, Transparent electronics: from synthesis to applications, John Wiley & Sons2010.

[3] M.A. Leenen, V. Arning, H. Thiem, J. Steiger, R. Anselmann, Printable electronics: flexibility for the future, physica status solidi (a), 206 (2009) 588-597.

[4] W.S. Wong, A. Salleo, Flexible electronics: materials and applications, Springer Science & Business Media2009.

[5] H. Hosono, D.C. Paine, Handbook of transparent conductors, Springer Science & Business Media2010.

[6] Y.G. Ha, K. Everaerts, M.C. Hersam, T.J. Marks, Hybrid gate dielectric materials for unconventional electronic circuitry, Acc Chem Res, 47 (2014) 1019-1028.

[7] J.E. Medvedeva, D.B. Buchholz, R.P. Chang, Recent Advances in Understanding the Structure and Properties of Amorphous Oxide Semiconductors, Advanced Electronic Materials, DOI (2017).

[8] K. Everaerts, J.D. Emery, D. Jariwala, H.J. Karmel, V.K. Sangwan, P.L. Prabhumirashi, M.L. Geier, J.J. McMorrow, M.J. Bedzyk, A. Facchetti, M.C. Hersam, T.J. Marks, Ambient-processable high capacitance hafnia-organic self-assembled nanodielectrics, J Am Chem Soc, 135 (2013) 8926-8939.

[9] Y.G. Ha, J.D. Emery, M.J. Bedzyk, H. Usta, A. Facchetti, T.J. Marks, Solution-deposited organic-inorganic hybrid multilayer gate dielectrics. Design, synthesis, microstructures, and electrical properties with thin-film transistors, J Am Chem Soc, 133 (2011) 10239-10250.

[10] X. Yu, T.J. Marks, A. Facchetti, Metal oxides for optoelectronic applications, Nat Mater, 15 (2016) 383-396.

[11] T. Kamiya, H. Hosono, Material characteristics and applications of transparent amorphous oxide semiconductors, NPG Asia Materials, 2 (2010) 15-22.

[12] The Transistor, Nobelprize.org. , 2014.

[13] J.M. Early, Out to Murray Hill to play: an early history of transistors, IEEE Transactions on Electron Devices, 48 (2001) 2468-2472.

[14] J.-H. Lee, D.N. Liu, S.-T. Wu, Introduction to flat panel displays, John Wiley & Sons2008.

[15] S.M. Sze, Semiconductor devices: physics and technology, John Wiley & Sons2008.

[16] S.A. DiBenedetto, A. Facchetti, M.A. Ratner, T.J. Marks, Molecular Self-Assembled Monolayers and Multilayers for Organic and Unconventional Inorganic Thin-Film Transistor Applications, Advanced Materials, 21 (2009) 1407-1433.

[17] R.P. Ortiz, A.F. Facchetti, T.J. Marks, High-k Organic, Inorganic, and Hybrid Dielectrics for Low-Voltage Organic Field-Effect Transistors.pdf, Chemical Reviews, 110 (2010) 205-239.

[18] Z. Wu, D. Ma, Recent advances in white organic light-emitting diodes, Materials Science and Engineering: R: Reports, 107 (2016) 1-42.

[19] H. Hosono, J. Kim, Y. Toda, T. Kamiya, S. Watanabe, Transparent amorphous oxide semiconductors for organic electronics: Application to inverted OLEDs, Proceedings of the National Academy of Sciences, DOI (2016) 201617186.

[20] F. Schwierz, Graphene transistors, Nature nanotechnology, 5 (2010) 487-496.

[21] R.H. Baughman, A.A. Zakhidov, W.A. De Heer, Carbon nanotubes--the route toward applications, science, 297 (2002) 787-792.

[22] A.D. Printz, D.J. Lipomi, Competition between deformability and charge transport in semiconducting polymers for flexible and stretchable electronics, Applied Physics Reviews, 3 (2016) 021302.

[23] J. Robertson, High dielectric constant gate oxides for metal oxide Si transistors, Reports on progress in Physics, 69 (2006) 327-396.

[24] J. Robertson, High dielectric constant oxides, The European physical journal applied physics, 28 (2004) 265-291.

[25] R. Street, Technology and applications of amorphous silicon, Springer Science & Business Media2013.

[26] K. Nomura, H. Ohta, A. Takagi, T. Kamiya, M. Hirano, H. Hosono, Room-temperature fabrication of transparent flexible thin-film transistors using amorphous oxide semiconductors, Nature, 432 (2004) 488-492.

[27] B. Radisavljevic, A. Radenovic, J. Brivio, i.V. Giacometti, A. Kis, Single-layer MoS2 transistors, Nature nanotechnology, 6 (2011) 147-150.

[28] L. Li, Y. Yu, G.J. Ye, Q. Ge, X. Ou, H. Wu, D. Feng, X.H. Chen, Y. Zhang, Black phosphorus field-effect transistors, Nature nanotechnology, 9 (2014) 372-377.

[29] M. Lorenz, M.R. Rao, T. Venkatesan, E. Fortunato, P. Barquinha, R. Branquinho, D. Salgueiro, R. Martins, E. Carlos, A. Liu, The 2016 oxide electronic materials and oxide interfaces roadmap, Journal of Physics D: Applied Physics, 49 (2016) 433001.

[30] E. Fortunato, P. Barquinha, R. Martins, Oxide Semiconductor Thin‐Film Transistors: A Review of Recent Advances, Advanced materials, 24 (2012) 2945-2986.

[31] T. Kamiya, K. Nomura, H. Hosono, Present status of amorphous In–Ga–Zn–O thin-film

transistors, Science and Technology of Advanced Materials, 11 (2010) 044305.

[32] J.W. Hennek, J. Smith, A. Yan, M.G. Kim, W. Zhao, V.P. Dravid, A. Facchetti, T.J. Marks, Oxygen "getter" effects on microstructure and carrier transport in low temperature combustion-processed a-InXZnO (X = Ga, Sc, Y, La) transistors, J Am Chem Soc, 135 (2013) 10729-10741.

[33] D.B. Buchholz, L. Zeng, M.J. Bedzyk, R.P. Chang, Differences between amorphous indium oxide thin films, Progress in Natural Science: Materials International, 23 (2013) 475-480.

[34] N. Zhou, D.B. Buchholz, G. Zhu, X. Yu, H. Lin, A. Facchetti, T.J. Marks, R.P. Chang, Ultraflexible Polymer Solar Cells Using Amorphous Zinc− Indium− Tin Oxide Transparent Electrodes, Advanced Materials, 26 (2014) 1098-1104.

[35] M.-G. Kim, M.G. Kanatzidis, A. Facchetti, T.J. Marks, Low-temperature fabrication of high-performance metal oxide thin-film electronics via combustion processing, Nature materials, 10 (2011) 382.

[36] P. Heremans, A.K. Tripathi, A. de Jamblinne de Meux, E.C. Smits, B. Hou, G. Pourtois, G.H. Gelinck, Mechanical and Electronic Properties of Thin‐Film Transistors on Plastic, and Their Integration in Flexible Electronic Applications, Advanced Materials, 28 (2016) 4266-4282.

[37] K. Everaerts, L. Zeng, J.W. Hennek, D.I. Camacho, D. Jariwala, M.J. Bedzyk, M.C. Hersam, T.J. Marks, Printed indium gallium zinc oxide transistors. Self-assembled nanodielectric effects on low-temperature combustion growth and carrier mobility, ACS applied materials & interfaces, 5 (2013) 11884-11893.

[38] D.E. Proffit, Q. Ma, D.B. Buchholz, R.P.H. Chang, M.J. Bedzyk, T.O. Mason, Structural and Physical Property Studies of Amorphous Zn–In–Sn–O Thin Films, Journal of the American

Ceramic Society, 95 (2012) 3657-3664.

[39] C.Y. Wang, L. Kirste, F. Morales, J. Mánuel, C. Röhlig, K. Köhler, V. Cimalla, R. Garcia, O. Ambacher, Growth mechanism and electronic properties of epitaxial In2O3 films on sapphire, Journal of Applied Physics, 110 (2011) 093712.

[40] S.Z. Karazhanov, P. Ravindran, P. Vajeeston, A. Ulyashin, T. Finstad, H. Fjellvåg, Phase stability, electronic structure, and optical properties of indium oxide polytypes, Physical Review B, 76 (2007) 075129.

[41] C.Y. Wang, Y. Dai, J. Pezoldt, B. Lu, T. Kups, V. Cimalla, O. Ambacher, Phase stabilization and phonon properties of single crystalline rhombohedral indium oxide, Crystal growth and Design, 8 (2008) 1257-1260.

[42] B. Yaglioglu, H.-Y. Yeom, D.C. Paine, Crystallization of amorphous In 2 O 3–10 wt% ZnO thin films annealed in air, Applied Physics Letters, 86 (2005) 261908.

[43] A. Walsh, C.R.A. Catlow, Structure, stability and work functions of the low index surfaces of pure indium oxide and Sn-doped indium oxide (ITO) from density functional theory, Journal of Materials Chemistry, 20 (2010) 10438-10444.

[44] A. Walsh, J.L. Da Silva, S.-H. Wei, Multi-component transparent conducting oxides: progress in materials modelling, Journal of Physics: Condensed Matter, 23 (2011) 334210.

[45] M.P. Taylor, D.W. Readey, C.W. Teplin, M.F. van Hest, J.L. Alleman, M.S. Dabney, L.M. Gedvilas, B.M. Keyes, B. To, J.D. Perkins, The electrical, optical and structural properties of InxZn1− xOy (0⩽ x⩽ 1) thin films by combinatorial techniques, Measurement Science and Technology, 16 (2004) 90.

[46] C.A. Hoel, T.O. Mason, J.-F. Gaillard, K.R. Poeppelmeier, Transparent conducting oxides

in the ZnO-In2O3-SnO2 system, Chemistry of Materials, 22 (2010) 3569-3579.

[47] S.P. Harvey, K.R. Poeppelmeier, T.O. Mason, Subsolidus phase relationships in the ZnO–In2O3–SnO2 system, Journal of the American Ceramic Society, 91 (2008) 3683-3689.

[48] D.E. Proffit, T. Philippe, J.D. Emery, Q. Ma, B.D. Buchholz, P.W. Voorhees, M.J. Bedzyk, R.P.H. Chang, T.O. Mason, Thermal stability of amorphous Zn-In-Sn-O films, Journal of Electroceramics, 34 (2014) 167-174.

[49] M.M. Moghadam, R. Li, D.B. Buchholz, Q. Li, P.W. Voorhees, V.P. Dravid, In Situ Crystallization and Morphological Evolution in Multicomponent Indium Oxide Thin Films, Crystal Growth & Design, 17 (2017) 1396-1403.

[50] L.J. van der Pauw, A method of measuring specific resistivity and Hall effect of discs of arbitrary shapes, Philips research reports, 13 (1958) 1-9.

[51] A. Murat, A.U. Adler, T.O. Mason, J.E. Medvedeva, Carrier generation in multicomponent wide-bandgap oxides: InGaZnO4, Journal of the American Chemical Society, 135 (2013) 5685-5692.

[52] J. Als-Nielsen, D. McMorrow, Elements of Modern X-ray Physics, Wiley2011.

[53] B.D. Cullity, S.R. Stock, Elements of X-ray Diffraction, Prentice Hall2001.

[54] B.E. Warren, X-ray Diffraction, Courier Corporation1969.

[55] G. Bunker, Introduction to XAFS: a practical guide to X-ray absorption fine structure spectroscopy, Cambridge University Press2010.

[56] C.D. Wagner, C.J. Powell, J.W. Allison, J.R. Rumble, NIST X-Ray Photoelectron Spectroscopy Database 1, Version 2, Nat'l Std. Ref. Data Series (NIST NSRDS)-, DOI (1997).

[57] H.C. Liao, P. Guo, C.P. Hsu, M. Lin, B. Wang, L. Zeng, W. Huang, C.M.M. Soe, W.F. Su,

M.J. Bedzyk, Enhanced Efficiency of Hot‐Cast Large‐Area Planar Perovskite Solar Cells/Modules Having Controlled Chloride Incorporation, Advanced Energy Materials, 7 (2017).

[58] J. Zegenhagen, Surface structure determination with X-ray standing waves, Surface Science Reports, 18 (1993) 202-271.

[59] M.J. Bedzyk, New Trends in X-ray Standing Waves, Nuclear Instruments & Methods in Physics Research A266 (1988) 679-683.

[60] M.J. Bedzyk, J.A. Libera, X-Ray Standing Wave in Multilayers, in: J. Zegenhagen, A. Kazimirov (Eds.) Synchrotron Radiation Techniques and Applications: The X-Ray Standing Wave Technique: Principles and Applications, World Scientific2013.

[61] J.A. Golovchenko, J.R. Patel, D.R. Kaplan, P.L. Cowan, M.J. Bedzyk, Solution to the Surface Registration Problem Using X-Ray Standing Waves, Phys Rev Lett, 49 (1982) 560-563.

[62] M.J. Bedzyk, D. Bilderback, J. White, H.D. Abruna, M.G. Bommarito, Probing Electrochemical Interfaces with X-ray Standing Waves, Journal of Physical Chemistry, 90 (1986) 4926-4928.

[63] M.J. Bedzyk, D.H. Bilderback, G.M. Bommarito, M. Caffrey, J.S. Schildkraut, X-Ray Standing Waves - a Molecular Yardstick for Biological-Membranes, Science, 241 (1988) 1788-1791.

[64] W. Lin, T.L. Lee, P.F. Lyman, J. Lee, M.J. Bedzyk, T.J. Marks, Atomic resolution X-ray standing wave microstructural characterization of NLO-active self-assembled chromophoric superlattices., Journal of the American Chemical Society, 119 (1997) 2205-2211.

[65] J.A. Libera, R.W. Gurney, C. Schwartz, H. Jin, T.L. Lee, S.T. Nguyen, J.T. Hupp, M.J. Bedzyk, Comparative X-ray standing wave analysis of metal-phosphonate multilayer films of

dodecane and porphyrin molecular square, J Phys Chem B, 109 (2005) 1441-1450.

[66] J.A. Libera, H. Cheng, M.O. de la Cruz, M.J. Bedzyk, Direct observation of cations and polynucleotides explains polyion adsorption to like-charged surfaces, J Phys Chem B, 109 (2005) 23001-23007.

[67] M. Born, E. Wolf, Principles of Optics, seventh expanded edition, Cambridge, England, DOI (1999).

[68] L.G. Parratt, Surface Studies of Solids by Total Reflection of X-Rays, Physical Review, 95 (1954) 359-369.

[69] B.K. Sharma, J.-H. Ahn, Flexible and Stretchable Oxide Electronics, Advanced Electronic Materials, 2 (2016) 1600105.

[70] G. Wang, N. Persson, P.-H. Chu, N. Kleinhenz, B. Fu, M. Chang, N. Deb, Y. Mao, H. Wang, M.A. Grover, Microfluidic Crystal Engineering of π-Conjugated Polymers, ACS nano, 9 (2015) 8220-8230.

[71] J.A. Rogers, T. Someya, Y. Huang, Materials and mechanics for stretchable electronics, Science, 327 (2010) 1603-1607.

[72] M.L. Hammock, A. Chortos, B.C. Tee, J.B. Tok, Z. Bao, 25th anniversary article: The evolution of electronic skin (e-skin): a brief history, design considerations, and recent progress, Adv Mater, 25 (2013) 5997-6038.

[73] J. Zhang, X. Liu, G. Neri, N. Pinna, Nanostructured Materials for Room-Temperature Gas Sensors, Adv Mater, 28 (2016) 795-831.

[74] S.G. Bucella, A. Luzio, E. Gann, L. Thomsen, C.R. McNeill, G. Pace, A. Perinot, Z. Chen, A. Facchetti, M. Caironi, Macroscopic and high-throughput printing of aligned nanostructured

polymer semiconductors for MHz large-area electronics, Nat Commun, 6 (2015) 8394.

[75] P.H. Chu, G. Wang, B. Fu, D. Choi, J.O. Park, M. Srinivasarao, E. Reichmanis, Synergistic Effect of Regioregular and Regiorandom Poly (3 - hexylthiophene) Blends for High Performance Flexible Organic Field Effect Transistors, Advanced Electronic Materials, 2 (2016).

[76] J.M. Adhikari, M.R. Gadinski, Q. Li, K.G. Sun, M.A. Reyes - Martinez, E. Iagodkine, A.L. Briseno, T.N. Jackson, Q. Wang, E.D. Gomez, Controlling Chain Conformations of High - k Fluoropolymer Dielectrics to Enhance Charge Mobilities in Rubrene Single - Crystal Field - Effect Transistors, Advanced Materials, 28 (2016) 10095-10102.

[77] H.N. Arnold, C.D. Cress, J.J. McMorrow, S.W. Schmucker, V.K. Sangwan, L. Jaber-Ansari, R. Kumar, K.P. Puntambekar, K.A. Luck, T.J. Marks, Tunable Radiation Response in Hybrid Organic–Inorganic Gate Dielectrics for Low-Voltage Graphene Electronics, ACS applied materials & interfaces, 8 (2016) 5058-5064.

[78] S. Balendhran, J. Deng, J.Z. Ou, S. Walia, J. Scott, J. Tang, K.L. Wang, M.R. Field, S. Russo, S. Zhuiykov, Enhanced charge carrier mobility in two - dimensional high dielectric molybdenum oxide, Advanced Materials, 25 (2013) 109-114.

[79] S.A. DiBenedetto, A. Facchetti, M.A. Ratner, T.J. Marks, Molecular Self - Assembled Monolayers and Multilayers for Organic and Unconventional Inorganic Thin - Film Transistor Applications, Advanced materials, 21 (2009) 1407-1433.

[80] S. Casalini, C.A. Bortolotti, F. Leonardi, F. Biscarini, Self-assembled monolayers in organic electronics, Chemical Society Reviews, DOI (2016).

[81] B. Wang, G. Di Carlo, R. Turrisi, L. Zeng, K. Stallings, M. Bedzyk, L. Beverina, T. Marks, A. Facchetti, Dipole Moment Inversion Effects in Self-Assembled Nanodielectrics for Organic

Thin Film Transistors, Submitted to Chemistry of Materials. (2017).

[82] J.F. Martinez Hardigree, H.E. Katz, Through thick and thin: tuning the threshold voltage in organic field-effect transistors, Acc Chem Res, 47 (2014) 1369-1377.

[83] S.K. Possanner, K. Zojer, P. Pacher, E. Zojer, F. Schürrer, Threshold Voltage Shifts in Organic Thin-Film Transistors Due to Self-Assembled Monolayers at the Dielectric Surface, Advanced Functional Materials, 19 (2009) 958-967.

[84] S. Vasudevan, N. Kapur, T. He, M. Neurock, J.M. Tour, A.W. Ghosh, Controlling transistor threshold voltages using molecular dipoles, Journal of Applied Physics, 105 (2009) 093703.

[85] K.P. Pernstich, S. Haas, D. Oberhoff, C. Goldmann, D.J. Gundlach, B. Batlogg, A.N. Rashid, G. Schitter, Threshold voltage shift in organic field effect transistors by dipole monolayers on the gate insulator, Journal of Applied Physics, 96 (2004) 6431-6438.

[86] C.K. Song, K.A. Luck, N. Zhou, L. Zeng, H.M. Heitzer, E.F. Manley, S. Goldman, L.X. Chen, M.A. Ratner, M.J. Bedzyk, “Supersaturated” Self-Assembled Charge-Selective Interfacial Layers for Organic Solar Cells, Journal of the American Chemical Society, 136 (2014) 17762-17773.

[87] M. Halik, H. Klauk, U. Zschieschang, G. Schmid, C. Dehm, M. Schütz, S. Maisch, F. Effenberger, M. Brunnbauer, F. Stellacci, Low-voltage organic transistors with an amorphous molecular gate dielectric, Nature, 431 (2004) 963-966.

[88] M. de Pauli, U. Zschieschang, I.D. Barcelos, H. Klauk, A. Malachias, Tailoring the dielectric layer structure for enhanced carrier mobility in organic transistors: The use of hybrid inorganic/organic multilayer dielectrics, Advanced Electronic Materials, 2 (2016).

[89] M. Salinas, C.M. Jager, A.Y. Amin, P.O. Dral, T. Meyer-Friedrichsen, A. Hirsch, T. Clark,

M. Halik, The relationship between threshold voltage and dipolar character of self-assembled monolayers in organic thin-film transistors, J Am Chem Soc, 134 (2012) 12648-12652.

[90] A. Jedaa, M. Salinas, C.M. Jäger, T. Clark, A. Ebel, A. Hirsch, M. Halik, Mixed self-assembled monolayer of molecules with dipolar and acceptor character—Influence on hysteresis and threshold voltage in organic thin-film transistors, Applied Physics Letters, 100 (2012) 36.

[91] T. Abu‐Husein, S. Schuster, D.A. Egger, M. Kind, T. Santowski, A. Wiesner, R. Chiechi, E. Zojer, A. Terfort, M. Zharnikov, The Effects of Embedded Dipoles in Aromatic Self‐Assembled Monolayers, Advanced Functional Materials, 25 (2015) 3943-3957.

[92] J. Chakhalian, J.M. Rondinelli, J. Liu, B.A. Gray, M. Kareev, E.J. Moon, N. Prasai, J.L. Cohn, M. Varela, I.C. Tung, M.J. Bedzyk, S.G. Altendorf, F. Strigari, B. Dabrowski, L.H. Tjeng, P.J. Ryan, J.W. Freeland, Asymmetric Orbital-Lattice Interactions in Ultrathin Correlated Oxide Films, Phys Rev Lett, 107 (2011).

[93] A. Nelson, Co-refinement of multiple-contrast neutron/X-ray reflectivity data usingMOTOFIT, Journal of Applied Crystallography, 39 (2006) 273-276.

[94] G. Kresse, J. Furthmüller, Efficient iterative schemes for ab initio total-energy calculations using a plane-wave basis set, Physical review B, 54 (1996) 11169.

[95] G. Kresse, J. Furthmüller, Efficiency of ab-initio total energy calculations for metals and semiconductors using a plane-wave basis set, Computational Materials Science, 6 (1996) 15-50.

[96] C.K. Song, A.C. White, L. Zeng, B.J. Leever, M.D. Clark, J.D. Emery, S.J. Lou, A. Timalsina, L.X. Chen, M.J. Bedzyk, Systematic investigation of organic photovoltaic cell charge injection/performance modulation by dipolar organosilane interfacial layers, ACS applied

materials & interfaces, 5 (2013) 9224-9240.

[97] D.S. Ginley, C. Bright, Transparent conducting oxides, Mrs Bulletin, 25 (2000) 15-18.

[98] S. Lee, S. Jeon, R. Chaji, A. Nathan, Transparent semiconducting oxide technology for touch free interactive flexible displays, Proceedings of the IEEE, 103 (2015) 644-664.

[99] J.F. Wager, B. Yeh, R.L. Hoffman, D.A. Keszler, An amorphous oxide semiconductor thin-film transistor route to oxide electronics, Current Opinion in Solid State and Materials Science, 18 (2014) 53-61.

[100] K. Banger, Y. Yamashita, K. Mori, R. Peterson, T. Leedham, J. Rickard, H. Sirringhaus, Low-temperature, high-performance solution-processed metal oxide thin-film transistors formed by a ‘sol–gel on chip’process, Nature materials, 10 (2011) 45-50.

[101] Y.H. Hwang, J.-S. Seo, J.M. Yun, H. Park, S. Yang, S.-H.K. Park, B.-S. Bae, An ‘aqueous route’for the fabrication of low-temperature-processable oxide flexible transparent thin-film transistors on plastic substrates, NPG Asia Materials, 5 (2013) e45.

[102] Y. Kumaresan, Y. Pak, N. Lim, M.-J. Park, S.-M. Yoon, H.-M. Youn, H. Lee, B.H. Lee, G.Y. Jung, Highly Bendable In-Ga-ZnO Thin Film Transistors by Using a Thermally Stable Organic Dielectric Layer, Scientific reports, 6 (2016) 37764.

[103] J. Smith, L. Zeng, R. Khanal, K. Stallings, A. Facchetti, J.E. Medvedeva, M.J. Bedzyk, T.J. Marks, Cation Size Effects on the Electronic and Structural Properties of Solution‐Processed In‐X‐O Thin Films, Advanced Electronic Materials, 1 (2015).

[104] W. Huang, L. Zeng, X. Yu, P. Guo, B. Wang, Q. Ma, R.P. Chang, J. Yu, M.J. Bedzyk, T.J. Marks, Metal Oxide Transistors via Polyethylenimine Doping of the Channel Layer: Interplay of Doping, Microstructure, and Charge Transport, Advanced Functional Materials, 26 (2016)

6179-6187.

[105] X. Yu, L. Zeng, N. Zhou, P. Guo, F. Shi, D.B. Buchholz, Q. Ma, J. Yu, V.P. Dravid, R.P. Chang, Ultra‐Flexible, "Invisible" Thin‐Film Transistors Enabled by Amorphous Metal Oxide/Polymer Channel Layer Blends, Advanced Materials, 27 (2015) 2390-2399.

[106] A.P.P. Correia, P.M.C. Barquinha, J.C. da Palma Goes, A Second-Order ΣΔ ADC Using Sputtered IGZO TFTs, Springer2015.

[107] G. Liu, A. Liu, H. Zhu, B. Shin, E. Fortunato, R. Martins, Y. Wang, F. Shan, Low‐Temperature, Nontoxic Water‐Induced Metal‐Oxide Thin Films and Their Application in Thin‐Film Transistors, Advanced Functional Materials, 25 (2015) 2564-2572.

[108] A. Klein, Transparent conducting oxides: Electronic structure–property relationship from photoelectron spectroscopy with in situ sample preparation, Journal of the American Ceramic Society, 96 (2013) 331-345.

[109] R. Khanal, D.B. Buchholz, R.P. Chang, J.E. Medvedeva, Composition-dependent structural and transport properties of amorphous transparent conducting oxides, Physical Review B, 91 (2015) 205203.

[110] S.L. Moffitt, Q. Zhu, Q. Ma, A.F. Falduto, D.B. Buchholz, R.P.H. Chang, T.O. Mason, J.E. Medvedeva, T.J. Marks, M.J. Bedzyk, Probing the Unique Role of Gallium in Amorphous Oxide Semiconductors through Structure–Property Relationships, Advanced Electronic Materials, DOI 10.1002/aelm.201700189(2017).

[111] D.C. Paine, T. Whitson, D. Janiac, R. Beresford, C.O. Yang, B. Lewis, A study of low temperature crystallization of amorphous thin film indium-tin-oxide, Journal of Applied Physics, 85 (1999) 8445-8450.

[112] M. Quaas, H. Steffen, R. Hippler, H. Wulff, Investigation of diffusion and crystallization processes in thin ITO films by temperature and time resolved grazing incidence X-ray diffractometry, Surf Sci, 540 (2003) 337-342.

[113] P.K. Song, H. Akao, M. Kamei, Y. Shigesato, I. Yasui, Preparation and crystallization of tin-doped and undoped amorphous indium oxide films deposited by sputtering, Japanese journal of applied physics, 38 (1999) 5224.

[114] F.O. Adurodija, L. Semple, R. Brüning, Crystallization process and electro-optical properties of In2O3 and ITO thin films, Journal of materials science, 41 (2006) 7096-7102.

[115] S. Muranaka, Crystallization of amorphous In2O3 films during film growth, Japanese journal of applied physics, 30 (1991) L2062.

[116] J. Ilavsky, Nika: software for two-dimensional data reduction, Journal of Applied Crystallography, 45 (2012) 324-328.

[117] L.E. Alexander, X-ray diffraction methods in polymer science, Wiley1969.

[118] W. Ruland, X-ray determination of crystallinity and diffuse disorder scattering, Acta Crystallographica, 14 (1961) 1180-1185.

[119] D.-M. Smilgies, Scherrer grain-size analysis adapted to grazing-incidence scattering with area detectors, Journal of Applied Crystallography, 42 (2009) 1030-1034.

[120] D.-M. Smilgies, Scherrer grain-size analysis adapted to grazing-incidence scattering with area detectors. Erratum, Journal of Applied Crystallography, 46 (2013) 286-286.

[121] M. Avrami, Kinetics of phase change I - General theory, J Chem Phys, 7 (1939) 1103-1112.

[122] M. Avrami, Granulation, Phase Change, and Microstructure - Kinetics of Phase Change.

III, J Chem Phys, 9 (1941) 177-184.

[123] E. Pang, N. Vo, T. Philippe, P. Voorhees, Modeling interface-controlled phase transformation kinetics in thin films, Journal of Applied Physics, 117 (2015) 175304.

[124] J.A. Sethian, Level set methods and fast marching methods: evolving interfaces in computational geometry, fluid mechanics, computer vision, and materials science, Cambridge university press1999.

[125] S. Osher, R. Fedkiw, Level set methods and dynamic implicit surfaces, Springer Science & Business Media2006.

[126] C. Ganpule, A. Roytburd, V. Nagarajan, B. Hill, S. Ogale, E. Williams, R. Ramesh, J. Scott, Polarization relaxation kinetics and 180 domain wall dynamics in ferroelectric thin films, Physical Review B, 65 (2001) 014101.

[127] M. Moghadam, E. Pang, T. Philippe, P. Voorhees, Simulation of phase transformation kinetics in thin films under a constant nucleation rate, Thin Solid Films, 612 (2016) 437-444.

[128] M. Moghadam, P. Voorhees, Thin film phase transformation kinetics: From theory to experiment, Scripta Materialia, 124 (2016) 164-168.

[129] M.M. Moghadam, P.W. Voorhees, Level-Set Method Simulation of Faceted Phase Transformation via Anisotropic Growth, Computational Materials Science, Under Review (2017).

[130] G. Russo, P. Smereka, A level-set method for the evolution of faceted crystals, SIAM Journal on Scientific Computing, 21 (2000) 2073-2095.

[131] B. Yaglioglu, H.-Y. Yeom, D.C. Paine, Crystallization of amorphous In2O3–10wt% ZnO thin films annealed in air, Applied Physics Letters, 86 (2005) 261908.

[132] B. Ravel, M. Newville, ATHENA, ARTEMIS, HEPHAESTUS: data analysis for X-ray absorption spectroscopy using IFEFFIT, Journal of Synchrotron Radiation, 12 (2005) 537-541.

[133] Q. Jia, T.M. McCleskey, A. Burrell, Y. Lin, G. Collis, H. Wang, A. Li, S. Foltyn, Polymer-assisted deposition of metal-oxide films, Nature materials, 3 (2004) 529.

[134] A.K. Burrell, T.M. McCleskey, Q. Jia, Polymer assisted deposition, Chemical Communications, DOI (2008) 1271-1277.

[135] G. Zou, J. Zhao, H. Luo, T. McCleskey, A. Burrell, Q. Jia, Polymer-assisted-deposition: a chemical solution route for a wide range of materials, Chemical Society Reviews, 42 (2013) 439-449.

[136] J. Smith, L. Zeng, R. Khanal, K. Stallings, A. Facchetti, J.E. Medvedeva, M.J. Bedzyk, T.J. Marks, Cation Size Effects on the Electronic and Structural Properties of Solution-Processed In-X-O Thin Films, Adv. Electron. Mater., 1 (2015) 1500146.